



National Library
of Canada

Bibliothèque nationale
du Canada

Canadian Theses Service

Service des thèses canadiennes

Ottawa, Canada
K1A 0N4

NOTICE

The quality of this microform is heavily dependent upon the quality of the original thesis submitted for microfilming. Every effort has been made to ensure the highest quality of reproduction possible.

If pages are missing, contact the university which granted the degree.

Some pages may have indistinct print especially if the original pages were typed with a poor typewriter ribbon or if the university sent us an inferior photocopy.

Previously copyrighted materials (journal articles, published tests, etc.) are not filmed.

Reproduction in full or in part of this microform is governed by the Canadian Copyright Act, R.S.C. 1970, c. C-30.

AVIS

La qualité de cette microforme dépend grandement de la qualité de la thèse soumise au microfilmage. Nous avons tout fait pour assurer une qualité supérieure de reproduction.

S'il manque des pages, veuillez communiquer avec l'université qui a conféré le grade.

La qualité d'impression de certaines pages peut laisser à désirer, surtout si les pages originales ont été dactylographiées à l'aide d'un ruban usé ou si l'université nous a fait parvenir une photocopie de qualité inférieure.

Les documents qui font déjà l'objet d'un droit d'auteur (articles de revue, tests publiés, etc.) ne sont pas microfilmés.

La reproduction, même partielle, de cette microforme est soumise à la Loi canadienne sur le droit d'auteur, SRC 1970, c. C-30.

THE UNIVERSITY OF ALBERTA

POLARIZED PROTON-PROTON
BREMSSTRAHLUNG AT 280 MeV

by

KARO MICHAELIAN

A THESIS

SUBMITTED TO THE FACULTY OF GRADUATE STUDIES AND
RESEARCH IN PARTIAL FULFILMENT OF THE REQUIREMENTS
FOR THE DEGREE OF DOCTOR OF PHILOSOPHY

IN

NUCLEAR PHYSICS

DEPARTMENT OF PHYSICS

EDMONTON, ALBERTA

FALL, 1987

Permission has been granted to the National Library of Canada to microfilm this thesis and to lend or sell copies of the film.

The author (copyright owner) has reserved other publication rights, and neither the thesis nor extensive extracts from it may be printed or otherwise reproduced without his/her written permission.

L'autorisation a été accordée à la Bibliothèque nationale du Canada de microfilmer cette thèse et de prêter ou de vendre des exemplaires du film.

L'auteur (titulaire du droit d'auteur) se réserve les autres droits de publication; ni la thèse ni de longs extraits de celle-ci ne doivent être imprimés ou autrement reproduits sans son autorisation écrite.

ISBN 0-315-41037-X

THE UNIVERSITY OF ALBERTA

RELEASE FORM

NAME OF AUTHOR: KARO MICHAELIAN

TITLE OF THESIS: POLARIZED PROTON-PROTON

BREMSSTRAHLUNG AT 280 MeV.

DEGREE: DOCTOR OF PHILOSOPHY

YEAR THIS DEGREE GRANTED: 1987

Permission is hereby granted to THE UNIVERSITY OF ALBERTA LIBRARY to reproduce single copies of this thesis and to lend or sell such copies for private, scholarly or scientific research purposes only.

The author reserves other publication rights, and neither the thesis nor extensive abstracts from it may be printed or otherwise reproduced without the author's written permission.

(Signed)

K. Michaelian

PERMANENT ADDRESS:

NUCLEAR RESEARCH CENTER

UNIVERSITY OF ALBERTA

EDMONTON, ALBERTA

CANADA, T6G 2N5

DATED:

Oct 13 / 87

THE UNIVERSITY OF ALBERTA
FACULTY OF GRADUATE STUDIES AND RESEARCH

The undersigned certify that they have read, and recommend to the Faculty of Graduate Studies and Research, for acceptance, a thesis entitled "POLARIZED PROTON-PROTON BREMSSTRAHLUNG AT 280 MeV" submitted by KARO MICHAELIAN in partial fulfilment of the requirements for the degree of Doctor of Philosophy in Nuclear Physics.

P. Kitchin
.....
Supervisor

camish
.....
W. B. Allen
W. B. Allen
.....
ap. Kamaat
.....
Min
.....
External Examiner

Date: *Aug. 6, 1987*

Dedication

To Mom and Papa for nurturing within me an interest to explore nature and for giving me the courage and the inspiration to do so.

Abstract

A proton-proton bremsstrahlung experiment was performed with the objective of learning about the off-shell nature of the strong force. Both the 5-fold differential cross sections and the analysing powers for this reaction were measured in 320 bins over a wide set of coplanar geometries from near on-shell to far off-shell. Events were generated with a 280 MeV polarized proton beam incident on a liquid hydrogen target. All three final state particles were detected in order to keep background at a minimum.

Prior to this experiment existing bremsstrahlung data questioned the validity of current potential models for the nuclear force in the off-shell regions. In particular, a completely on-shell approximation, the Soft Photon Approach (SPA) was held in favor over these models. With an improvement in statistics of an order of magnitude, we were able to accurately measure the cross sections and analysing powers and ascertain the quantitative validity of the potential models.

The data is compared with a modern bremsstrahlung calculation with input from two of the latest potential models, the Paris and the Bonn potentials, and also the SPA. The ingredients that go into these calculations are summarized in the following chapters.

This experiment is the first to give a direct and clear indication of the off-shell nature of the strong force and also represents the first statistically significant measurement of proton-proton bremsstrahlung analysing powers.

Acknowledgements

I would like to express my sincere gratitude to my supervisor Professor Peter Kitching for the guidance and independence he has afforded me throughout my student years. His patience, support and many contributions to my education will always be remembered.

Special thanks to the many University of Alberta professors and scientists who have conferred some of their knowledge and experience, especially the following TRIUMF research scientists: Rudy Abegg who provided much personal support and introduced me to the operation of a cyclotron; Dave Hutcheon who was instrumental in running this experiment and Andy Miller who provided valuable advice and information.

The acquisition and analysis of the experimental data couldn't have been accomplished without the combined efforts of two generous persons: Gordon Greeniaus who introduced me to Monte Carlo simulations and provided advice on both scientific and personal affairs; and Peter Green who gave me a general education in the operation of computers.

The fatherly tutoring by Herb Coombes on many aspects of the electronics and detectors will be cherished. Harold Fearing gave me a gentle introduction to bremsstrahlung theory and provided the theoretical curves to which our data was compared.

I would like to thank Jan Soukup for his contributions to the design and construction of the target and scattering chamber and for allowing me to reproduce drawings of these in this thesis.

Also I wish to thank my acting supervisor Professor W.C. Olsen and all the other members of the U. of A. Experiment 208 group for their help in the initial set-up and data collection phases of this experiment.

Completion of this experiment required residence in two cities, Vancouver and Edmonton. In Edmonton Baltz and Madelyn Aguda shared with me many days and evenings of entertainment. Baltz provided academic stimulus and accompanied me on many travels of discovery. Comfort was found in my companionship with fellow students Reyad and Bunda.

In Vancouver the long days of work that rolled into nights were made immeasurably more enjoyable because of the warmth of a very special and dear friend Maria Manalo, who taught me how to give and love unselfishly. My respected guru Sul Kahn kept up my interest in activities of mutual appreciation and helped me focus on those things most important. Support and dear friendship was always provided by Josie, Alexis, Dinu and Mary.

Contents

1	Introduction	1
1.1	Elastic Scattering and the Question of Uniqueness	1
1.2	Many-Body Processes and Off-shell Effects	3
1.3	Nucleon-Nucleon Bremsstrahlung	5
2	Calculation of the Bremsstrahlung Amplitude	8
2.1	A Historical Perspective	8
2.2	The $pp\gamma$ Amplitude	10
2.2.1	Preliminary Remarks	15
2.2.2	The Electromagnetic Interaction	15
2.2.3	Non-relativistic Calculation of $\langle \vec{k} H_{em}^1 0 \rangle$	16
2.2.4	Relativistic Calculation of $\langle \vec{k} H_{em}^1 0 \rangle$	17
2.2.5	Bremsstrahlung Amplitude	20

2.2.6	External Emission	20
2.2.7	Internal Scattering	23
2.3	Potential Models	24
2.3.1	The Paris Potential	24
2.3.2	The Bonn Potential	27
2.4	The Soft Photon Approach	30
3	A Brief Overview of the Experiment	34
3.1	TRIUMF, The Facility	34
3.2	The Experiment	37
3.2.1	Target	37
3.2.2	Proton Detection	39
3.2.3	Photon Detection	40
3.2.4	Background Elimination	41
3.2.5	Electronics	42
3.2.6	Computer Acquisition	46
3.2.7	Semi-on line Analysis	47
3.2.8	Data Runs	48
3.2.9	Data Reduction	50
3.2.10	Analysis	50
3.2.11	Analysing Powers	53

3.2.12	Differential Cross-Section	53
4	Apparatus, Detector Calibration, Detector Timing	55
4.1	Apparatus	55
4.1.1	Beam Control	55
4.1.2	Polarimeter	57
4.1.3	SEM	58
4.1.4	Scattering Chamber	59
4.1.5	Liquid Hydrogen Target	61
4.1.6	Trigger Detectors	65
4.1.7	Vertical Drift Chambers	67
4.1.8	C-Magnet	70
4.1.9	Electronics	70
4.1.10	Computer	75
4.2	Detector Calibration	76
4.2.1	LEP Detectors	76
4.2.2	HEP Detectors	77
4.2.3	Cerenkov Detectors	77
4.2.4	Vertical Drift Chambers	78
4.3	Detector Timing	79
4.3.1	LEP and HEP Detectors	79

4.3.	Cerenkov Counters	80
5	Event Acquisition and Analysis	81
5.1	Acquisition	81
5.2	Analysis-Skimming	86
5.3	Analysis - Processing	93
6	Monte Carlo	108
6.1	Introduction	108
6.2	Description	114
6.2.1	Abbreviations and Definitions	114
6.2.2	The Coordinate System	117
6.2.3	Approximations	117
6.3	Beam Proton	118
6.4	Event Generation	119
6.5	Tracking	121
6.5.1	Tracking the LE Proton	122
6.5.2	Tracking the HE Proton	123
6.5.3	Tracking the Photon	128
6.6	Efficiency Weighting and Binning	128
7	ppγ Analyzing Powers and Cross Sections	138

7.1	Analysing Powers	138
7.2	$pp\gamma$ Cross Sections	145
8	Results and Conclusions	159
8.1	Results; Asymmetries and Cross Sections	159
8.2	Conclusion	161
	Bibliography	163
	Appendices	167
A	Cerenkov Detector Efficiencies	167
B	Target Empty and Target Vacuum Runs	175
C	PP Elastic Analysis	180
D	Potential Model Calculations of Fearing and Workman	190
E	Solid Angles Subtended by Detectors	193
E.1	Low Energy Protons (LEP)	193
E.2	High Energy Protons (HEP)	194
E.3	Photon Detectors	195
F	Systematic Errors	198
F.1	Errors that Normalize Out	198

F.2	Errors in Measurement	199
F.2.1	Cerenkov Detectors	199
F.2.2	LE Detectors	199
F.2.3	HE Detectors	200
F.3	Errors in Efficiency Calculations	201
F.3.1	VDC Missing and Multiple Efficiencies	202
F.4	Other Errors	203
F.5	Conclusions	203
G	Analysing Powers and Cross Sections, Numerical Values	205

List of Tables

4.1	Labels for liquid H_2 target items.	63
5.1	Event data word structure. (Part 1.)	82
5.2	Event data word structure. (Part 2.)	83
5.3	DCR bit assignments.	85
5.4	Detector multiples statistics.	94
5.5	Results of the VDC multiples reduction scheme.	97
5.6	Accumulated scaler counts in the LAC.	103
5.7	Accumulated scaler counts in the SAC	103
5.8	Accumulated $p\bar{p}\gamma$ event counts in the LAC.	104
5.9	Accumulated random counts in the LAC.	105
5.10	Accumulated $p\bar{p}\gamma$ event counts in the SAC.	106
5.11	Accumulated random counts in the SAC.	107
6.1	VDC not missing efficiencies for the LAC.	132
6.2	VDC not missing efficiencies for the SAC.	133

6.3	Detector not multiple efficiencies for the LAC and SAC as a function of position on anode plane 2X.	134
6.4	Detector not multiple efficiencies for the LAC and SAC.	134
6.5	Cerenkov detector not multiple efficiencies for the LAC and SAC.	135
6.6	Ratio of IDEAL to REAL monte carlo counts for the LAC.	137
6.7	Ratio of IDEAL to REAL monte carlo counts for the SAC.	137
7.1	The error introduced by averaging over only 4 topplanar points ΔA_y^{theo} and $\Delta \sigma^{theo}$, and the ratio of this error to the statistical experimental error. Results are for an HE bin centered at 27.8° and a 4° wide LE bin centered at 28.0° (LAC).	146
7.2	The error introduced by averaging over only 4 coplanar points ΔA_y^{theo} and $\Delta \sigma^{theo}$, and the ratio of this error to the statistical experimental error. Results are for an HE bin centered at 12.4° and a 4° wide LE bin centered at 12.0° (SAC).	147
8.1	Values per data point for the asymmetry plots of Chapter 7. Each plot contains 16 data points.	160
A.1	Photon absorber thicknesses intervening between target and Pb glass detectors. Units of cm.	168
A.2	More photon absorber thicknesses intervening between target and Pb glass detectors. Units of cm.	169

A.4	Photon detection efficiencies in the SAC.	174
B.1	Corrections to the target empty and vacuum data. The column labeled, 'Counts' represents the real events after subtraction of the randoms and application of all corrections.	179
C.1	Accumulated HE P/S events and correction factors for the LAC.	182
C.2	Accumulated HE P/S events and correction factors for the SAC.	183
E.1	Polar angle ranges, central value, distances, and solid angles subtended by the four HEP bins.	194
E.2	Central angles, distances, 1/2 widths, and solid angles of Cerenkov detectors in the LAC.	196
E.3	Central angles, distances, 1/2 widths, and solid angles of Cerenkov detectors in the SAC	197

List of Figures

1.1	Nucleon-nucleon bremsstrahlung Feynman diagrams for (a) single, and (b) double scattering.	6
2.1	Bremsstrahlung of a charged particle from a fixed, purely electromagnetic field.	10
2.2	External emission diagrams.	11
2.3	Double scattering.	12
2.4	ρ or ω radiative decay.	13
2.5	Pion bremsstrahlung.	13
2.6	Delta excitation.	14
2.7	Radiation from the momentum dependence of the potential.	14
2.8	External emission.	20
2.9	Internal emission.	23
2.10	Contributions to the Paris nucleon-nucleon potential. Diagrams taken from reference [21]	25

vertices (ii). Diagrams taken from reference [24].	28
3.1 Experimental setup for detecting bremsstrahlung events.	38
3.2 Hydrogen target flask. Only the central 5 mm portion contains liquid H ₂	39
3.3 Coincidences required for a 3-coincidence event.	43
3.4 Schematic diagram of the event acquisition.	49
3.5 HEP angle of bend through the spectrometer versus photon scattering angle. After application of all tests excluding the test on abscissa. HEP bin centered at 17.5°	52
4.1 TRIUMF's 1B beamline.	56
4.2 The pp elastic polarimeter.	57
4.3 Scattering chamber containing the hydrogen target and the LE proton detectors.	60
4.4 Cross sectional views through the liquid H ₂ portion of the target. The 'bite' taken out of the cell body helped reduce photon losses. Labels are given on the following page.	62
4.5 Operation of vertical drift chambers.	69
4.6 Two views of the high energy proton momentum analysing C-magnet.	71
4.7 Electronic logic for handling 3-coincidence events.	72

4.9	Electronic logic for the pulser events.	76
5.1	LEP time of flight versus HEP time of flight. The prompt central peak contains the real $pp\gamma$ events.	87
5.2	HEP bend angle through the spectrometer versus LEP time of flight.	88
5.3	LEP time of flight versus LEP deposited energy. The central peak contains the real $pp\gamma$ events	89
5.4	Cerenkov-RF time spectrum summed over all 16 Cerenkov detectors.	91
5.5	Algorithm to determine VDC quantities for the case of an event at the site of a dead wire.	95
5.6	HEP angle of bend through spectrometer versus photon scat- tering angle. HEP bin centered at 17.5°	99
5.7	LEP deposited energy versus photon scattering angle.	100
5.8	Projection of the HE proton tracks in drift chambers 1 and 2 back to the target.	102
6.1	Raw collected $pp\gamma$ counts plotted as a function of photon scat- tering angle for the small angle SAC.	109
6.2	Raw collected $pp\gamma$ counts plotted as a function of photon scat- tering angle for the large angle SAC.	110

6.3	Raw collected $pp\gamma$ counts plotted as a function of photon scattering angle for the small angle LAC. Note the larger scale on the y-axis than for the SAC plots.	111
6.4	Raw collected $pp\gamma$ counts plotted as a function of photon scattering angle for the large angle LAC.	112
6.5	Flow chart of Monte Carlo code. Part one.	115
6.6	Flow chart of Monte Carlo code. Part two.	116
6.7	Use of Stoke's theorem to determine the vertically focusing horizontal components of the C-magnet field.	126
7.1	$pp\gamma$ analysing powers for the small angle SAC.	141
7.2	$pp\gamma$ analysing powers for the large angle SAC.	142
7.3	$pp\gamma$ analysing powers for the small angle LAC.	143
7.4	$pp\gamma$ analysing powers for the large angle LAC.	144
7.5	$pp\gamma$ cross sections for the small angle SAC. The data is arbitrarily normalized by multiplying by a factor of 0.667.	150
7.6	$pp\gamma$ cross sections for the small angle SAC. The data is arbitrarily normalized by multiplying by a factor of 0.667.	151
7.7	$pp\gamma$ cross sections for the large angle SAC. The data is arbitrarily normalized by multiplying by a factor of 0.667.	152
7.8	$pp\gamma$ cross sections for the large angle SAC. The data is arbitrarily normalized by multiplying by a factor of 0.667.	153

trarily normalized by multiplying by a factor of 0.667.	154
7.10 $pp\gamma$ cross sections for the small angle LAC. The data is arbitrarily normalized by multiplying by a factor of 0.667.	155
7.11 $pp\gamma$ cross sections for the large angle LAC. The data is arbitrarily normalized by multiplying by a factor of 0.667.	156
7.12 $pp\gamma$ cross sections for the large angle LAC. The data is arbitrarily normalized by multiplying by a factor of 0.667.	157
A.1 Distribution of electron deposited energy within the cerenkov veto counters. The peaks correspond to one or two minimum ionizing electrons.	171
C.1 HE P/S elastic analysing powers as a function of run number, or time, for the LAC.	184
C.2 HE P/S elastic analysing powers as a function of run number, or time, for the SAC.	185
C.3 HE P/S elastic cross sections as a function of run number, or time, for the LAC.	187
C.4 HE P/S elastic cross sections as a function of run number, or time, for the SAC.	188

Chapter 1

Introduction

Ever since the complicated momentum dependence of the strong, or nuclear, force was discovered it was realized that even complete knowledge of the two-body, i.e. elastic, interaction would not be enough to determine a unique potential for the force. A full description could only come through observing many-body interactions in conjunction with the two-body case.

1.1 Elastic Scattering and the

Question of Uniqueness

The objective of any elastic nucleon-nucleon scattering experiment is to determine the form of the strong interaction potential by observing the asymptotic waves of the scattered particles at a large distance from the target relative to the range of the interaction. In practice, one carries out numerous experiments to obtain the scattering amplitude. The most general form

pression containing five complex amplitudes. Nine experiments are needed to determine these 10 terms since they are related by an overall phase.

If the strong interaction were dependent only on the separation of the two interacting particles and not on their relative momentum, i.e. static, then it would be possible to show that the elastic scattering amplitude as a function of energy uniquely determines the potential. In such a case it would only be necessary to carry out the nine required experiments and form the potential from the results.

Unfortunately, nature is more complex in the case of the strong interaction. It is known that the force between nucleons carries a complicated momentum dependence in terms of effects such as the spin-orbit coupling, for example. In this case the potential cannot be uniquely determined from the elastic scattering amplitude and in fact it can be shown that there are infinitely many potentials which give equivalent phase shifts. (i.e. These potentials all fit the elastic data in any phase shift equally well.) Collectively these are known as 'phase equivalent potentials'.

The phase-equivalence arises because the elastic scattering amplitude is determined from the wavefunctions of the particles in the asymptotic limit. At large distances from the target the particles no longer feel the short range interaction and are therefore essentially free. Thus the wavefunctions for the scattered nucleons in this region only contain contributions from the so

$$p^2 c^2 = E^2 - m^2 c^4 \quad (1.1)$$

However, the wavefunction at small distances has contributions from momenta that are also off-shell. By fitting momentum dependent potentials to elastic data one thereby guarantees equivalence on-shell but it would only be fortuitous if they had the correct off-shell behavior.

What is needed then to probe the off-shell contribution to the nuclear force is an interaction involving three or more bodies. In this many-body interaction a scattered wave could impinge on a third body before reaching its asymptotic form. Put another way, it is not necessary for energy and momentum to be conserved in each two-body interaction as long as they are conserved in the overall system.

1.2 Many-Body Processes and Off-shell Effects

The effect of the off-shell contribution has important consequences in all nuclear many-body processes. Aside from bremsstrahlung some of those which have been used to study the off-shell behavior of the strong force include nuclear matter calculations, deuteron breakup, and knockout processes.¹ Concerning nuclear matter calculations, there is an on-going effort to reconcile

¹For a review of these processes in relation to the off-shell behavior of the strong force see [1].

energies with the observed values. The cross section for deuteron breakup, especially at high momentum transfer to the neutron, is found to be critically sensitive to the off-shell behavior of the interaction. Knockout reactions, such as quasi-elastic (p,2p) scattering, have been found to provide insight into off-shell behavior particularly below 200 MeV incident energy. These results, however, are complicated mainly due to nuclear distortion effects and multiple scattering.

The most direct approach, both experimentally and theoretically, to obtaining off-shell information has been through reactions of the form $N + N \rightarrow N + N + \gamma$ or, nucleon-nucleon bremsstrahlung. First, although this is a 3-body system, only 2-bodies are strongly interacting. Secondly, for the two nucleon system, bremsstrahlung is the first off-shell process that occurs with increasing energy. This means that experimentally, complications arising from other off-shell processes, for example pion production, can be avoided by staying below the thresholds of these processes². Bremsstrahlung is also easy to handle theoretically since the form of the electromagnetic interaction is well described by QED and its weakness with respect to the strong force allows the use of perturbation methods, in particular the Distorted Wave Born Approximation.

²Pion production is in fact the off-shell process that occurs next for the two nucleon system with a threshold of approximately 290 MeV lab energy.

1.3 Nucleon-Nucleon Bremsstrahlung

In bremsstrahlung two nucleons in the initial state go to two nucleons plus a photon in the final state. Off-shell elements arise because of the interplay between two interactions, the electromagnetic and the strong. The electromagnetic interaction is the photon takes away momenta from one of the nucleons allowing it to interact strongly off-the-energy-shell, i.e. such that equation 1.1 no longer holds. This nucleon has become a 'virtual' particle as it is not possible for a 'real' particle to emit a photon and simultaneously conserve both energy and momentum. The nucleon goes back on-the-energy-shell, i.e. becomes a real particle, by interacting strongly with the other nucleon. This process may involve photon emission from internal meson lines mediating the strong force, or double scattering in which the photon is emitted after a strong interaction, but the nucleon remains off-the-energy-shell until a subsequent strong interaction.

Both $pp\gamma$ and $np\gamma$ experiments have been performed in the past³. Both types have suffered from a critical lack of statistics due to the smallness of their cross section. Although at intermediate energies the $np\gamma$ cross section is approximately four times larger than the $pp\gamma$ cross section, experiments with neutrons are harder to perform mainly because of the much lower intensities of available neutron beams. Theoretically, $np\gamma$ is also more difficult to handle because one-pion-exchange currents must be included (see figure 2.5) and

³For a complete list of references for experiments performed prior to 1971 see the review article by Halbert [2]. The more recent experiments are described in references [3,4,5,6,7].

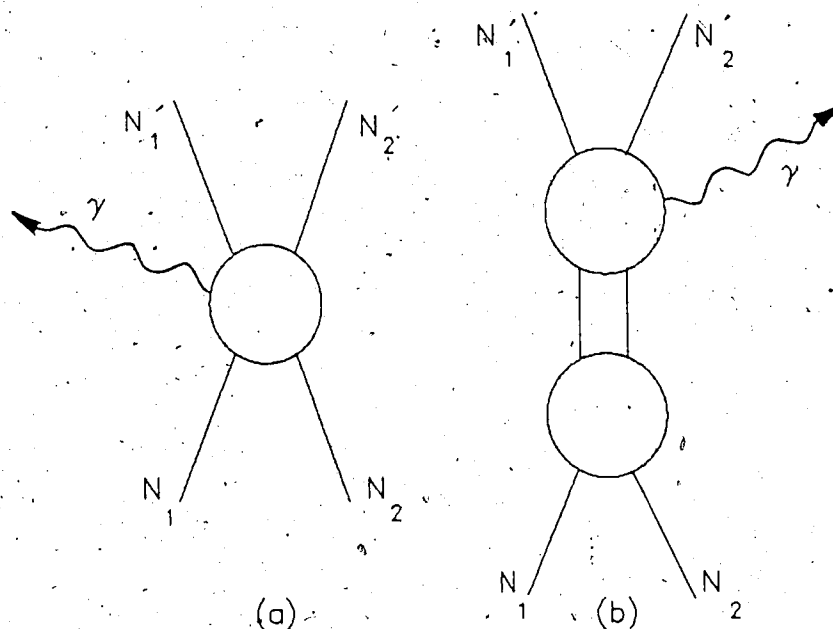


Figure 1.1: Nucleon-nucleon bremsstrahlung Feynman diagrams for (a) single, and (b) double scattering.

there are twice as many partial waves to calculate: the total wavefunction must be antisymmetric and the identity of the protons in $pp\gamma$ allows only angular momentum even singlet and angular momentum odd triplet states.

For these reasons a modern $pp\gamma$ experiment was initiated by the University of Alberta group at the TRIUMF cyclotron facility with the objective of learning about the off-shell behavior of the strong force. Specifically the goal of the experiment was twofold. First, to determine whether an existing modern potential would fit the experimental data in an off-shell region. To this end, a modern calculation with input from the Paris and Bonn potentials was initiated at TRIUMF.⁴ Secondly, a question as to why all previous

⁴H. Fearing and R. Workman performed the calculations. See [8] or [9] for details.

bremsstrahlung experiments seemed to agree best with a calculation which contains no off-shell input, the Soft Photon Approximation (SPA), apparently better than with potential models, had to be investigated. This approximation is expected to be valid only in the on-shell limit, i.e., where the photon's momentum goes to zero. Such agreement could only indicate some kind of accidental cancellation in the off-shell terms for the bremsstrahlung process. We wished to address these problems by not only measuring the cross section, but also by making the first statistically significant measurement of the $pp\gamma$ analysing power.

The experiment was well suited to the capabilities of TRIUMF since the facility provides a high intensity, high duty factor polarized proton beam within the energy range of interest. Experimental advances over earlier experiments include; a liquid hydrogen target, giving a well defined volume and solid angles; detection of all three final state particles, giving a greatly reduced background; and a large amount of allotted beam time, approximately 1000 hours, giving vastly improved statistics. A proton energy of 280 MeV was chosen as a compromise between too high an energy where potential models wouldn't be valid, and too low an energy where the cross section is smaller and approaches on-shell predictions. Proton polar angles between 10° and 30° were viewed. The maximum off-shellness of the interaction occurs at the smallest proton polar angles. The limit of 10° was set by the requirements of accommodating the detectors and the beam line.

Chapter 2

Calculation of the Bremsstrahlung Amplitude

2.1 A Historical Perspective

It took a number of years after the first bremsstrahlung experiment before a reasonably accurate theoretical description was given. The delay resulted mainly from improper assumptions about the contribution from the double scattering term when performing the calculation in the center of mass (CM) and lab coordinate systems. Initial estimates by Sobel and Cromer [10] 1963(SC) concluded that the double scattering term contributes less than 10% to the integrated $pp\gamma$ cross section. As this term is extremely difficult to calculate (there is a continuum of intermediate states) it was ignored in their initial laboratory-frame calculation utilizing a distorted-wave Born-approximation with input from the Yale and Brueckner-Gammel-

Thaler potentials¹. The first experiment, performed by Gottschalk et al. [11] at 158 MeV, gave cross sections smaller than those predicted by a factor of four. Further experiments [12,13,14] at lower energies showed that the discrepancy became worse.

Duck and Pearce [15] 1966(DP) made an independent calculation of the $pp\gamma$ cross section using the SC formalism, also omitting the double scattering term, but this time doing it in the CM frame. They found agreement with the data at 158 MeV and, after correcting a number of errors in both their calculation and the SC formalism, reasonable fits were also obtained at lower energies.

The DP and SC discrepancy was finally resolved by Signell [16] who first obtained an analytical description of the single- and double-scattering terms for low incident proton momenta. He found that in the laboratory frame the single- and double-scattering terms were both large and of opposite sign. In the CM frame, the single-scattering term was small compared to its laboratory counter-part and the double scattering term was negligible. The conclusion was that low energy calculations done in the lab frame must include both single- and double-scattering terms where as in the CM frame, calculation of just the single scattering term suffices. At high energies it is now realized that both terms are important regardless of the frame chosen.

So far, only Brown [17] has calculated double scattering terms, and only at low energies (corrections to the integrated cross section were found to be 10-

¹Older phenomenological potentials fit to the data with a large number of free parameters.

15% at 158 MeV), but there is now an effort by Fearing [18] to include double scattering terms in a gauge invariant calculation based on the modern Paris and Bonn potentials. This calculation contains many corrections, such as Coulomb and relativistic effects (extensions of the relativistic spin corrections of Liou and Sobel [section 2.2.4]), not before included.

2.2 The $pp\gamma$ Amplitude

This section outlines the steps involved in calculating the bremsstrahlung amplitude. To elucidate the process somewhat we first consider bremsstrahlung of a charged particle from a fixed, purely electromagnetic field (figure 2.1).

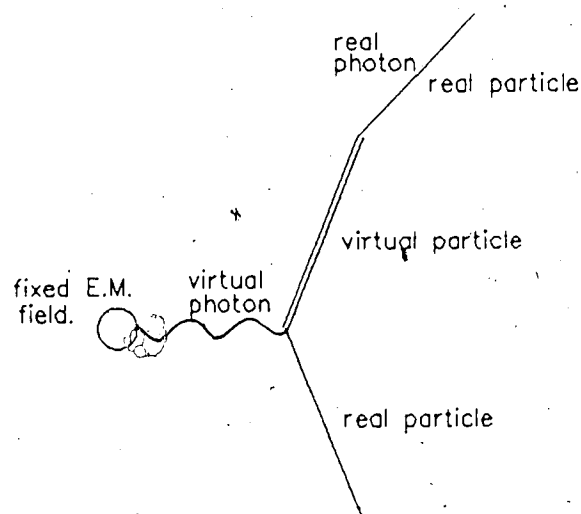


Figure 2.1: Bremsstrahlung of a charged particle from a fixed, purely electromagnetic field.

In this Feynman diagram, a real charged particle absorbs a virtual photon from the electromagnetic (E.M.) field. Four momentum conservation requires that the proton become a virtual particle, (i.e. it goes off-the-energy shell), before emitting a real photon which puts it back on the energy shell.

The case of nucleon-nucleon bremsstrahlung is more complicated since both the strong and the electromagnetic forces play a part. Two classes of bremsstrahlung arise: external and internal emission. External emission, or single scattering, has the photon emitted from one of the off-shell lines of the proton before or after the strong interaction. External emission is depicted in the following diagrams.

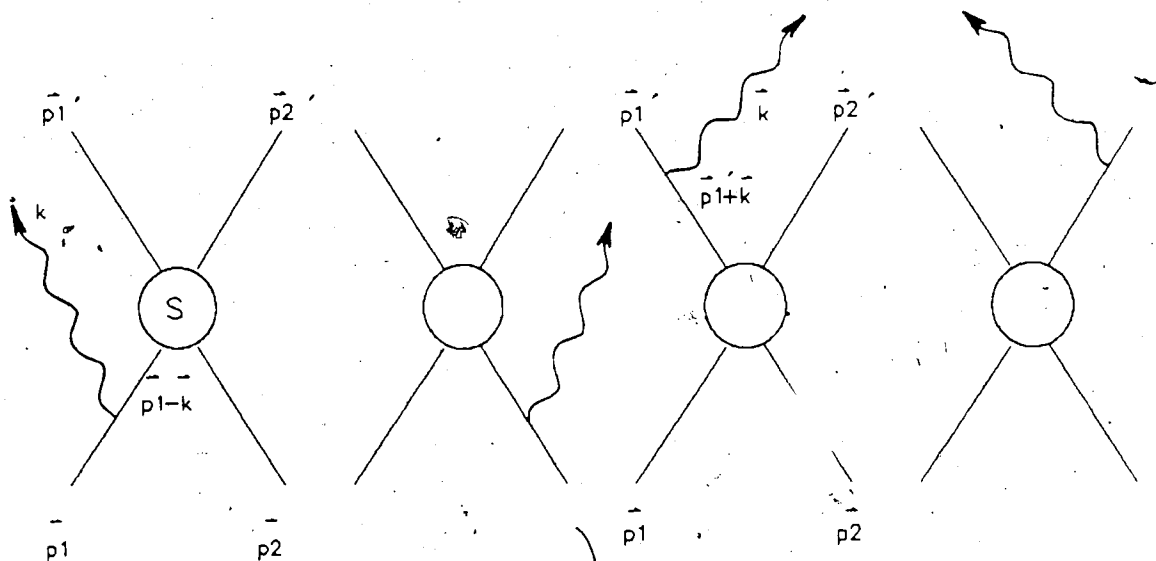


Figure 2.2: External emission diagrams.

In the left most diagram of figure 2.2, the acceleration proton 1 (\vec{p}_1) experiences in the field of proton 2 (\vec{p}_2) causes it to emit a photon which puts \vec{p}_1 off-the-energy-shell. It then interacts strongly at S with \vec{p}_2 putting itself back on the energy-shell. Four such diagrams are drawn corresponding

to photon emission from the different proton lines.

Internal emission, which includes double scattering, has the photon coupling in some way to the internal meson lines which mediate the strong force. This can be divided into several classes.

1. Double scattering, figure 2.3, where the photon is emitted after a strong

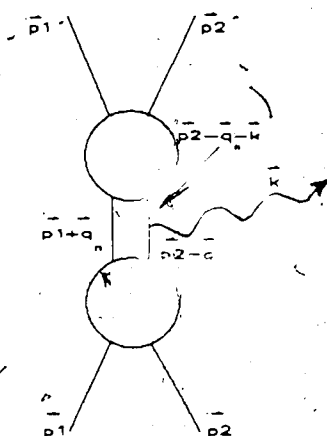


Figure 2.3: Double scattering.

interaction and the proton remains off-the-energy shell until a subsequent strong interaction. As mentioned earlier, double scattering is considerably more difficult to calculate because of the energy continuum of intermediate virtual states (\vec{q}_n can have any value).

2. Radiation from internal emission lines, for example;

- (a) for $pp\gamma$, ρ or ω radiative decay, figure 2.4, where the ρ or ω vector mesons decay electromagnetically into a pion and a photon.
- (b) for $np\gamma$, pion bremsstrahlung, figure 2.5, where the charged pion mediating the strong force interacts electromagnetically with ei-

ther the neutron or proton.

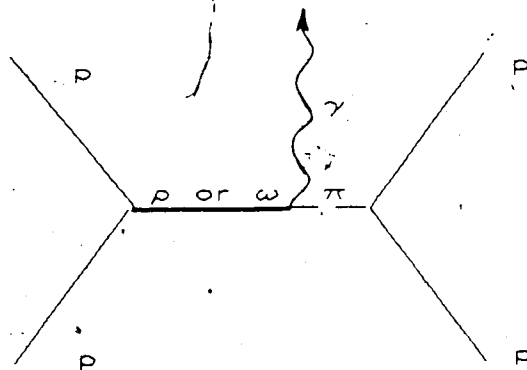


Figure 2.4: ρ or ω radiative decay.

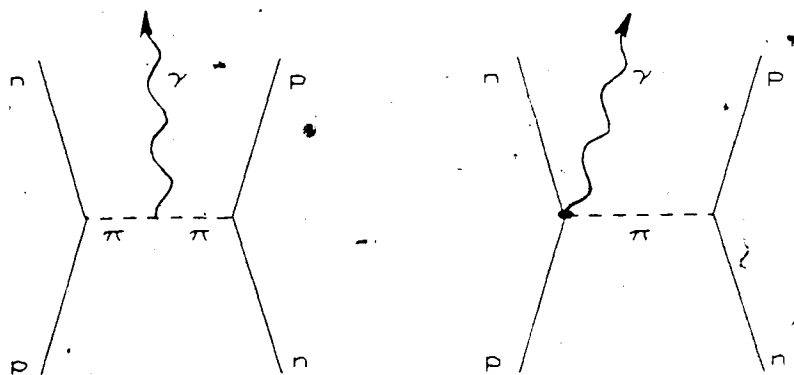


Figure 2.5: Pion bremsstrahlung.

3. Delta excitation, figure 2.6, where a pion excites a proton into a Δ resonance which subsequently decays electromagnetically into a proton and a photon.
4. Radiation from the momentum dependence of the nuclear potential, figure 2.7. Such terms are generated when \vec{p} is replaced by $\vec{p} - e\vec{A}$ in

the potential, (section 2.2.2). Diagrams like those of class 2. and 3. may contribute to this diagram.

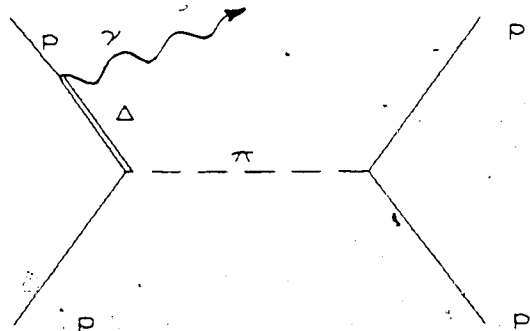


Figure 2.6: Delta excitation.

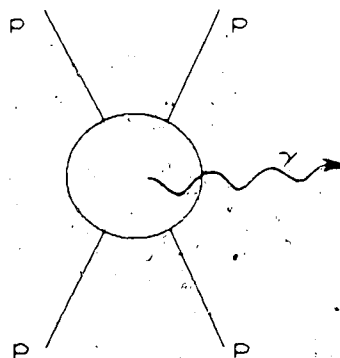


Figure 2.7: Radiation from the momentum dependence of the potential.

The object of a theoretical calculation is to determine an amplitude for each of the diagrams and then obtain experimentally measurable quantities such as; the cross section $\sigma \rightarrow \Sigma |\text{amplitudes}|^2$; and the analysing power $A_y \rightarrow (\sigma^\uparrow - \sigma^\downarrow)/(\sigma^\uparrow + \sigma^\downarrow)$. Here σ^\uparrow , σ^\downarrow are the cross sections for the incident proton polarized in the spin up and down states respectively. Steps

involved in calculating an amplitude for each of the above diagrams will be outlined next. We follow an older but comprehensive description by Liou and Sobel [19], and a very recent, (1985), calculation of the cross section and analysing power from modern potential models (Paris and Bonn), by Fearing and Workman [9,8]

2.2.1 Preliminary Remarks

The approach is to obtain an amplitude from a potential via the non-relativistic Schrödinger equation. However, as Liou and Sobel point out, parameters of the potential are determined by fits to real elastic scattering data which is inherently relativistic. Therefore it is reasonable to expect that such a strictly non-relativistic treatment suffices for a bremsstrahlung experiment which is only "somewhat" relativistic at 280 MeV. Relativistic kinematics are used throughout and the electromagnetic interaction is treated relativistically to order $(K.E._{proton}/M_{proton})^3$. Also, terms which go as α^2 and higher are neglected because of the weakness of the electromagnetic coupling.

2.2.2 The Electromagnetic Interaction

The electromagnetic interaction between the two protons is brought into the equation of motion by replacing the momentum operator in the Schrödinger equation, \vec{p} by $\vec{p} - e\vec{A}(\vec{r}, t)$, where \vec{A} is the operator form of the vector potential. This replacement is known as 'minimal electromagnetic coupling' since only one constant, e , is introduced. The coulomb gauge, $\Phi = 0$, $\vec{\nabla} \cdot \vec{A} =$

0, is chosen for the E.M. interaction with the vector potential conveniently written in terms of photon creation and annihilation operators

$$\vec{A}(\vec{r}, t) = \frac{1}{2\pi\sqrt{k_0}} \hat{\epsilon} [a e^{-ik_0 t + i\vec{k} \cdot \vec{r}} + a^\dagger e^{ik_0 t - i\vec{k} \cdot \vec{r}}]. \quad (2.1)$$

Here $\hbar = c = 1$, k_0 = photon energy, $\hat{\epsilon}$ = photon polarization, and the creation and annihilation operators are defined by

$$\begin{aligned} \langle \vec{k} | a^\dagger | 0 \rangle &= 1 \\ \langle \vec{k} | a | 0 \rangle &= 0. \end{aligned}$$

The interaction of the protons with their external E.M. field yields a hamiltonian H_{em}^1 . A second term H_{em}^2 arises when the substitution $\vec{p} \rightarrow \vec{p} - e\vec{A}(\vec{r}, t)$ is made because of the momentum dependence of the nuclear potential. The total E.M. hamiltonian is then

$$H_{em} = H_{em}^1 + H_{em}^2. \quad (2.2)$$

For purposes of term identification and comparison, both a non-relativistic and a relativistic calculation of the matrix element for the creation of a photon will be made.

2.2.3 Non-relativistic Calculation of $\langle \vec{k} | H_{em}^1 | 0 \rangle$

The momentum operator \vec{p} is replaced by $\vec{p} - e\vec{A}$ in the kinetic energy operator ($\vec{p}^2/2m$), of the Schrödinger equation. A magnetic moment interaction $-\vec{\mu} \cdot \vec{B}$ is also added making the coupling no longer minimal. Here $\mu = \frac{e}{2m} u \vec{\sigma}$ and

$\vec{B} = \nabla \times \vec{A}$ with $u = 2.793$ and where $\vec{\sigma}$ is the proton's spin. The non-relativistic hamiltonian for the protons interaction with an E.M. field is then,

$$H_{em}^{(N.R.)} = \frac{(\vec{p} - e\vec{A}(\vec{r}, t))^2}{2m} - \vec{\mu} \cdot (\vec{\nabla} \times \vec{A}). \quad (2.3)$$

Replacing \vec{A} with its form in terms of creation and annihilation operators and neglecting terms of order α^2 and higher, the non-relativistic matrix element for the creation of a photon is

$$\langle \vec{k} | H_{em}^1 | 0 \rangle = -e \frac{e^{ik_0 t}}{2\pi m k_0^{1/2}} \sum_{j=1}^2 \left[\hat{e} \cdot \vec{p}_j + i \frac{u}{2} \vec{\sigma}_j \cdot (\hat{e} \times \vec{k}) \right] e^{-i\vec{k} \cdot \vec{r}_j}, \quad (2.4)$$

with the kinetic energy operator subtracted off and where the sum over j accounts for the two protons.

2.2.4 , Relativistic Calculation of $\langle \vec{k} | H_{em}^1 | 0 \rangle$

The relativistic equivalent of the Schrödinger equation is the Dirac equation,

$$i \frac{\partial \Psi}{\partial t} = H \Psi. \quad (2.5)$$

For a proton in an electromagnetic field²

$$H = \vec{\alpha} \cdot (\vec{p} - e\vec{A}) + \beta m + e\phi + \beta \frac{e}{2m} (u - 1) (i\vec{\alpha} \cdot \vec{E} - \vec{\sigma} \cdot \vec{B}), \quad (2.6)$$

where $\vec{\alpha}$ and β are the 4×4 Dirac matrices. Equation 2.5 is a four component equation: two energy components plus two components of spin. It is possible to reduce this to a two component positive energy equation for the proton

²See for example, Bjorken and Drell. The last term is due to the anomalous magnetic moment of the proton

by applying a 'Foldy-Wouthuysen' transformation [20]. This transformation removes the small negative energy components from the Hamiltonian to any desired order of the kinetic energy of the proton over its mass $\left(\frac{K.E.p}{m_p}\right)$. Such a transformation is useful in the present case and we choose to go to third order where $\left(\frac{K.E.p}{m_p}\right)^3 = \left(\frac{280}{938}\right)^3$ is small. The resulting two component equation to this order takes the form

$$H'\Phi = i\frac{\partial\Phi}{\partial t} \quad (2.7)$$

with

$$H' = m + \frac{\vec{p}^2}{2m} + \frac{(\vec{p}^2)^2}{8m^3} + e\phi + H_{em}^{FW} \quad (2.8)$$

and

$$\begin{aligned} H_{em}^{FW} = & -\frac{e}{2m}[(\vec{p} \cdot \vec{A} + \vec{A} \cdot \vec{p}) - \frac{e}{2m}u\vec{\sigma} \cdot \vec{B}] \\ & -\frac{e}{8m^2}(2u-1)\vec{\nabla} \cdot \vec{E} \\ & -i\frac{e}{8m^2}(2u-1)\vec{\sigma} \cdot (\vec{\nabla} \times \vec{E}) \\ & -\frac{e}{4m^2}(2u-1)\vec{\sigma} \cdot (\vec{E} \times \vec{p}) \\ & -\frac{e}{8m^3}[\vec{p}^2(\vec{p} \cdot \vec{A} + \vec{A} \cdot \vec{p}) + \vec{p} \cdot \vec{A} + \vec{A} \cdot \vec{p}\vec{p}^2] \end{aligned} \quad (2.9)$$

In the Coulomb gauge and neglecting the relativistic correction to the proton's kinetic energy

$$H' = m + \frac{\vec{p}^2}{2m} + H_{em}^{FW}$$

Terms 1 and 2 of equation 2.9 together with equation 2.8 make up the whole of the non-relativistic hamiltonian, equation 2.3. They are the main electric and magnetic contributions.

The remaining terms of equation 2.9 are relativistic corrections to the main terms. The third term $\rightarrow \frac{1}{m^2} \vec{\nabla} \cdot \vec{E}$, known as the 'Darwin' term, is attributed to 'zitterbewegung': (In a relativistic quantum mechanical picture the proton's coordinate is not static but fluctuates over a distance $\delta r \simeq \frac{1}{m}$.) Terms 4 and 5 are relativistic spin corrections. Bjorken and Drell [20] show that these terms comprise the spin orbit energy which has the more familiar form for a spherically symmetric potential. In this case the fourth term goes as

$$\vec{\nabla} \times \vec{E} = \vec{\nabla} \times \vec{\nabla} V = 0,$$

and the fifth term goes as

$$\begin{aligned} \vec{\sigma} \cdot (\vec{E} \times \vec{p}) &= -\frac{1}{r} \frac{\partial V}{\partial r} \vec{\sigma} \cdot \vec{r} \times \vec{p} \\ &= -\frac{1}{r} \frac{\partial V}{\partial r} \vec{\sigma} \cdot \vec{L}. \end{aligned}$$

Term 6 $\rightarrow \vec{p}^2 (\vec{p} \cdot \vec{A})$ is a relativistic correction to the main electric term (term 1).

The relativistic matrix element for the creation of a photon by a proton within a uniform electromagnetic field is then

$$\begin{aligned} \langle \vec{k} | H_{em}^{FW} | 0 \rangle &= N e^{-i\vec{k} \cdot \vec{r}} \left\{ \vec{p} \cdot \hat{\epsilon} - \frac{1}{4m^2} [\vec{p}^2 \vec{p} \cdot \hat{\epsilon} + \vec{p} \cdot \hat{\epsilon} \vec{p}^2] \right. \\ &\quad \left. + i \frac{u}{2} \vec{\sigma} \cdot \hat{\epsilon} \times \left[\vec{k} - \left(1 - \frac{1}{2u} \right) \left(\frac{\vec{p}}{m} + \frac{\vec{k}}{2m} \right) \vec{k} \right] \right\}. \end{aligned} \quad (2.10)$$

For a system with two protons in their mutual electromagnetic field the relativistic Hamiltonian is

$$H_{em}^1 = \sum_{j=1}^2 (H_{em}^{FW})_j + H^{\Delta FW}. \quad (2.11)$$

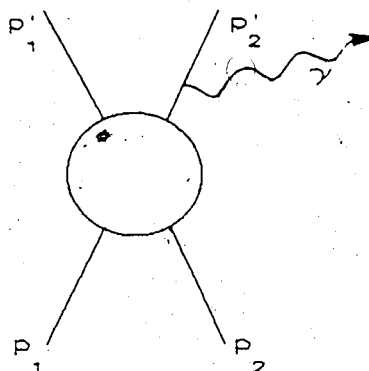


Figure 2.8: External emission.

As a reminder, the superscript 1 refers to that part of the total E.M. hamiltonian that comes from the static E.M. interaction between the two protons; the sum over j takes care of the fact that there are two protons. $H^{\Delta FW}$ is a correction term that arises from a Foldy-Wouthuysen reduction of the two particle system. (Found to be small, i.e. effects the cross section by $< 1\%$ at intermediate energies [19].)

2.2.5 Bremsstrahlung Amplitude

The total bremsstrahlung amplitude can be obtained through the use of Feynman diagrams or by doing an analytic determination of the Born series. Here an association will be made with Feynman diagrams depicting external and internal emission.

2.2.6 External Emission

The amplitude for the external emission diagram of figure 2.8 is

$$\begin{aligned} \langle \vec{p}_1', \vec{p}_2' | T_E | \vec{p}_1, \vec{p}_2 \rangle &= \langle \vec{k} | H_{em}^{FW} + H^{\Delta FW} | 0 \rangle \langle \vec{p}_1', \vec{p}_2' + \vec{k} | G_0(E) | \vec{p}_1, \vec{p}_2 \rangle \\ &\quad \cdot \langle \vec{p}_1', \vec{p}_2' + \vec{k} | t(E) | \vec{p}_1, \vec{p}_2 \rangle + \dots \end{aligned} \quad (2.12)$$

where \dots represents 3 similar terms for the other diagrams. The factors have the following significance; $\langle \vec{k} | H_{em}^{FW} + H^{\Delta FW} | 0 \rangle$ is the matrix element for the creation of a photon: obtained from equation 2.10 ; $\langle \vec{p}_1', \vec{p}_2' + \vec{k} | G_0(E) | \vec{p}_1, \vec{p}_2 \rangle$ is the free proton propagator in the intermediate, i.e. virtual state:

$$\begin{aligned} G_0(E) &= (E - H^0)^{-1} \\ &\simeq \text{the Lorentz invariant } m(E_2' k - \vec{p}_2' \cdot \vec{k})^{-1} \\ &= \frac{m}{p_{2\mu}' k^\mu}. \end{aligned} \quad (2.13)$$

The final term $\langle \vec{p}_1', \vec{p}_2' + \vec{k} | t(E) | \vec{p}_1, \vec{p}_2 \rangle$ is the two proton off-shell interaction matrix obtained from a particular potential. Fearing et al. determine this term by writing it, in each partial wave, as a product of the on-shell interaction matrix and a half-off-shell function F_l ,

$$t_l(E, \vec{p}_1', \vec{p}_2' + \vec{k}, \vec{p}_1, \vec{p}_2) = F_l(\vec{p}_1', \vec{p}_2' + \vec{k}, \vec{p}_1, \vec{p}_2) t_l(E, \vec{p}_1', \vec{p}_2', \vec{p}_1, \vec{p}_2), \quad (2.14)$$

where $t_l(E, \vec{p}_1', \vec{p}_2' + \vec{k}, \vec{p}_1, \vec{p}_2) = \langle \vec{p}_1', \vec{p}_2' + \vec{k} | t_l(E) | \vec{p}_1, \vec{p}_2 \rangle$. This is then substituted into the partial wave momentum space Lippmann-Schwinger equation which can be solved for F_l . The full external amplitude, including all four diagrams, is obtained from equation 2.12 with equations 2.10, 2.13, and 2.14.

$$\langle \vec{p}_1', \vec{p}_2' | T_E | \vec{p}_1, \vec{p}_2 \rangle = N m \left[A \frac{1}{p_{1\mu}' k^\mu} \langle \vec{p}_1' + \vec{k}, \vec{p}_2' | t(E) | \vec{p}_1, \vec{p}_2 \rangle \right]$$

$$\begin{aligned}
& - \langle \vec{p}_1, \vec{p}_2 | t(E') | \vec{p}_1 - \vec{k}, \vec{p}_2 \rangle \frac{1}{p_{1\mu} k^\mu} B \\
& + C \frac{1}{p_{2\mu} k^\mu} \langle \vec{p}_1, \vec{p}_2 + \vec{k} | t(E) | \vec{p}_1, \vec{p}_2 \rangle \\
& - \langle \vec{p}_1, \vec{p}_2 | t(E') | \vec{p}_1, \vec{p}_2 - \vec{k} \rangle \frac{1}{p_{2\mu} k^\mu} D \Big], \quad (2.15)
\end{aligned}$$

where

$$\begin{aligned}
A = & \vec{\epsilon} \cdot \vec{p}_1 \left(1 - \frac{2p_1'^2 + \vec{p}_1 \cdot \vec{k} + k^2}{4m^2} \right) + i \frac{u}{2} \vec{\sigma}_1 \cdot \vec{\epsilon} \times \left[\vec{k} - \left(1 - \frac{1}{2u} \right) \left(\frac{\vec{p}_1}{m} + \frac{\vec{k}}{2m} \right) k_0 \right. \\
& \left. + \frac{k_0 \vec{p}_2}{4um} \right] - i \frac{u}{2} \vec{\sigma}_2 \cdot \vec{\epsilon} \times \frac{k_0 \vec{p}_2}{4um} \quad (2.16)
\end{aligned}$$

B, C, and D have similar definitions and correspond to photon emission from the different proton lines. (These will be given explicitly after some simplification.)

The last two terms of A, of the forms $\vec{\sigma}_1 \cdot \vec{\epsilon} \times \vec{p}_2'$ and $\vec{\sigma}_2 \cdot \vec{\epsilon} \times \vec{p}_2'$ are due to the correction term $H^{\Delta FW}$. Liou and Sobel have shown, by explicit calculation that these terms are negligible [19].

Equation 2.16 can be simplified by noting that p^3/m^2 (or $p^2 k/m^2$), is small compared with p , and that $\vec{\sigma}_1 \cdot \vec{\epsilon} \times \frac{\vec{k}}{2m}$ is small compared with $\vec{\sigma}_1 \cdot \vec{\epsilon} \times \frac{\vec{p}_1}{m}$, since $\frac{p^2}{2m} \sim k$ and therefore $\frac{p}{k} \sim \frac{2m}{p} \gg 1$.

These simplifications give,

$$\begin{aligned}
A &= \vec{p}_1 \cdot \vec{\epsilon} + \frac{i u}{2} \vec{\sigma}_1 \cdot \vec{\epsilon} \times \left[\vec{k} - \left(1 - \frac{1}{2u} \right) \frac{k_0}{m} \vec{p}_1 \right], \\
B &= \vec{p}_1 \cdot \vec{\epsilon} + \frac{i u}{2} \vec{\sigma}_1 \cdot \vec{\epsilon} \times \left[\vec{k} - \left(1 - \frac{1}{2u} \right) \frac{k_0}{m} \vec{p}_1 \right], \\
C &= \vec{p}_2 \cdot \vec{\epsilon} + \frac{i u}{2} \vec{\sigma}_2 \cdot \vec{\epsilon} \times \left[\vec{k} - \left(1 - \frac{1}{2u} \right) \frac{k_0}{m} \vec{p}_2 \right], \\
D &= \vec{p}_2 \cdot \vec{\epsilon} + \frac{i u}{2} \vec{\sigma}_2 \cdot \vec{\epsilon} \times \left[\vec{k} - \left(1 - \frac{1}{2u} \right) \frac{k_0}{m} \vec{p}_2 \right]. \quad (2.17)
\end{aligned}$$

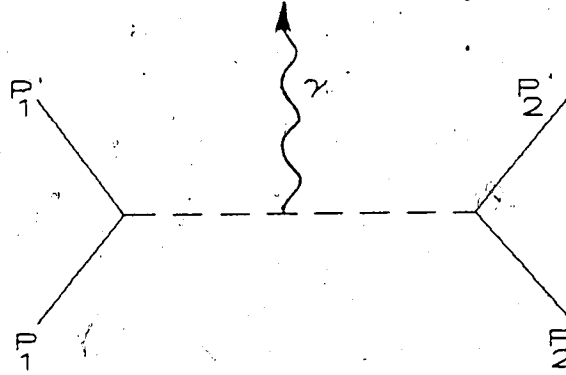


Figure 2.9: Internal emission.

2.2.7 Internal Scattering

The amplitude for figure 2.9 is

$$\begin{aligned} \langle \vec{p}_1', \vec{p}_2', \vec{k} | T_I | \vec{p}_1, \vec{p}_2 \rangle &= \langle \vec{p}_1', \vec{p}_2' | t(E') G_0(E') (\vec{k} | H_{em}^1 | 0) G_0(E) t(E) | \vec{p}_1, \vec{p}_2 \rangle \\ &+ \langle \vec{p}_1', \vec{p}_2' | [1 + t(E') G_0(E')] (\vec{k} | H_{em}^2 | 0) [1 + G_0(E) t(E)] | \vec{p}_1, \vec{p}_2 \rangle \quad (2.18) \end{aligned}$$

where, recall, H_{em}^2 results from the \vec{p} dependence of the nuclear potential.

The evaluation of this amplitude is much more involved than that for external emission ($|T_E|$) because of the intermediate momentum over which an integration must be performed. It has therefore been usual to evaluate ($|T_I|$) to lowest order in an expansion in powers of k , i.e. keeping terms up to k^0 . Explicit calculation shows that the second term of equation 2.18, which results from the potential's momentum dependence, is of order k and therefore doesn't contribute. The first term, arising from emission from internal meson lines, goes as $\frac{\vec{p}_1 + \vec{p}_2}{(p_1 + p_2)_\mu k^\mu} [\dots] + O(k)$ and therefore does not contribute in calculations done in the center of mass system where $\vec{p}_1 = -\vec{p}_2$. The total contribution to the integrated cross section of the internal scattering terms has been estimated to be $\sim 15\%$ at energies close to that of the present experiment [17]. The recent calculation by Fearing et al. also

takes the internal amplitude to zeroth order in the photon momentum over the total available energy.

2.3 Potential Models

The half-off-shell t matrix elements used in the calculations that are compared with the data in chapter 8 were obtained from the Paris and Bonn potentials. These are modern, theoretically based potentials which describe the force in terms of realistic meson exchanges. They lack the large number of free parameters of the more traditional phenomenological potentials such as the Reid and Hamada-Johnston. Both do very well with the elastic scattering data below approximately 300 MeV lab energy and also with deuteron data.

2.3.1 The Paris Potential

This potential is based on dispersion theory at large and intermediate range but with phenomenological short range input. The contributions to the long and intermediate range parts are listed in figure 2.10.

These diagrams correspond to; i) the fundamental second order process of one pion exchange; ii) fourth order uncorrelated two pion exchange; mesonic resonances (σ, ρ, ω and the ϵ); iii) nucleonic excited state contributions; iv) higher order diagrams in two pion exchange. The phenomenological short range contribution is obtained by adjusting parameters to give the best fit

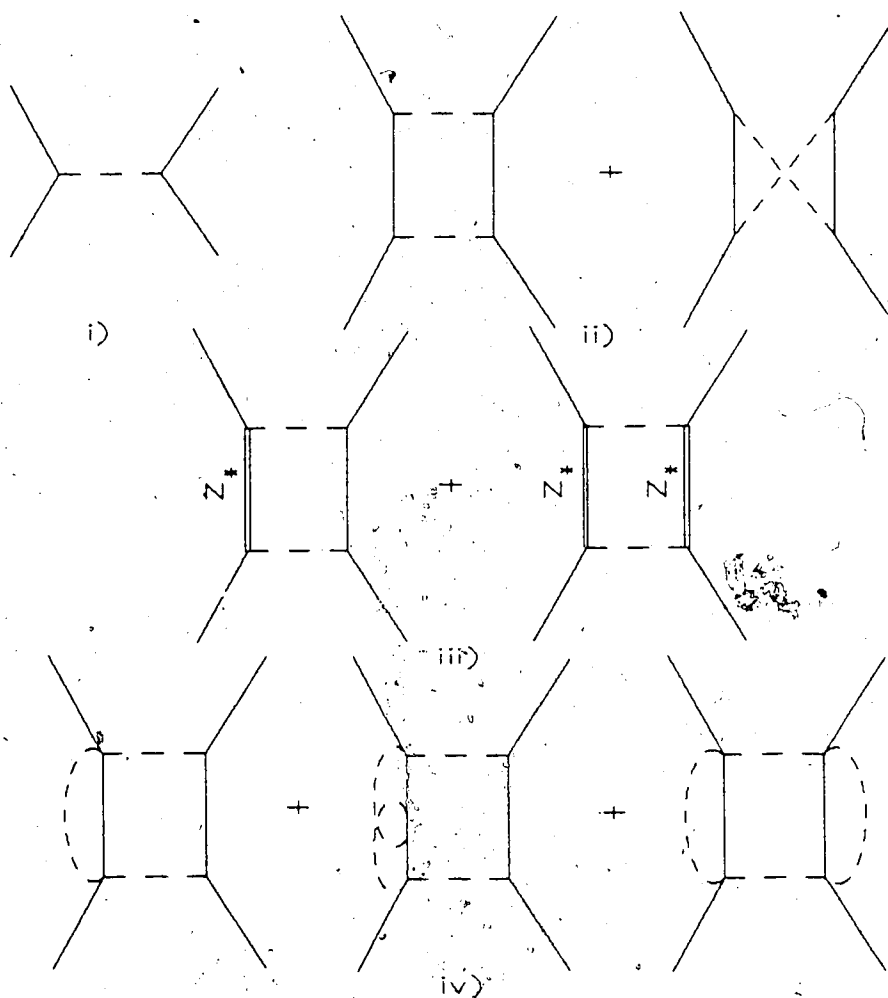


Figure 2.10: Contributions to the Paris nucleon-nucleon potential. Diagrams taken from reference [21]

to all the NN phase shifts below $J=6$, for energies up to 350 MeV.

The general form of the full potential can be written

$$V(r, E) = V_{theor}(r, E)f(r) + V_{phen}(r, E)[1 - f(r)]$$

with E being the CM energy and $f(r)$ a function that sharply suppresses V_{theor} at distances less than ~ 0.8 fm and also minimizes the contribution from V_{phen} for $r > 1$ fm:

$$f(r) = \frac{(pr)^\alpha}{1 + (pr)^\alpha}$$

with $\alpha = 10$. and $p = 1.25 \text{ fm}^{-1}$. As usual both V_{theor} and V_{phen} contain central, spin-orbit, spin-spin, tensor and quadratic spin orbit pieces.

The theoretical part of the potential, V_{theor} , is found to have an energy dependence only in its central piece and here it is weak and approximately linear below the meson production threshold. Also, a best fit to the Livermore [22] energy-independent phase-shift data showed that the central piece of V_{theor} is linear with energy while the other pieces are constant.

The phenomenological part is assumed to be independent of r , leaving it with only an energy dependence, and has a boundary condition imposed such that it remain finite at $r = 0$, i.e. chosen to be a soft-core. With these, the complete form of the potential is

$$V(r, E) = U(r) + EW(r)$$

where $U(r) = U_{theor}(r)f(r) + C[1 - f(r)]$ and $W(r) = W_{theor}f(r) + C'[1 - f(r)]$ with $C' = 0$ for $r > 1$ fm. Thus has 6 free

parameters for each isospin state specified by the constants $C_c, C_{ss}, C_T, C_{so}, C_{so2}$, and C'_c .

For the overall fit of the potential to the Livermore $\bar{p}p$ data, Vinh Mau calculates a χ^2 per data point of 2.5. If the theoretical part $V_{theor}(r, E)$ is not linearized with respect to energy but allowed to keep its full energy dependence and a small energy dependence allowed for the phenomenological tensor piece inside the core, then the χ^2 per data point goes to 1.7 and 3.0 for $\bar{p}p$ and np scattering respectively [21].

2.3.2 The Bonn Potential

The Bonn potential is a field-theoretic approach that has, as its base, a non-covariant³, time-ordered perturbation theory. It differs from the dispersion-theoretic Paris potential in that explicit nucleon-nucleon-meson and nucleon-isobar-meson vertices are obtained and built into a Hamiltonian rather than obtaining a potential parameterized in Yukawa terms which relies on the empirical data of πN and $\pi\pi$ scattering and an arbitrary phenomenological potential for short range. The only phenomenological input to the Bonn potential are coupling constants and cut-off masses (described below), fit to np elastic scattering data below 300 MeV lab energy.

The Bonn potential is "a comprehensive field-theoretic meson-exchange model consisting of all irreducible diagrams (up to fourth order) which by careful, reasonable and realistic consideration are to be included." [23] The diagrams of figure 2.11, plus all possible time orderings, list the contributions to the potential [24]. These diagrams are parameterized in terms of the

³A non-relativistic theory can easily be applied to standard many body theory with applications in nuclear structure.

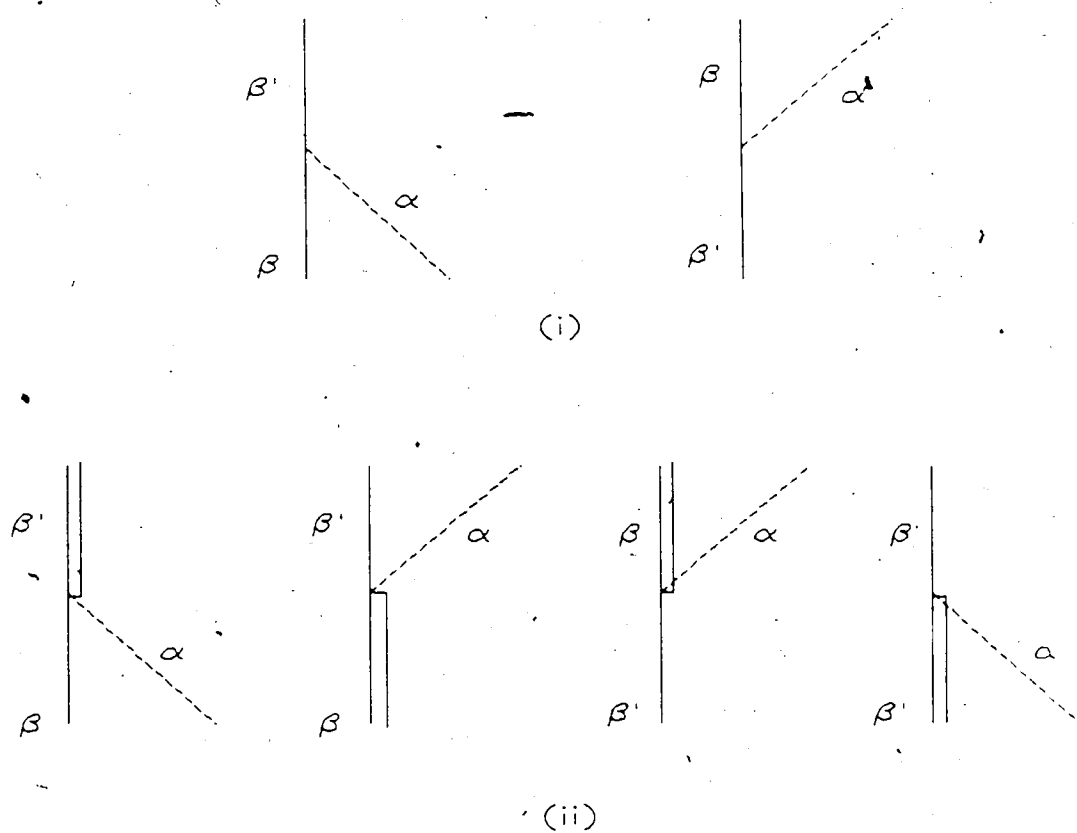


Figure 2.11: Meson-nucleon-nucleon vertices (i), and meson-nucleon-isobar vertices (ii). Diagrams taken from reference [24].

interaction Lagrangians:

$$L_{NN\pi} = \frac{f_{\pi}}{m_{\pi}} \bar{\psi} \gamma^5 \gamma^{\mu} \psi \partial_{\mu} \phi_{\pi} \quad (\pi, \eta)$$

$$L_{NN\sigma} = g_{\sigma} \bar{\psi} \psi \phi_{\sigma} \quad (\sigma, \delta)$$

$$L_{NN\nu} = g_{\nu} \bar{\psi} \gamma_{\mu} \psi \phi_{\nu}^{\mu} + \frac{f_{\nu}}{4m} \bar{\psi} \sigma_{\mu\nu} \psi (\partial^{\mu} \phi_{\nu}^{\nu} - \partial^{\nu} \phi_{\nu}^{\mu}) \quad (\rho, \omega)$$

$$L_{N\Delta\pi} = \frac{f_{N\Delta\pi}}{m_{\pi}} \bar{\psi} \vec{T} \psi_{\mu} \partial^{\mu} \vec{\phi}_{\pi} + h.c.$$

$$L_{N\Delta\rho} = i \frac{f_{N\Delta\rho}}{m_{\rho}} \bar{\psi} \gamma^5 \gamma_{\mu} \vec{T} \psi_{\nu} (\partial^{\mu} \vec{\phi}_{\rho}^{\nu} - \partial^{\nu} \vec{\phi}_{\rho}^{\mu}) + h.c.$$

where the symbol definitions are;

m is the nucleon mass,

m_{α} is the meson mass,

ψ is the nucleon field operator,

ϕ_{α} is the meson field operator,

ψ_{μ} is a field operator describing the Δ -isobar, and

\vec{T} is the isospin transition operator.

Form factors $F^{(\alpha)}(k)$ are applied to the meson-baryon vertices and are a consequence of the extended, or quark-bag, nature of the hadrons:

$$F^{(\alpha)}(k) = \left(\frac{\Lambda_{\alpha}^2 - m_{\alpha}^2}{\Lambda_{\alpha}^2 + k^2} \right)^{n_{\alpha}}$$

where k = momentum transfer, Λ_{α} = cutoff-mass, $n_{\alpha} = 1$ or 2 depending on the coupling. (This form factor suppresses the contribution for high momenta, i.e. small distances.) Λ_{α} is related to the hadron size and therefore determines the range of the suppression. It is however, chosen so as to give the best fits to empirical data and found to range from 1.2 to 1.5 GeV. Therefore, the above diagrams represent all processes up to an exchanged

total meson mass of $\simeq 1$ GeV.

Excellent fits to the data are obtained in all partial waves. Higher partial wave fits, resulting mainly from the one-meson and 2π -exchange contributions, are in close agreement with dispersion theoretic results. When 2π -exchange is supplemented with the two boson-exchange diagrams containing π and ρ , good fits are also obtained in lower partial waves. Further introduction of the $\pi\sigma^4$ and $\pi\omega$ diagrams gives more consistency in the values for the cutoffs for the πNN and $\pi N\Delta$ vertices, 1.3 and 1.2 GeV respectively. The model also gives excellent predictions for the deuteron and low energy nucleon scattering parameters: the scattering length 'a' and the effective range 'r' in both singlet and triplet states [24].

Although no explicit comparison to nuclear matter experiments has so far been performed, it is suggested [24] that inclusion of the fourth order diagrams in conjunction with isobar excitations has the effect of reducing nuclear binding, i.e. better saturation: a problem that afflicts most conventional potentials.

2.4 The Soft Photon Approach

The basis of the Soft Photon Approach (SPA) is a theorem, attributed to Low [25] 1958, that says it is possible to obtain an amplitude, $M_{NN\gamma}$, to zeroth order in photon momentum for the process $N + N \rightarrow N + N + \gamma$ from a

⁴ σ here stands for the sum of all $\pi\pi$ and $\pi\rho$ diagrams.

knowledge of the $N + N \rightarrow N + N$ phase shifts and the static electromagnetic moments of the particles involved. As such, this approach says nothing about off-shell effects, (it contains only on-shell input). It is however useful as a check on other potential model calculations as these two approaches should converge in the limit $k_\gamma \rightarrow 0$.

What was interesting about the SPA, and in fact was one of the motivations for doing a new experiment, was that data from all prior $pp\gamma$ experiments fit the calculation as well or better than they fit potential models, even in geometries in which the interaction was known to be far off-shell. This unexpected result in part motivated the present experiment which featured greatly improved statistics and a measurement of the analysing power, which, of course, does not have the associated normalization problems of the cross section.

The derivation of the amplitude for $pp\gamma$ through SPA will be outlined below following a description by Fearing [26]. First, the amplitudes for the external emission graphs (section 2.2.6) are expanded in a power series, for both the p-p off-shell and the photon creation factors, about an on-shell point.⁵ The external emission graphs contain all the $O(1/k)$ pieces plus higher order pieces. To make the amplitude gauge invariant, further $O(k^0)$

⁵In the Low prescription, the on-shell point is chosen as an average energy and momentum transfer. Feshbach and Yennie [27] however, have obtained a prescription that avoids the expansion in energy: useful at low energies where the NN amplitudes depend strongly on energy.

terms are added. One then arrives at an amplitude

$$M_{NN\gamma} = \frac{A}{k} + B + Ck.$$

'A' contains kinematic factors, the elastic NN amplitudes and only charge terms from the photon creation. 'B' contains kinematic factors, the elastic amplitudes and also their derivatives, and charge and anomalous magnetic moment terms. 'C' contains all terms of higher order in k , i.e. $C \equiv C(k)$. (Strictly speaking A and B are also functions of k but this dependence arises from the kinematics and is completely known.) This term contains the off-shell terms, higher order on-shell terms, contributions from internal emission, and others.

The cross section is

$$d\sigma \sim k |M_{NN\gamma}|^2 \sim \frac{A^2}{k} + 2\text{Re}AB^* + (B^2 + 2\text{Re}AC^*)k + 2\text{Re}BC^*k^2 + C^2k^3$$

where the k factor, multiplying the square of the amplitude, comes from phase space.

The soft photon theorem says that the A^2 , $2\text{Re}AB^*$, and the B^2 part of the $O(k)$ term come strictly from on-shell information. In fact, a theorem due to Burnett-Kroll [28], allows one to obtain the first two terms $A^2/k + 2\text{Re}AB^*$, from only a knowledge of the unpolarized elastic cross section, i.e. $|M_{NN}|^2$. For the spin polarized case, the first two terms in the polarized $NN\gamma$ cross section can likewise be obtained from a knowledge of the polarized NN cross section through an extension of the Burnett-Kroll theorem due to Fearing [29]. To obtain the B^2 term in either case, phase shifts are needed.

Fearing [26] has investigated the contributions of the various unknown terms to the differences between the SPA, a potential model calculation (H.J.), and the results of a number of prior $pp\gamma$ experiments performed at various energies and geometries. These are, a 42 MeV Manitoba [4], a 200 MeV TRIUMF [7] and a 730 MeV UCLA [6] experiment. In general, both the energy and geometry were found to be important factors in determining which of the unknown terms were being investigated by the experiment. Also, the SPA was found to qualitatively fit the data and quantitatively differ from it by amounts of the order of the size of the experimental errors. As chapter 7 indicates, this result no longer holds true in the case of the present experiment.

Chapter 3

A Brief Overview of the Experiment

This chapter is only an overview, intended to allow the reader to form an integrated perspective of the entire experiment. Complete and detailed information on each component is left to the following chapters.

3.1 TRIUMF, The Facility

TRIUMF, an acronym for Tri (three) University Meson Facility, is a 500 MeV H^- cyclotron facility that began operating in 1974 under the joint direction of the University of Alberta, University of British Columbia, Simon Fraser University and the University of Victoria, the original three B.C. universities having been joined by the University of Alberta in 1968.

Through the use of accelerating dees, supplied with an RF voltage, and a magnetic dipole field, either polarized or unpolarized H^- ions are accelerated to any desired energy between 180 and 520 MeV. The beam is extracted

by inserting a carbon 'stripper' foil at a radius appropriate to the required energy. This foil strips the two electrons from the ion, leaving it a bare proton of opposite (i.e. positive) charge thus causing a reversal in its direction of curvature in the magnetic field and resulting in the exit of the proton from the cyclotron.

Two stripper foils provide extraction at two different points allowing simultaneous extraction of separate proton beams with different energies. One of the extraction beamlines is dedicated to proton and neutron experiments and the other, through the use of meson production targets, to meson experiments and pion cancer therapy.

The H^- ions are produced with either an Ehlers[30] type hot filament unpolarized source (1-2 mA at 12 KeV), or a Lamb shift [31] polarized source ($0.6\mu\text{A}$ with $\sim 80\%$ polarization). The ions are confined by a buncher to sharp pulses lasting ~ 5 ns and spaced 43.6 ns apart, to match the RF of the accelerating voltage across the dee and injected into the center of the cyclotron. The macroscopic duty factor is 100%, and the intensity of the extracted beam may be controlled by adjusting the vertical depth of penetration of the stripper foil into the circulating beam or by choosing a foil of appropriate thickness.

The entire injection, accelerating and extraction facilities, are kept under a vacuum of $\sim 10^{-7}$ torr to avoid beam dispersion and premature stripping of the H^- ions.

For this experiment a 280 MeV polarized proton beam of ~ 13 nA was

extracted through beamline 1B (figure 4.1). Control elements of this line consist of:

1. a dipole bending magnet 1BVB2 to direct protons into the secondary beamline 1B,
2. a number of beam focusing quadrupoles, 1BQ7, 1BQ8 and 1BQ9,
3. a vertical steering magnet 1BSM4 and a horizontal bender 1BVB3.

Monitoring of the beam position and focus was attained through 'vertical wire' monitors, M5 to M7, which gave both horizontal and vertical profiles of the beam.

Beam polarization, and intensity, were monitored by a polarimeter which counted left and right coincidences for elastic scattering of the polarized protons off a CH_2 target.

Beam current was also measured by a secondary emission monitor, SEM, located downstream of the target. (The number of secondary atomic electrons knocked out by the beam protons from the SEM's 21 constituent aluminum plates, and collected through a potential difference is proportional to the beam current.)

Finally, a beam dump composed of iron plus concrete shielding, to reduce back scattering into the experimental area, absorbed the protons at the end of the line.

3.2 The Experiment

All three final state particles, i.e. two protons and the photon, were detected in order to overconstrain the kinematics and thus reduce background. Components of the experimental setup are described below and depicted in figure 3.1.

3.2.1 Target

The source of the $p\bar{p}\gamma$ events was a liquid hydrogen target contained within an evacuated scattering chamber located at 1BT1 (figure 4.1). The target consisted of a 1 meter long cylindrical flask 6.8 cm in diameter, oriented parallel to the beam, figure 3.2. Only the central 1.59 cm radius and 5 mm thick portion of the flask contained liquid hydrogen. Next to the liquid, on both sides, was 487.5 mm of H_2 gas at 1 atmosphere pressure, separated from the liquid by thin copper coated Kapton windows. The gas provided spatial separation of the thick beam entrance and exit windows from the liquid target region. Background originating from the entrance and exit windows was then reduced by shielding the detectors and rejecting, in the software with the aid of vertical drift chambers (VDC's), those events that came from the window regions.

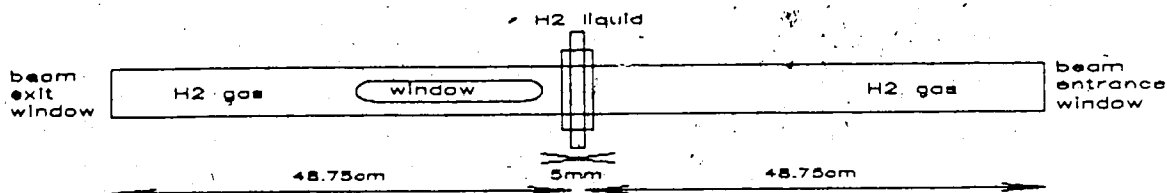


Figure 3.2: Hydrogen target flask. Only the central 5 mm portion contains liquid H₂

3.2.2 Proton Detection

The two final state protons were detected within a few degrees of the horizontal plane containing the beam line, and in a polar angle range of $\sim 10^\circ$ to 30° on both sides of the beam line.

Because the detection systems of the two protons differed, in what follows a distinction will be made by referring to the proton detected on the same side of the beam line as the photon as the 'low energy proton' (LEP), and that detected on the opposite side as the 'high energy proton' (HEP), which, in general, had higher energy than the LEP.

LEP Detection

The LEP's were detected inside the evacuated scattering chamber because in certain kinematic regions of interest the energy of the proton dropped to as low as 4 MeV. Five 6.35 mm thick plastic scintillators, each subtending a polar angle of approximately 4° at the target, were used to obtain both

energy and time of flight information and formed part of the event trigger.

HEP Detection

The HEP was momentum analysed with a spectrometer consisting of a 'C' type dipole magnet and four vertical drift chambers. By measuring the relative drift times of ionization electrons originating along the track of the proton to a set of three anode wires, these chambers are capable of giving track position information to an accuracy of $\pm 0.15\text{mm}$. The proton's angle of incidence and its time of passage through the chambers were also obtained from the VDC's. Two chambers in front of the magnet gave both the initial scattering angle of the proton and the location of the event vertex within the target cylinder. Two chambers after the magnet, in conjunction with those in front, gave the angle through which the proton was bent by the magnetic field, i.e., a measure of its momentum.

An array of eight 3.18 mm thick plastic scintillators, parallel to and directly behind the final VDC, gave the time of flight information for the HEP and formed part of the event trigger.

3.2.3 Photon Detection

Sixteen lead glass cerenkov counters, each subtending between $\sim 5^\circ$ and 11° and spanning the polar range 15° to 170° on the same side of the beam line as the LEP detectors, gave the approximate energy and scattering angle of the photon. Detection of a photon provided the delayed stop for the LEP

and HEP time of flight determination and completed the event trigger.

3.2.4 Background Elimination

Simultaneous detection of all three final state particles kept the random background well below that suffered in all prior $pp\gamma$ experiments. However the random triple coincidence rate observed in preliminary test runs, approximately $5000/nC$ was still much too high to be tolerated by our acquisition system. By far the biggest contribution to this rate came from pp elastic scattering off the various target regions in conjunction with beam induced neutron background triggering the cerenkov counters.

Some of this background was reduced with an absorber-veto combination behind both the LEP and HEP detection scintillators. Behind the eight scintillators on the HEP side were copper plates thick enough to absorb the highest energy $pp\gamma$ proton allowed by the kinematics plus approximately 3% for range straggling and thin enough to allow elastics to penetrate and be detected by the veto counters. The veto counters were 3.18 mm thick, oversized plastic scintillators put in anti-coincidence with the HEP detectors¹. A similar absorber-veto combination was used on the LEP side except that CH_2 was used as the absorbing material in order to minimize photon losses to the two cerenkov detectors behind. For typical beam currents of ~ 13 nA, the absorber-veto systems decreased the average HEP, LEP detector singles

¹i.e. if a signal was detected in both the HEP detector and its veto counter the event was rejected since only elastically scattered protons would have enough energy to penetrate the Cu absorber.

rates from $5.0 \times 10^4/\text{s}$, $2.0 \times 10^5/\text{s}$ to $3.0 \times 10^4/\text{s}$ and $8.0 \times 10^4/\text{s}$ respectively.

The proton detectors were directly shielded from viewing the target cylinder end windows by stainless steel absorber, except from the upstream window on the LEP side for which Teflon was used to reduce photon absorption.

A 3.18 mm thick plastic scintillator in front of every cerenkov counter vetoed charged particles. Singles rates with and without these vetos averaged $2.7 \times 10^3/\text{s}$ and $3.0 \times 10^3/\text{s}$ respectively².

In addition to the large background flux of elastically scattered protons, a large neutron component, probably from (p,n) interactions at the beam dump, was observed in the HEP detection branch during a sweep of the experimental area with a liquid scintillator. Even considering the relatively low detection efficiency for neutral particles in plastic, the large flux made it necessary to place two large scintillators, spanning the HEP detection region, in coincidence with the HEP trigger scintillators. Singles rates with and without these extra scintillators averaged $2.0 \times 10^4/\text{s}$ and $3.0 \times 10^4/\text{s}$ respectively.

3.2.5 Electronics

A triple coincidence required satisfactory pulse heights at the discriminator from at least one of each of the detector types, and the correct detector-veto coincidences / anticoincidences as depicted in figure 3.3. If the pulse height responses were favorable, an event was formed by a triple coincidence at the

²Values are for a typical beam current of 13 nA.

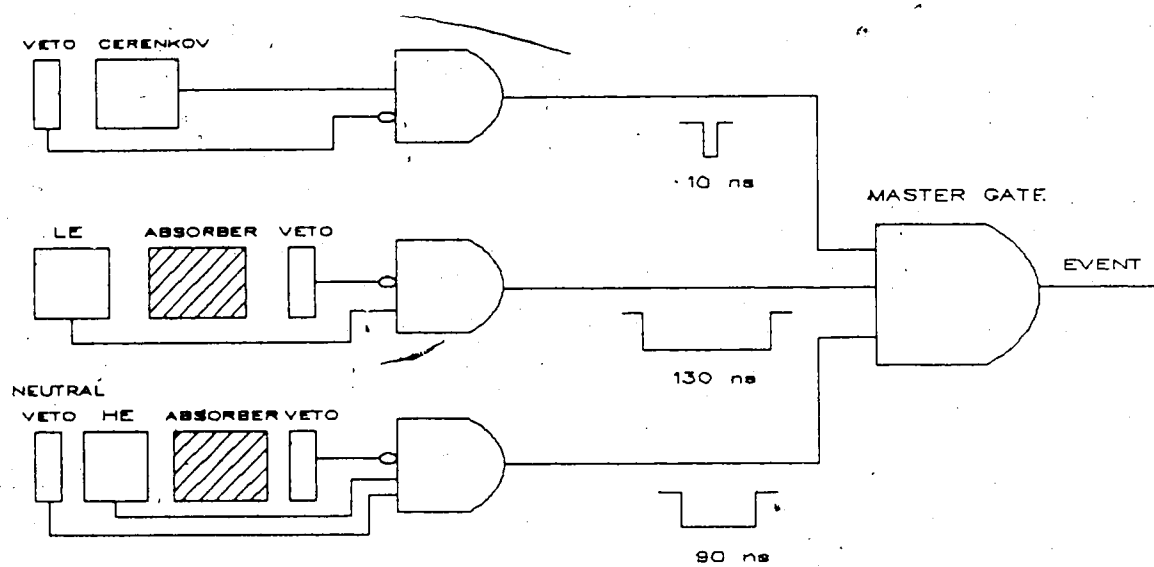


Figure 3.3: Coincidences required for a 3-coincidence event.

master gate. For such an event the following quantities were recorded:

1. For the LEP,
 - (a) energy deposited in the plastic, measured with analog to digital converters (ADC's) that integrated the output pulse from the plastic over a fixed time period,
 - (b) its time of flight, measured with time to digital converters (TDC's).
(The delayed photon detection provided the stop. The overall time resolution was a couple of nano seconds.)
2. For the HEP,
 - (a) its momentum, via the C-magnet spectrometer,
 - (b) its flight time, measured with TDC's.
3. For the photon,
 - (a) energy deposited in the cerenkov counter, measured with ADC's,
 - (b) the photon-cyclotron RF time: later used to eliminate background not directly associated with a beam burst.
4. For all particles the polar and azimuthal angles, θ and ϕ were known to within the solid angle subtended by the particular detector.

Three particles in the final state means 9 independent degrees of freedom. With the constraints of energy and momentum conservation, i.e. kinematics, this number is reduced to 5. In total this experiment measured the

11 quantities enumerated above (only 5 being independent). Thus the $pp\gamma$ events were well overconstrained, a fact evident in the excellent background rejection attained.

To determine the amount of background that did remain, two types of triple coincidences were recorded, 'prompt' and 'delayed' events. A prompt event was one in which all three final state particles came from the same beam burst. These could be either real $pp\gamma$ events or random triple coincidences. A delayed event was one in which at least one of the particles came from a different beam burst and was therefore definitely a random event. (These were accepted by making the widths of the proton detector output pulses, at the master gate, wide enough to allow particles from different beam bursts to form a coincidence. See figure 3.3.) The component of prompt random triples mixed in with the real prompt $pp\gamma$ events was then determined from the number of delay random events. Delay random events were recorded for the cases in which two particles came from the same beam burst and also in which no particle came from the same burst.

A sample of pp elastic scattering events, single coincidences requiring a HEP trigger scintillator and its elastic veto in coincidence, was taken simultaneously along with triple coincidences for cross section normalization.

Also collected were pulser events, obtained by sending electrical pulses to light emitting diodes attached to each particle detector. These were used to monitor gain shifts and the dead time of the system. Dead time was obtained from the ratio of the number of pulses recorded on tape to the number submitted to the system.

Information from the following electronic modules constituted the event data words:

1. TDC's — recorded flight time information and also the raw time data from each individual VDC wire (used for determining track position and direction information).
2. ADC's — recorded deposited energy information for the LE protons and the photons.
3. Scalers — recorded various coincidence and singles rates.
4. Digital Coincidence Registrar (DCR) — recorded the event type, e.g. pulser, elastic or $pp\gamma$, and spin condition.

3.2:6 Computer Acquisition

A schematic diagram of the event acquisition system is shown in figure 3.4. Having defined a candidate for an event through the electronics, an Eclipse S230 computer read the data words and decided, based on a small number of tests, whether the event would be stored on magnetic tape for further processing or rejected. An electronic latch prevented another event from coming along and overwriting the data before the computer had completed reading the previous event. The trigger rate at a beam current³ of 13 nA

³An average current ~ 13 nA was chosen as a compromise after considering factors such as, dead time, random triple rate and the $pp\gamma$ event rate.

was $\sim 50/s$ with a dead time of $\sim 30\%$. Only 0.6% of all accepted events were $pp\gamma$'s giving a real count rate of one event every 4 seconds.

The on-line acquisition analysis was kept short in order to minimize the dead time of the system. The only events rejected by the software were those with missing drift chamber planes or those whose cerenkov-cyclotron RF time difference was too large for the event to be directly associated with a 5ns wide beam burst. To determine the correction to the data for the drift chamber misses, 3% of all events that triggered the electronics were put directly on tape without any processing whatsoever.

Only those characteristics which were essential for monitoring the operating condition of the system were monitored on-line. These included all scalers and a spectrum of the position of the event vertex at the target, along an axis parallel to the upstream drift chambers. Together, these gave a qualitative indication of the target status and the quality of the beam tune. A more quantitative measure of beam quality was obtained by dividing the rate of the triple coincidence events by the cube of the beam current. For random events, which scale as the cube of the current, this quantity is independent of the beam current and therefore gives a 'current normalized' measure of the random background.

3.2.7 Semi-on-line Analysis

It took approximately 45 minutes to fill a 1600 bpi, 2400 ft tape with data.

The full tape was then taken to an Eclipse S200 computer for further 'semi-

on-line analysis. This analysis was primarily for monitoring the hardware more closely and identifying $pp\gamma$ events. For example, the gains of all detectors were monitored by noting the position of the pulsers within the ADC spectra. $pp\gamma$ events were identified by looking for kinematic loci on the following spectra:

1. HEP angle of bend through the spectrometer versus the photon scattering angle. (Figure 5.6.)
2. LEP time of flight versus HEP time of flight. (Figure 5.1.)
3. LEP time of flight versus LEP deposited energy. (Figure 5.3.)

3.2.8 Data Runs

Data was acquired in two consecutive ~ 4 week periods in January and June of 1985. In January, with a large angle configuration (LAC), corresponding to HEP detection between 20° and 30° , approximately 80,000 $pp\gamma$ events were obtained out of a background of $\sim 10,000,000$ random triple events. In June, with a small angle configuration (SAC), corresponding to HE detection between 10° and 20° , approximately 60,000 $pp\gamma$ events were obtained out of an even larger background.⁴ In total some 200 data tapes were obtained each containing about 120,000 events of which $\sim 0.6\%$ were $pp\gamma$ events.

⁴The cross section for the major background contributor, pp elastic scattering, increases as the HEP scattering angle decreases.

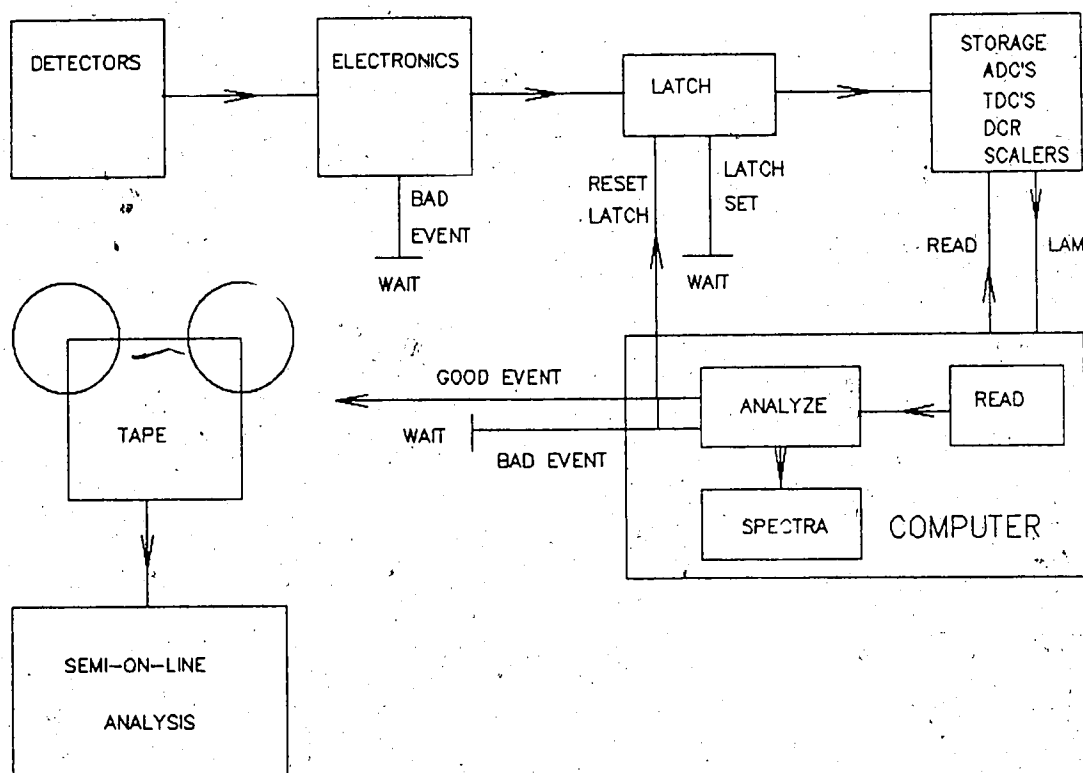


Figure 3.4: Schematic diagram of the event acquisition. The label 'WAIT' in the diagram refers to the systems waiting for another event to come along while the electronic latch is open. The 'look at me' (LAM) signal, issued to the computer by the crates containing the ADC's and TDC's, informs the computer that an event has been accepted. The computer then responds by reading the event data words.

3.2.9 Data Reduction

After data collection, a more complete analysis program selectively discarded those events that did not satisfy limits on various $pp\gamma$ kinematic loci. Some events were spared from this "skimming" process, namely; the HE prescaled elastic sample, pulser events, and the 3% sample of unprocessed events. For all other events the following loose cuts were applied:

1. Photon detection time minus cyclotron RF time. (Narrower than that used during acquisition.)
2. HEP bend angle through the spectrometer. (Just tight enough to remove most of the elastic events.)
3. LEP time of flight corrected for kinematics.
4. HEP time of flight corrected for kinematics and path length differences.

These cuts reduced the amount of random data by a factor of 5 leaving about 40 "condensed" tapes for further processing.

3.2.10 Analysis

The bremsstrahlung and elastic data were analysed on both a Digital VAX 780 and VAX 8600, using event processing and histogramming routines of the program "Perseus" [32].

pp γ Analysis

A test on the origin of the event vertex within the liquid portion of the target was first applied to all the data.

The data was then divided into 480 bins according to θ_γ , ϕ_γ , θ_{LE} , ϕ_{LE} , and θ_{HE} , ϕ_{HE} . The photon and LE proton bins were defined by the physical limits of their detectors while the HE protons were binned by dividing the drift chamber coverage of 20° polar angle into 6 equal angle bins. Dividing the data into such a large number of bins placed tight constraints on the kinematics of a particular bin. Very good background subtraction was therefore attained by applying the following cuts separately to each bin;

1. proton bend angle through the spectrometer,
2. energy deposited in the LEP detectors,
3. LEP time of flight,
4. HEP time of flight.

The average accidental random background remaining after these cuts was about 1.2%. Individual bins however had background ranging from ~0% to 12%. On the whole background remained higher in the SAC than in the LAC because of the larger elastic cross section at smaller angles. Figure 3.5 shows the enhancement of real to random events after application of all tests excluding the test on the bend angle.

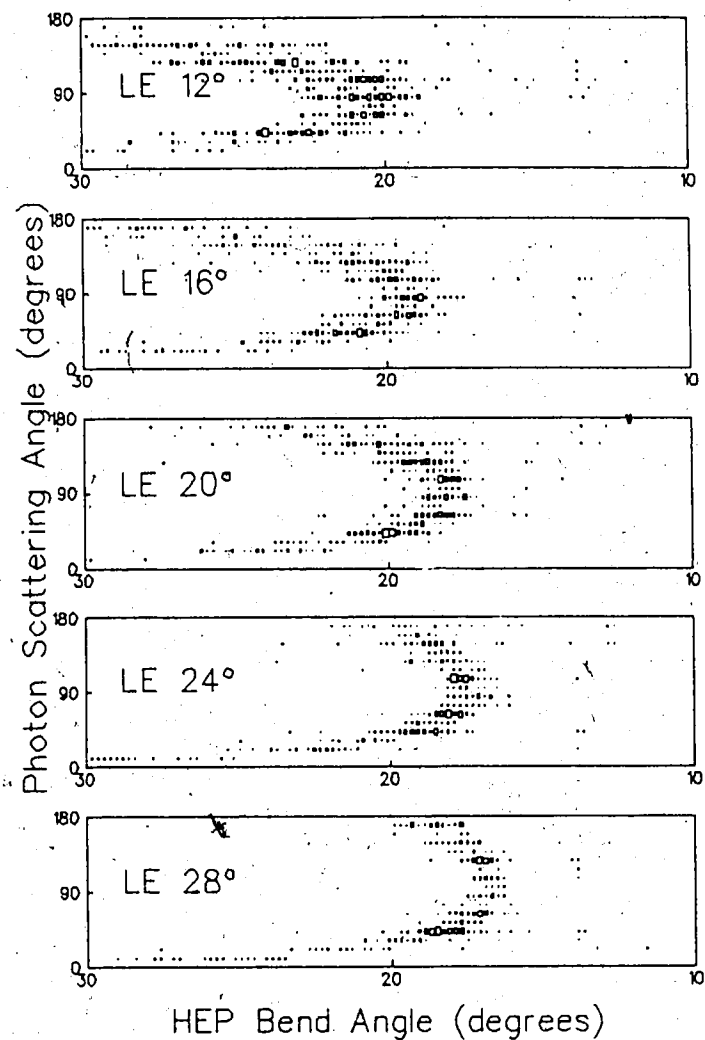


Figure 3.5: HEP angle of bend through the spectrometer versus photon scattering angle. After application of all tests excluding the test on abscissa. HEP bin centered at 17.5° .

3.2.11 Analysing Powers

The polarization of the incident beam was cycled through 3 minutes of spin up, 1 minute of spin off, 3 minutes of spin down and 1 minute of spin off.

The analysing power, A_y , for the $pp\gamma$ interaction was defined as

$$A_y = \frac{(N^\uparrow - R^\uparrow)/n_{inc}^\uparrow LT^\uparrow - (N^\downarrow - R^\downarrow)/n_{inc}^\downarrow LT^\downarrow}{P^\uparrow(N^\uparrow - R^\uparrow)/n_{inc}^\uparrow LT^\uparrow + P^\downarrow(N^\downarrow - R^\downarrow)/n_{inc}^\downarrow LT^\downarrow}$$

where $N^{(\uparrow\downarrow)}$ is the number of prompt events, (all particles coming from the same beam burst), with spin up(down) passing all $pp\gamma$ tests for a particular bin.

$R^{(\uparrow\downarrow)}$ is the number of random events, (different beam bursts), with spin up(down) passing all $pp\gamma$ tests.

$n_{inc}^{(\uparrow\downarrow)}$ is the number of incident protons, proportional to the total charge collected by the SEM in the spin up(down) mode.

$LT^{(\uparrow\downarrow)}$ is the live time of the system in the spin up(down) mode, determined from the pulser events.

$P^{(\uparrow\downarrow)}$ is the polarization of the incident beam in the spin up(down) mode.

Chapter 7 contains a complete description of the analysing power, its error, and plots of the data compared with various theoretical calculations.

3.2.12 Differential Cross-Section

The three-fold differential cross sections, $\frac{d^3\sigma}{d\Omega_{HE}d\Omega_{LE}d\theta_\gamma}$, were calculated as follows:

For the incident beam polarized data

$$\left. \frac{d^3\sigma}{d\Omega_{HE}d\Omega_{LE}d\theta_\gamma} \right|_{\parallel} = Z \frac{1}{P^\parallel + P^\perp} \left[\frac{P^\parallel(N^\parallel - R^\parallel)}{n_{inc}^\parallel LT^\parallel} + \frac{P^\perp(N^\parallel - R^\parallel)}{n_{inc}^\perp LT^\parallel} \right]$$

and for incident beam unpolarized data,

$$\left. \frac{d^3\sigma}{d\Omega_{HE}d\Omega_{LE}d\theta_\gamma} \right|_0 = Z \left[\frac{N^0 - R^0}{n_{inc}^0 LT^0} \right]$$

Here $Z = \frac{\epsilon(\Delta\Omega)n_{tgt}}{\Delta\Omega_{HE}\Delta\Omega_{LE}\Delta\theta_\gamma}$, where $\epsilon(\Delta\Omega)$ is a Monte Carlo correction factor, for the given bin $\Delta\Omega$, that corrects for such things as finite acceptance, detector efficiency, multiple scattering, etc. These are of course bin dependent. (Chapter 6 gives a complete description of the Monte Carlo.)

n_{tgt} is the number of target protons per unit volume and t is the target thickness.

N^0, R^0, LT^0 , and n_{inc}^0 have the same definitions as $N^{\parallel(1)}, R^{\parallel(1)}, LT^{\parallel(1)}$, and $n_{inc}^{\parallel(1)}$ except that they are for the unpolarized beam mode.

The total differential cross section combining the unpolarized with polarized data is

$$\sigma = \frac{\sigma^{\parallel(1)}/(\delta\sigma^{\parallel(1)})^2 + \sigma^0/(\delta\sigma^0)^2}{1/(\delta\sigma^{\parallel(1)})^2 + 1/(\delta\sigma^0)^2}$$

where σ is short for $\frac{d^3\sigma}{d\Omega_{HE}d\Omega_{LE}d\theta_\gamma}$ and $\delta\sigma$ is the statistical error in the cross sections.

A complete description of the cross section and its error, along with plots of the data and various theoretical calculations, are given in chapter 7.

Chapter 4

Apparatus, Detector Calibration, Detector Timing

4.1 Apparatus

4.1.1 Beam Control

Figure 4.1 shows the components of the beam line used in controlling and monitoring the beam parameters. These consist of: dipole, horizontal benders VB2 and VB3; beam focusing quadrupoles Q7, Q8, and Q9; a vertical steering magnet SM4; beam profile wire monitors M5 and M6; vacuum valves VA7 and V8; a polarimeter; a secondary emission monitor (SEM); and a beam dump. Beam halo was reduced with a 2.5 cm diameter tungsten collimator located between M5 and the polarimeter, and a 1.59 cm diameter, 8.89 cm long copper collimator located just upstream of the scattering chamber. The beam dump, SEM, and polarimeter were surrounded by a large amount

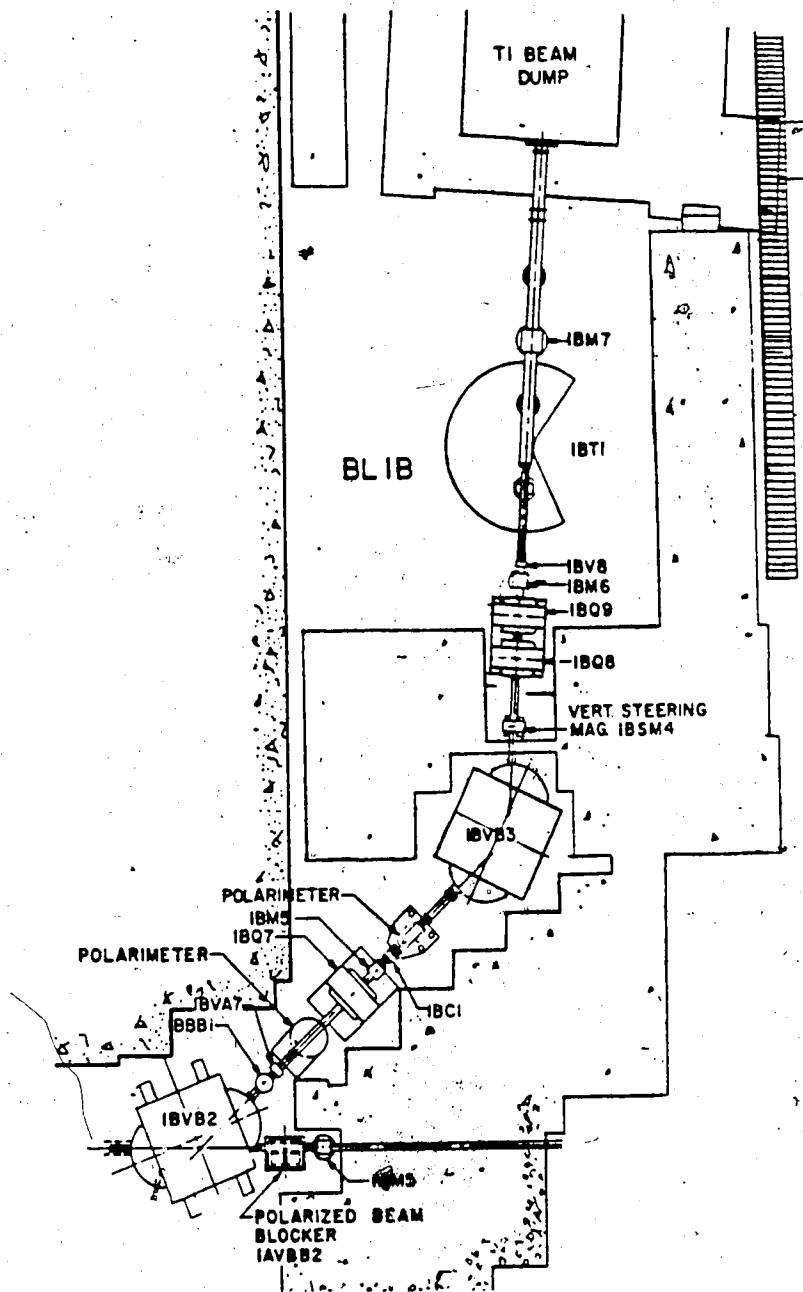


Figure 4.1: TRIUMF's 1B beamline.

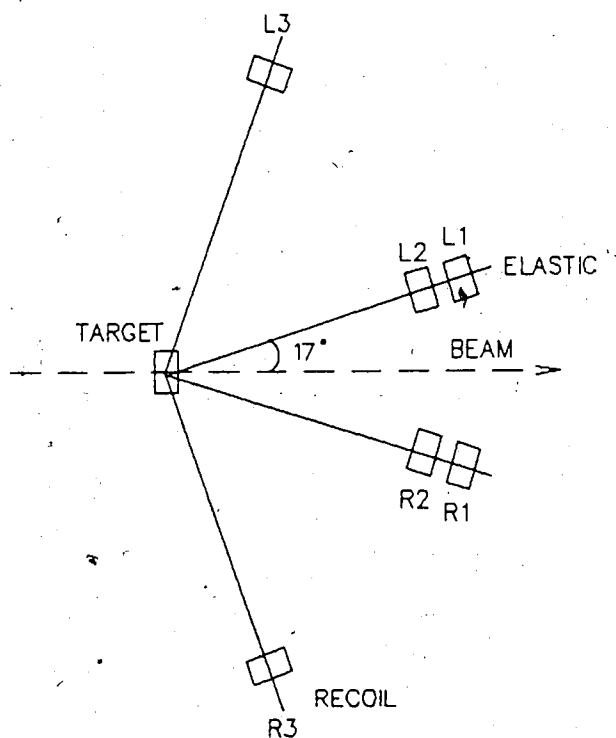


Figure 4.2: The pp elastic polarimeter.

of concrete and lead to minimize the background within the area from the beam halo.

4.1.2 Polarimeter

Beam polarization and intensity were monitored with a polarimeter that utilized pp elastic scattering at 17° lab of the beam from the hydrogen in a 5.36 mg/cm^2 thick CH_2 target (figure 4.2).

The beam polarization is calculated from the number of left and right scattered protons and a knowledge of the CH_2 pp elastic analysing power at 17° lab. A left event is defined as a coincidence between the pair of

detectors, L1 and L2 at 17° and the plastic recoil proton detector, R3. Similarly a right event requires a coincidence between detectors R1, R2, and L3. Accidental contributions to these prompt events were determined by counting the same coincidences but with R3 and L3 delayed by 43 ns (1 beam burst). The background contribution from the carbon in CH_2 was determined by replacing the CH_2 target with carbon and taking data. (Carbon was found to contribute 9.9% to the left plus right counts at 280 MeV.) Beam polarization is then given by

$$P = \frac{1}{A(\text{CH}_2)} \cdot \frac{(L - L_{\text{acc}}) - (R - R_{\text{acc}})}{(L - L_{\text{acc}}) + (R - R_{\text{acc}})}$$

where L, R = the number of left, right polarimeter coincidences, $L_{\text{acc}}, R_{\text{acc}}$ = the number of left, right accidental coincidences, A = the analysing power of the polarimeter (i.e. considering the contribution of the carbon in CH_2), determined to be 0.372 at 280 MeV and 17° lab, (see section 7.1). Average values of the polarization in the spin up and down modes were respectively, 73.6% and 76.6% in the LAC and, 78.0% and 74.2% in the SAC. These values have been corrected for the small instrumental asymmetry in the polarimeter, obtained from the measured polarization of the beam in the spin off mode, of 4.4% (LAC) and 3.4% (SAC).

4.1.3 SEM

The secondary emission monitor (SEM) provided a more accurate measurement of the number of incident protons by measuring the charge, collected through a potential difference, from atomic electrons knocked out of its 21

constituent aluminum plates by the proton beam. This was calibrated in a separate run, shortly after the data taking runs, with a Faraday cup (a device that measures the total number of beam protons by measuring the charge collected on an insulated cylindrical conductor).

4.1.4 Scattering Chamber

A diagram of the scattering chamber, containing the liquid H_2 target and the LEP detectors, is given in figure 4.3. Its shape outlined the objects enclosed in order to reduce the surface area and thus lessen the total force of atmospheric pressure. Three sections, a base, mid-section, and a lid were bolted together and kept vacuum tight with greased 'O'-ring seals. The mid-section was of $20.3 \text{ cm} \times 7.6 \text{ cm}$ aluminum C-channel, 0.64 cm thick on the photon detection side and 1.27 cm thick on HEP detection side, designed to allow photon penetration and maintain structural support under vacuum. The base and lid were of 2.54 cm thick aluminum, reinforced with aluminum channel webbing.

The HEP's exited the scattering chamber through a $10.2 \text{ cm} \times 50.8 \text{ cm}$, 0.127 mm thick Kapton window sealed between aluminum plates and bolted to the chamber against an O-ring seal. Five ports in the chamber lid, for the LEP detectors, allowed these protons to be detected within the vacuum. This was necessary because in certain kinematic situations their energy leaving the target drops to as low as 4 MeV. Only the plastic scintillators were within the chamber. The phototubes for these scintillators were located outside

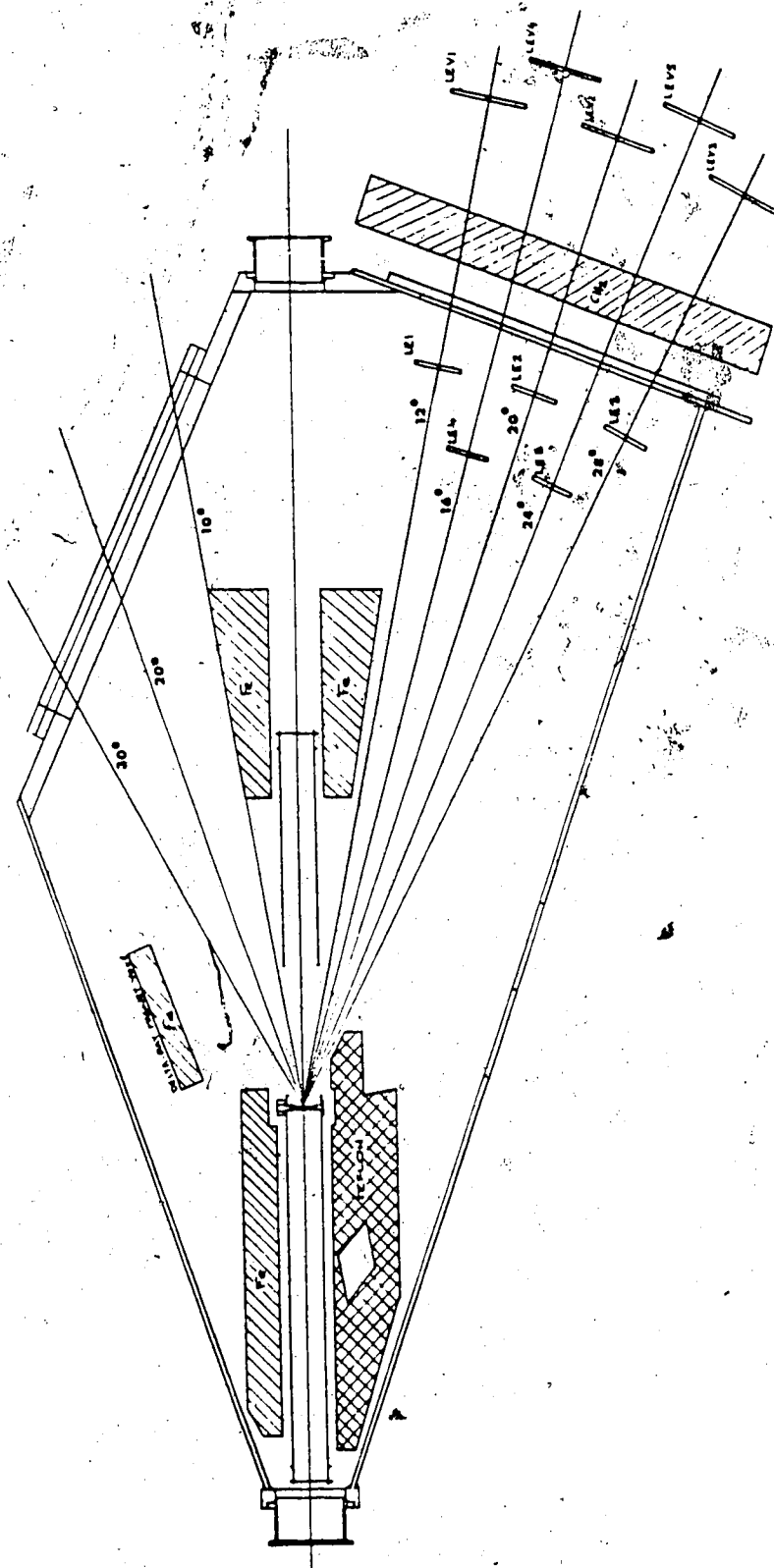


Figure 4.3: Scattering chamber containing the hydrogen target and the LE proton detectors.

the chamber, and coupled to them through plastic light guides sealed in the chamber lid. Stainless steel and Teflon absorbers bolted to the lid provided shielding for the LEP and HEP detectors from beam scattering off the walls and end caps of the H_2 target cylinder. A 360 gauss permanent magnet suspended from the lid prevented δ -rays¹ from reaching the LEP detectors. Mounting all components from the inside lid allowed easy access to the target at beam height by dropping the mid-section and base as one unit.

The whole chamber assembly was supported from above by an aluminum brace suspended from 'I' beams resting on concrete shielding blocks. During the experiment the chamber had proved leak tight to $\sim 10^{-6}$ torr.

4.1.5 Liquid Hydrogen Target

A cylindrical 5 mm thick and 3.18 cm diameter liquid hydrogen target was contained at the center of a 1 m long 6.8 cm diameter stainless steel tube, located at 1BT₁ inside the scattering chamber. Figure 4.4 gives a number of cross sectional views through the target.

The length of the 1 m tube, minus the 5 mm liquid portion, was filled with H_2 gas at the same pressure as the liquid, (1 atm.). The gas separated the liquid from the thick (0.025 mm stainless steel), potentially background contributing, target cylinder end caps. Thin (0.0076 mm Kapton, coated with 1000 Å Cu) windows separated the liquid from the gas. Two .051 mm kapton windows in the side of the downstream 1/2 m section of the tube

¹Atomic electrons ionized from the hydrogen by the incident protons.

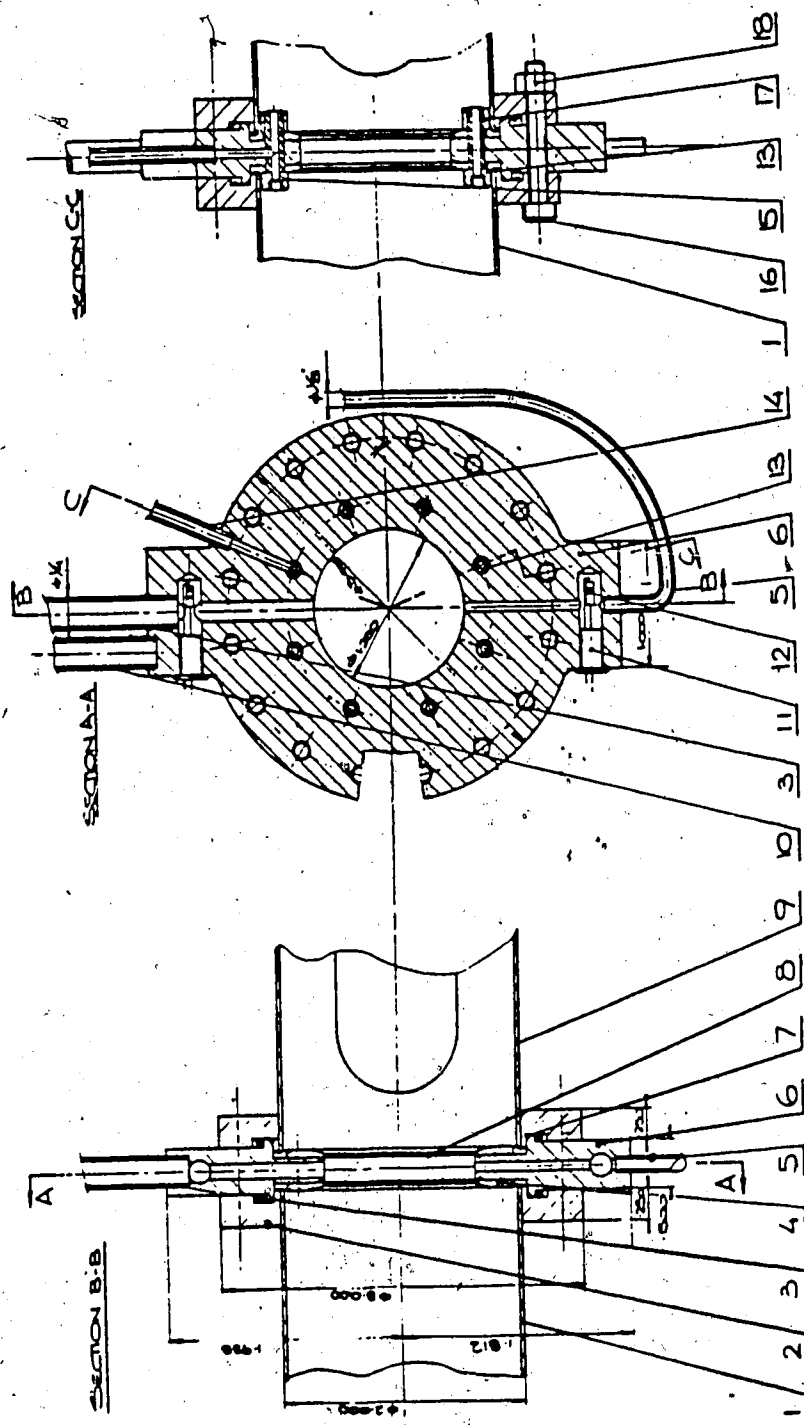


Figure 4.4: Cross sectional views through the liquid H_2 portion of the target. The 'bite' taken out of the cell body helped reduce photon losses. Labels are given on the following page.

ITEM	DESCRIPTION	MATERIAL
1	Upstream Gas Enclosure Half	St.St.
2	Gas Enclosure Flange	St.St.
3	Boil-off Tube	St.St.
4	Reinforcing Ring	St.St.
5	Fill Tube	St.St.
6	Cell Body	St.St.
7	Indium Wire Seal	Indium
8	Cell Window	Kapton
9	Downstream Gas Enclosure Half	St.St.
10	Heat Pipe $\Phi 1/4$ "	St.St.
11	Feed-thru Bushing	
12	Level Sensing Diode	-
13	Breather Bolt	St.St.
14	Gas Inlet/Outlet Tube 1/8"	St.St.
15	Gas Feed-thru Breather Bolt	St.St.
16	Cap Screw	St.St.
17	Nut	St.St.
18	Hex. Nut	St.St.

Table 4.1: Labels for liquid H_2 target items.

allowed the two final state protons to exit the enclosure when they were produced between 10° to 30° on either side of the beam line. A 1.59 mm aluminum sheet added to the HEP window helped prevent δ rays, swept away from the LEP detectors by the permanent magnet, from getting into the HEP detection regime.

To avoid heat being conducted from the rest of the chamber into the liquid hydrogen, the target assembly was supported independently from the cryostat on adjustable thin stainless steel wires and the entire target cylinder was wrapped with a few layers of thin aluminized mylar.

A CRYODYNE 10-20[33] cryogenerator, providing 10W of cooling at 20° K through adiabatic expansion of compressed helium gas, liquified the hydrogen gas. Liquification of the purified hydrogen gas was a two stage process. In the first stage, heat exchanger coils cooled the hydrogen gas before it entered a condensing vessel. In the second stage, the gas condensed around copper pins of a second heat exchanger and the target filled via a vacuum insulated tube connected to the condensing vessel. Similar boil-off tubes provided a path for the vaporized hydrogen from the target to return to the condensing vessel to be re-liquified. The procedure for filling the target consisted of first attaining a reasonable vacuum ($\sim 10^{-4}$ torr), in the scattering chamber and cryostat, opening the filler tube via helium operated valves, and then waiting until the target became cool enough and the cycle of condensation and evaporation slowed enough for the target to fill. Two resistors, one at the top and the other at the bottom of the target cavity, gave an indication of the level of the liquid within the target. The entire

procedure of cool down to liquid H_2 , starting from room temperature, took ~24 hours.

4.1.6 Trigger Detectors

Low Energy Proton Detectors

The detectors for the $pp\gamma$ final state protons detected on the same side of the beam as the photon were located inside the vacuum of the scattering chamber in order to prevent significant energy degradation. Five 6.35 mm thick, type NE102 plastic detectors (good resolution for high count rate applications), at a distance of approximately 1 m from the target, covered the 10° to 30° of polar angle in five 4° steps. Specifically, two forward detectors, $6.24\text{ cm} \times 8.46\text{ cm}$ high were located at 93.45 cm from the target and the other three were $6.98\text{ cm} \times 9.46\text{ cm}$ high, located at 104.33 cm. Each was wrapped with 0.0089 mm aluminum foil, backed with a 0.013 mm polyester, to avoid background arising from the photomultiplier tube response to room lighting. Acrylic adiabatic light guides coupled the 6.35 mm plastics to 5.08 cm diameter Philips P2252 photomultiplier tubes. A small light emitting diode (LED) pulser was attached to the plastics to monitor gain shifts and the dead time of the system.

The elastic veto detectors located outside the scattering chamber at a distance of ~140 cm from the target were 6.35 mm thick, $11\text{ cm} \times 13.15\text{ cm}$ high, type NE102 plastics. Similar couplings were provided to RCA 8575, 5.08 cm diameter photomultiplier tubes. Between the elastic vetos and the

EE trigger counters was 7.0 cm of CH₂ plus 1.27 cm aluminum absorber to stop the pp γ protons.

High Energy Proton Detectors

Eight 3.2 mm thick high energy proton trigger counters, 20 cm \times 15 cm high, of type NE102 plastic, were used. Each had attached a LED pulser. The detectors were coupled through adiabatic light guides to 5.08 cm diameter RCA 8575 tubes. Their distances from the target varied but averaged 3.8 m in the small angle configuration and 3.4 m in the large angle configuration.

Directly behind these trigger counters was copper absorber thick enough to stop pp γ protons, determined by ray-tracing maximum energy pp γ protons through the magnet. Elastic protons, however, had sufficient energy to pass through the copper and were vetoed with wider, 30 cm \times 15 cm high, counters.

A large, random, beam-induced neutral background (observed during a survey of the area with a liquid scintillator) was reduced by two 82 cm \times 15 cm counters in front of, and in coincidence with four trigger counters. A 3.2 mm thick aluminum plate provided support for these detectors.

Photon Detectors

The photons were detected in one of 16 lead glass cerenkov detectors covering the range from 15° to 170°. Eight of these were 12.7 cm diameter, 17.8 cm long cylindrical lead glass detectors (Schott SF5, composition by weight;

51% Pb, 26% O, 18% Si, 3% K, 1.5% Na). These were coupled via RTV 602 silicon cement to 12.7 cm diameter RCA 8854 photomultiplier tubes. The remaining 8 detectors were 15.2 cm \times 15.2 cm cubes, also of SF5, coupled to 12.7 cm diameter RCA 8854 tubes through Dow Corning's SYLGARD compound. Attached to the front face of each detector was a LED pulser. All 16 assemblies were completely surrounded by light protection foil and by 1.59 mm of soft steel which shielded the photo-tubes from the adverse effects of external magnetic fields.

A 3.2 mm thick plastic (NE102) veto scintillator, 15.2 cm \times 15.2 cm, covered the front face of each lead glass to veto charged particles.

4.1.7 Vertical Drift Chambers

Four vertical drift chambers (VDC's) were used for good position resolution at high count rates. Two just outside the scattering chamber in front of a spectrometer magnet, gave the scattering angle of the HE protons and the event vertex position at the target, while two behind the magnet gave, in conjunction with those in front, the bend angle of the proton, i.e. its momentum. Also, a software cut on the x and y planes of the second VDC defined the solid angle acceptance for the HE protons.

VDC's determine, with great accuracy (intrinsic resolution of these chambers is $\sim 150 \mu\text{m}$), the position and direction of a charged particle track within the chamber by measuring the relative drift times of ionization electrons created along the track to three contiguous sensing anode wires. (See figure 4.5.)

Each anode wire within the chamber, spaced 6 mm apart and separated by two field shaping wires (to keep the field between the anode wires uniform and thus reduce non-linearity in the position-drift time relationship), is connected through a discriminator to a Lecroy 4291 Drift Chamber Digitizer (TDC). The relative drift times were determined by defining the TDC start as detection of electrons at the anode wire, and the stop as a suitably delayed photon detection signal from one of the cerenkov detectors.

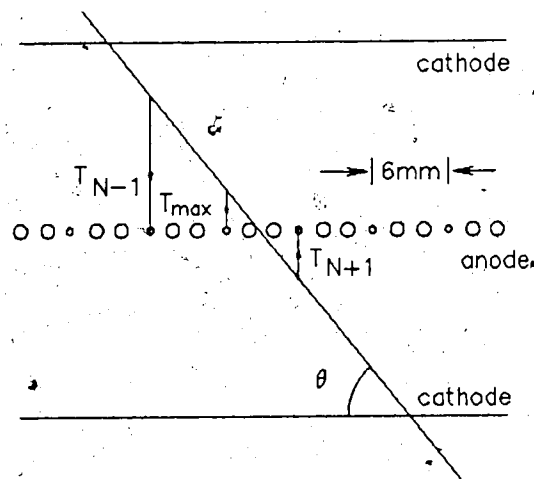
All chambers had 0.025 mm thick mylar entrance and exit windows. Chambers 1, 3 and 4 had one vertical wire anode plane surrounded by two 0.025 mm thick aluminized mylar foil cathode planes. Chamber 2 had, in addition to a vertical wire plane, another anode plane with wires at 30° to the vertical for y-direction information, plus three foil cathode planes.

The active areas of the chambers were: chamber 1, 38.4×9.0 cm high, requiring 64 anode wires; chamber 2, 48.0×10.0 cm, requiring 160 wires (2 planes); chamber 3, 153.6×20.0 cm, requiring 256 wires; chamber 4, the same as chamber 3.

A mixture of 50% argon and 50% isobutane (C_4H_{10}) gas flowed continuously through the chambers. This mixture was chosen for its small diffusion coefficient² and good quenching properties³.

²During drift the electrons will diffuse, following a Gaussian distribution, due to multiple collisions.

³Avalanching is reduced with a polyatomic molecule (C_4H_{10}) which has many non-ionizing energy dissipation modes.



Definitions: N = channel # with largest time value
 T_{\max} = largest TDC value (= shortest drift)
 T_{\min} = lesser of T_{N+1} and T_{N-1}

Quantities of interest:

$\tan(\theta) \propto T_{\max} - T_{\min}$ angle of particle track (arbitrary units)

$\bar{T} = T_{\max} + 1/2 |T_{N+1} - T_{N-1}|$ mean time of passage

$X = N - 1/2(T_{N+1} - T_{N-1}) / (T_{\min} - T_{\max})$ position of track

Figure 4.5: Operation of vertical drift chambers.

4.1.8 C-Magnet

The momentum analysing C-magnet for the high energy protons was designed specifically for this experiment. A schematic diagram is given in figure 4.6. The gap size was 10 cm and the pole area was $40.0 \times 86.8 \text{ cm}^2$. Two coils, saddle shaped to reduce their width so the VDC's could be positioned close to the pole edges, were used.

An operating field between 0 and 1.76 T could be obtained by varying the current from 0 to 750 amps through 132 turns/coil of 7.9 mm^2 copper conductor. Maximum power consumption at 750 A was 31.5 KW/coil. For the duration of the experiment the field was held constant at 1.0 T, requiring 330 A.

Prior to the experiment, field maps were taken at 0.8 and 1.5 T using a Hall probe, 2.54 cm below, 2.54 cm above, and at the central plane of the gap. During the experiment the field strength was continuously monitored with an NMR probe centred within the gap.

The proximity of the C-magnet to the beam line gave a remnant field of ~ 200 gauss in the region of the beam. A beam re-steering magnet positioned slightly downstream of the C-magnet was therefore required.

4.1.9 Electronics

The electronic logic leading to an event definition and subsequent information handling is shown in figure 4.7. All components relating to event definition

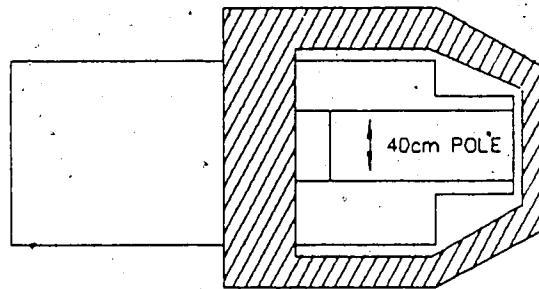
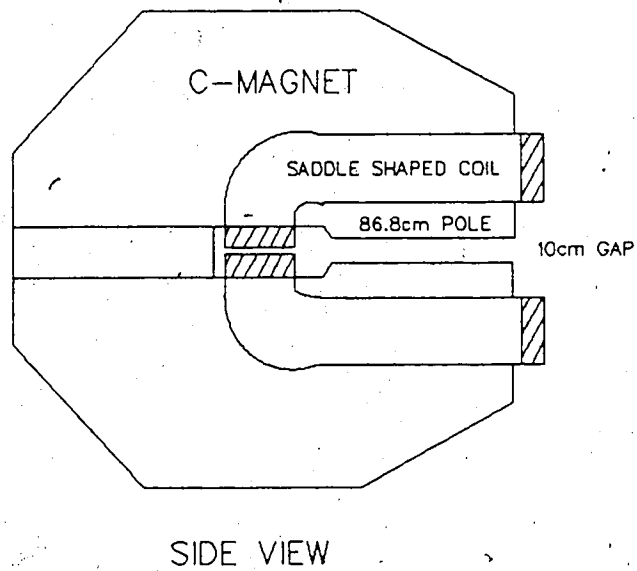


Figure 4.6: Two views of the high energy proton momentum analysing C-magnet.

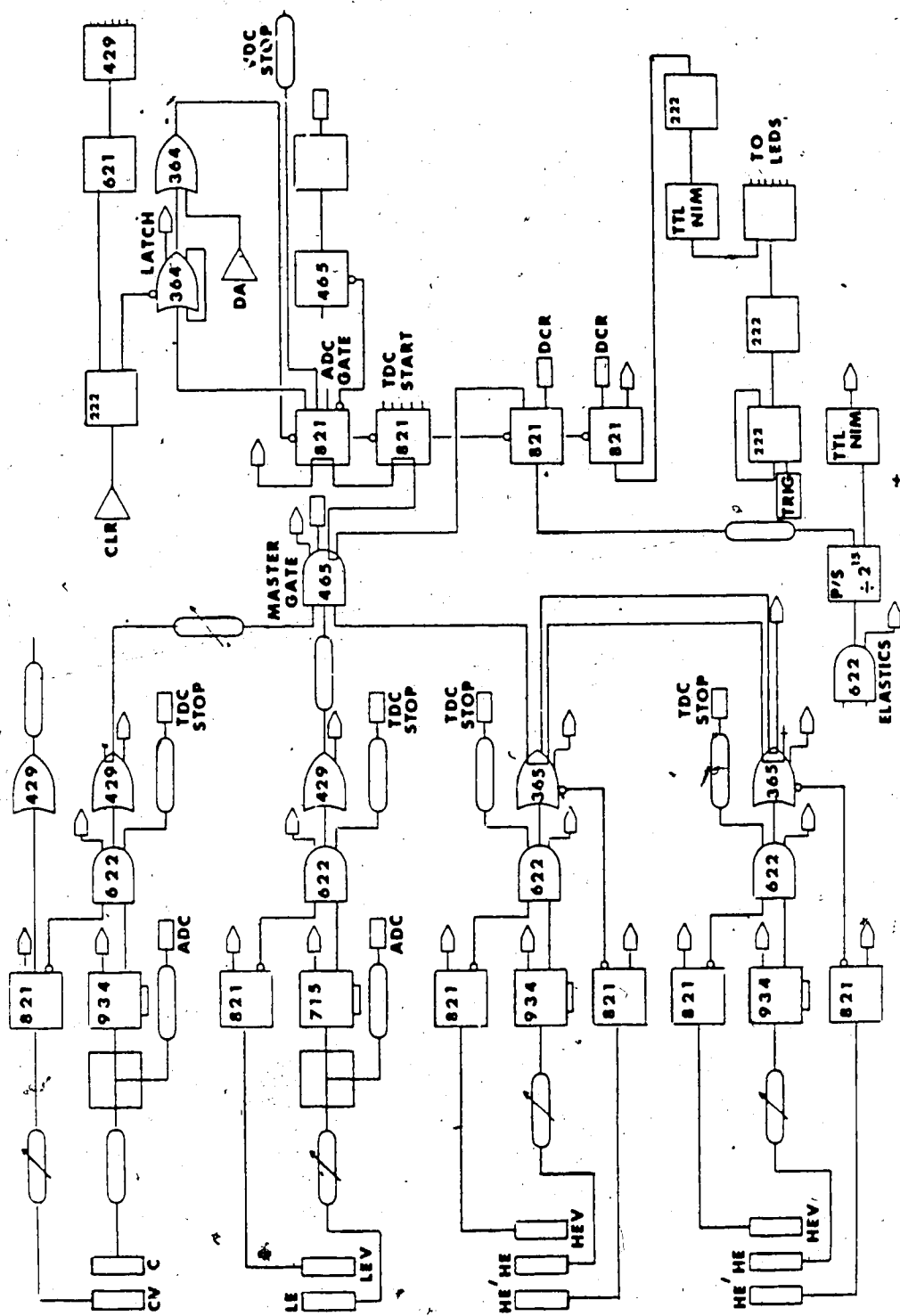


Figure 4.7: Electronic logic for handling 3-coincidence events.

were located within the experimental area.

A $pp\gamma$ candidate required a triple coincidence at the Master Gate (a Lecroy 465 quad coincidence unit). This in turn required the particular conditions to be satisfied by the different detector types. For all detectors, the amplitude of the signals from the outputs of the photomultiplier tubes had to be above the discriminator threshold. (Section 4.2 gives details of threshold values.) For the LE protons, an anticoincidence was required between one of the 5 particle detectors inside the evacuated scattering chamber and its elastic veto situated behind the CH_2 absorber. A splitter sent half of the particle detector signal into a charge integrating Lecroy 2249 ADC and the other half into a Philips 715, 5 channel timing discriminator. The output of this discriminator, along with the NOT output of a Lecroy 821 quad discriminator connected to the LE veto, was fed into an LRS 622 coincidence unit that determined the anticoincidence. Five such coincidence units supplied the inputs to a Lecroy 429 OR-gate, the output of which went into the master gate and provided stop signals for the TDC's.

For the HE protons a similar arrangement existed, however, the HE detector signals were fed through a Ortec 934 constant fraction discriminator (CFD). No ADC's were connected since energy information was obtained from the spectrometer. Two tagging counters, each covering 4 HE detectors, were effectively put in coincidence with the 8 HE detectors by having their NOT outputs veto an output from the two LRS 365 OR-gates.

An anticoincidence between one of the cerenkov counters and its veto was formed in a similar fashion as that for the LE detectors, except that the

cerenkov signal was fed through a Ortec 934 constant fraction discriminator.

Outputs of all discriminators, coincidence units, and OR-gates were attached to Kinetics 3615 Hex or Lecroy 32 channel scalers.

If pulses from the 3 detector types overlapped at the master-gate (see Sec. 4.2 for timing and pulse width information), a triple coincidence was defined and the output of this coincidence unit started the TDC's, opened the ADC gates, set a digital coincidence register (DCR) bit (indicating a triple coincidence), stopped all VDC TDC's, and set a latch. The latch, a combination of two LRS 364 OR-gates, with one feeding itself, prevented another event from overwriting the DCR, ADC's, and the TDC's before the computer had finished reading the previous event. It could also be set/reset through the computer key board to suspend/continue event acquisition.

Aside from an event defined by having pulses from the 3 detector types overlap at the master-gate, HE elastic pre-scaled events and pulser events were allowed. An HE elastic event required a coincidence, through a LRS 622 AND-gate, between HE detector number 4 (fourth from the beam line in the detector array), and its elastic veto. The output of the coincidence unit was fed through a custom made pre-scaler, set to accept one event out of every 2^{15} events. No detector TDC information was obtained for these events since no detector TDC stops were provided. Figure 4.8 shows the electronic logic for these elastic events. Pulser events, triggered off the polarimeter to scale with the real 3-coincidence rates (for an accurate determination of dead time) were obtained from light emitting diodes in each of the detector types, supplied by a fanout box connected to the pulser trigger. Figure 4.9 shows

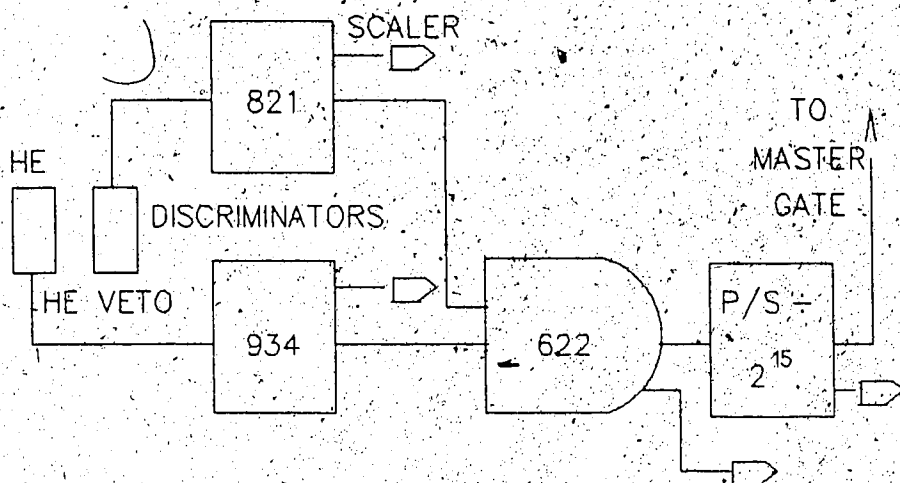


Figure 4.8: Electronic logic for the HE pre-scaled elastic events.

the electronic logic for these pulser events. To allow easy identification of the event type, separate DCR bits were set for the 3-coincidence, HE pre-scaled elastic, and pulser events.

Scalers were attached to the master-gate, the HE p/s elastic coincidence unit, the pre-scaler, the pulser trigger, and the latch.

4.1.10 Computer

Acquisition was carried out on a Data General Eclipse S230 computer with an RDOS operating system and having 384 K bytes of physical memory. This was backed up with a 5 Mbyte fixed disk, a 5 Mbyte removable disk, and a 1600 bpi magnetic tape drive. The electronics were linked via a CAMAC branch to the computer located in the counting room ~10 m. away.

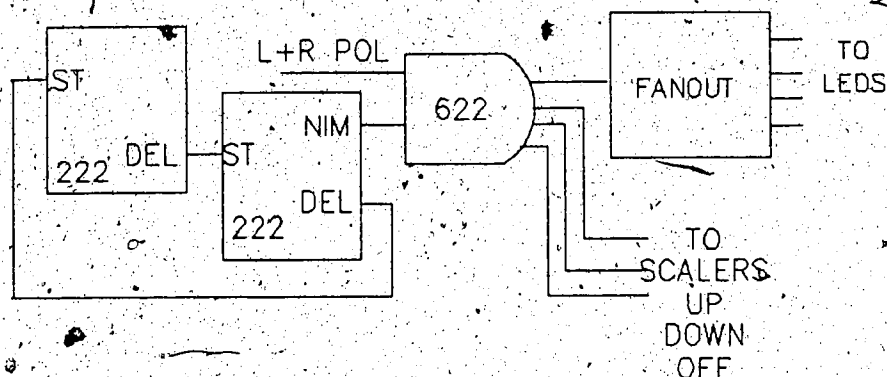


Figure 4.9: Electronic logic for the pulser events.

4.2 Detector Calibration

4.2.1 LEP Detectors

The production energy range of interest for these protons was ~ 10 to 120 MeV. This meant that the energy deposited by the lowest energy proton in the 6.35 mm plastic scintillator, considering energy loss in traversing the liquid H_2 target, was about 5 MeV. The energy deposited by the highest energy 'passing' proton was about 3 MeV. Gains of the photo tubes were set with a $100\text{-}\mu\text{Ci } ^{22}\text{Na}$ gamma source by choosing the 340 keV Compton edge of one of the 511-keV annihilation photons to give a 40 mV output from the tube, as measured after all delays and splitters (i.e. at the discriminators). Within this region the ADC's are more or less linear. Discriminator thresholds were then set to 30 mV to accept this lowest energy proton.

Pulser amplitudes were adjusted to give a response near the top of the ADC spectra.

For the LE veto detectors, gains were adjusted so the 340 keV Compton electron absorbed in the 6.35 mm plastic veto detector gave a 20 mV amplitude at the discriminators. The minimum energy deposited by passing elastic protons of maximum energy 270 MeV is 2.4 MeV. (Energy loss is actually slightly greater because of the degradation of the proton energy in going through the CH_2 absorber.) Thresholds were set to 30 mV.

4.2.2 HEP Detectors

The energy range of the pp γ protons into the HEP detectors was 50 to 220 MeV. The minimum energy deposited by the maximum energy proton in the 3.18 mm plastic was determined to be 1.2 MeV. Gains were adjusted so the 340 keV Compton electron gave 20 mV at the discriminator. Discriminator thresholds were set to 30 mV.

HE veto detector gains were set so the 340 keV Compton electrons gave a 34 mV amplitude at the discriminators. Thresholds were also set to 30 mV. (The thickness of these counters was also 3.18 mm, and the maximum energy elastic proton was 270 MeV.)

4.2.3 Cerenkov Detectors

Minimum ionizing cosmic rays, namely muons, were utilized for calibration. It had been determined, through calibration of some detectors in a 70 MeV

electron beam, that these muons produce the same amount of light as a 100 MeV gamma in the cylindrical 12.7 cm \times 17.8 cm Pb glass, and a 120 MeV gamma in the 15.2 cm \times 15.2 cm cubes.

Gains of the phototubes were adjusted such that the broad cosmic peak minus the pedestal (artificial bias applied to the ADC's to keep values positive), lay somewhere between 1/3 and 1/2 of the available ADC range and corresponded to roughly 3 channels/MeV. Events were acquired simultaneously for all 16 counters with the computer by defining the master-gate as a coincidence between a cerenkov and its veto, with discriminator thresholds turned down for acquisition. Various tests were first performed by placing the veto counter on the top, sides, and the front face of the detector to see if the peak was affected by the orientation of the counters. Although the shape of the peak was found to change, the peak positions of all spectra were within 5% of each other.

pp γ photons had energies ranging from \sim 190 MeV at forward angles to \sim 50 MeV at backward angles. Thresholds were set at roughly 20 MeV (corresponding to between 150 and 200 mV), by assuming the range between the pedestal and cosmic peak on the ADC spectrum was linear.

4.2.4 Vertical Drift Chambers

The high flux of elastically scattered protons on the VDC's demanded operation at relatively low gain ($\simeq 10^4$). Operating anode plane voltages, giving the best efficiencies without drawing too large a current, were determined by

trial and error to be 7.5, 7.8, 7.8, 8.2, 8.2 KV for chambers 1, 2(2 planes), 3, and 4 respectively. The efficiencies were obtained by first setting the trigger to define an event as a coincidence between any HE detector and its veto. The ratio of the number of events that missed in a chamber but did not miss in its neighbor chamber, divided by the total number of events after subtracting out those that missed in both chambers (thought to be bad triggers), was the efficiency.

4.3 Detector Timing

4.3.1 LEP and HEP Detectors

Relative timing of all detectors and vetos was obtained by using a double gamma coincidence, from positron annihilation in a ^{22}Na source, with a 6.35 cm thick plastic "wand" detector and each particle detector in turn. Adjustable delays were used to set the time differences consistently over the detector groups. Relative time differences between the HE and LE detectors was set to about 45 ns at the master gate to cover the flight time differences and to allow a coincidence between a LE proton and a HE proton delayed by one beam burst. (Widths of the LE, HE, and γ pulses at the master gate were set to 120, 120, and 10 ns respectively, (therefore photon detection determined the event timing). Timing errors were estimated to be ± 2 ns.

4.3.2 Cerenkov Counters

Cerenkov vetos were timed with the "wand" using the ^{22}Na source. The Pb glass was timed relative to the "wand" using a 4.4 MeV photon from a series of decays initiated by α decay of Am in a Am-Be source. (The photon compton scatters in the plastic and pair creates in the Pb glass.) Also, the relative timing of the vetos and counters was checked with cosmic rays.

Chapter 5

Event Acquisition and Analysis

5.1 Acquisition

Data was taken in two approximately 500 hour runs in January and June of 1985. In January, in the large angle configuration (LAC), approximately 80,000 $pp\gamma$ events were obtained. In June, in the small angle configuration (SAC), another approximately 60,000 were collected. In total 200 data tapes were written at 1600 bpi density, each containing about 120,000 events, of which less than 0.6% were $pp\gamma$.

Events were acquired on-line with the software program MIDAS[34] via a Data General Eclipse S230 computer. The event data word structure is listed in tables 5.1 and 5.2. The sections are:

1. Digital Coincidence Registrar (DCR) - see table 5.3 for the assignments of the individual bits.
2. Cerenkov TDC values - photon detection time (delayed stop) with re-

WORD #	DESCRIPTION	WORD #	DESCRIPTION
1	DCR HIGH	22	CERENKOV ADC 1
2	DCR LOW	23	ADC 2
4	CERENKOV TDC 1	24	ADC 3
5	TDC 2	25	ADC 4
6	TDC 3	26	ADC 5
7	TDC 4	27	ADC 6
8	TDC 5	28	ADC 7
9	TDC 6	29	ADC 8
10	TDC 7	30	ADC 9
11	TDC 8	31	ADC 10
13	TDC 9	32	ADC 11
14	TDC 10	33	ADC 12
15	TDC 11	35	ADC 13
16	TDC 12	36	ADC 14
17	TDC 13	37	ADC 15
18	TDC 14	38	ADC 16
19	TDC 15	40	LE-1 TDC
20	TDC 16	41	LE-2 TDC

Table 5.1: Event data word structure. (Part 1.)

WORD #	DESCRIPTION
42	LE-3 TDC
43	LE-4 TDC
44	LE-5 TDC
47	R.F.
49	HE-1 TDC
50	HE-2 TDC
51	HE-3 TDC
52	HE-4 TDC
53	HE-5 TDC
54	HE-6 TDC
55	HE-7 TDC
56	HE-8 TDC
58	LE-1 ADC
59	LE-2 ADC
60	LE-3 ADC
61	LE-4 ADC
62	LE-5 ADC
64	VDC WORD COUNT
65→	VDC TDC RAW DATA

Table 5.2: Event data word structure. (Part 2.)

spect to a common start.

3. Cerenkov ADC values - a measure of the energy deposited within the Pb glass detectors.
4. LEP TDC values - LEP detection time with respect to photon detection time.
5. R.F. - cyclotron R.F. time signal.
6. HEP TDC values - HEP detection time with respect to photon detection time.
7. LE ADC values - a measure of the energy deposited within the plastic LEP detectors.
8. VDC WORD COUNT - a variable equal to the number of VDC TDC values to follow. This number depended on the total number of struck VDC anode wires.
9. VDC TDC values - detection time of ionized electrons with respect to photon detection time. One word for each struck wire.

At LAM requests from the Camac modules, the computer read the data words and a short acquisition program then decided which events were pp γ candidates and would be kept for further processing. After a 1024 word buffer was filled, the data was transferred to permanent storage on magnetic tape. The on-line analysis was short so computer dead time would be minimized.

WORD #	BIT #	DESCRIPTION
1	0-15	NOT USED
2	0	PULSER
	1	TRIPLE COINCIDENCE
	2	SPIN UP
	3	SPIN OFF
	4	SPIN DOWN
	5	SPIN BUSY
	6	HE PRESCALED ELASTIC
	11	(SOFTWARE) 3% PRESCALED TRIPLE

Table 5.3: DCR bit assignments.

Three percent of the triple coincidence events that triggered the electronics were put directly to tape without any processing. These un-processed events were used as a check on cuts applied during acquisition and later analysis, and also for a missings and multiples correction applied to the cross section. On-line rejected events were only those with missing drift chamber planes (less than three struck wires per plane).

Monitoring the operating condition of the system was essential for good data taking. On-line, those aspects which were most crucial were monitored. This entailed looking at scalers, scaler rates, and a spectrum of the position of the event vertex within the target to survey for failed electronic components, a bad beam tune or alignment, and target failure.

A more complete analysis was performed almost simultaneously on a Data

General Eclipse S200 computer since computer dead time was no longer a factor. The objectives were to closely survey hardware operation and identify $pp\gamma$ events. Monitored were detector gains (by noting the position of the pulser in ADC spectra for the LE and Cerenkov detectors), magnet and drift chamber operations (by viewing plots of the bend angle of the HE protons in passing through the spectrometer, and spectra of track position within each VDC plane). $pp\gamma$ events were identified by looking for kinematic loci on the following spectra: HEP time of flight vs LEP time of flight; HEP bend angle vs LEP time of flight; deposited energy in the LEP detectors vs LEP time of flight. Figures 5.1 to 5.3 are reproductions of what were observed during semi-on-line analysis.

5.2 Analysis-Skimming

Of the data on the 200 tapes, only a very small fraction was from $pp\gamma$ events. The first part of the analysis was concerned with reducing this number of tapes to a more manageable number by selectively discarding events that did not satisfy very generous limits on various kinematic quantities. The HE prescaled elastic events, pulser events, and the 3% sample were spared from this kinematic "skimming" process. The steps of this procedure were executed in the order enumerated below with the software program MIDAS on an Eclipse S200 computer.

1. The 3% sample, identified by having bit 11 of DCR word 2 set, were saved and copied directly to tape.

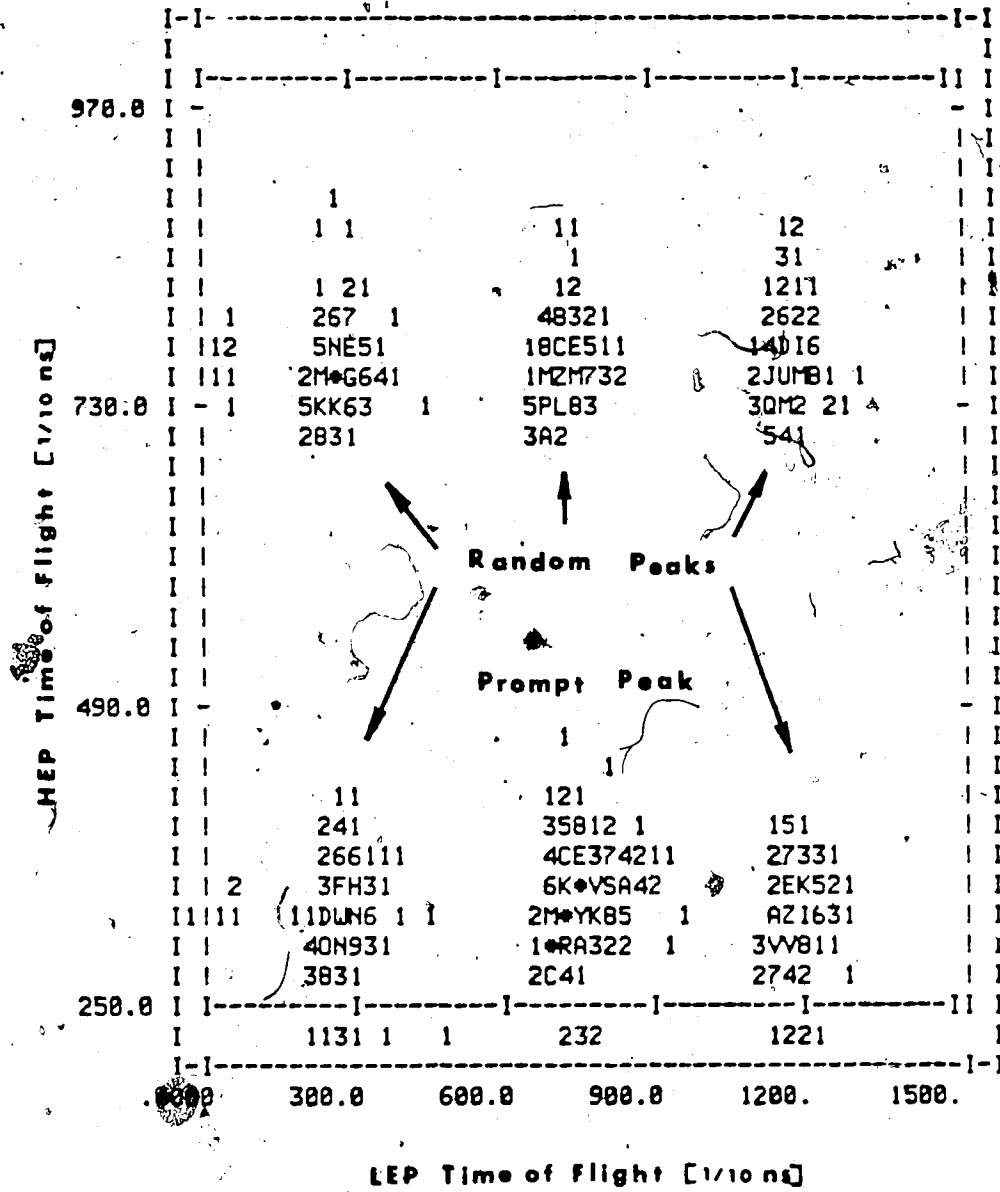


Figure 5.1: LEP time of flight versus HEP time of flight. The prompt central peak contains the real ppy events.

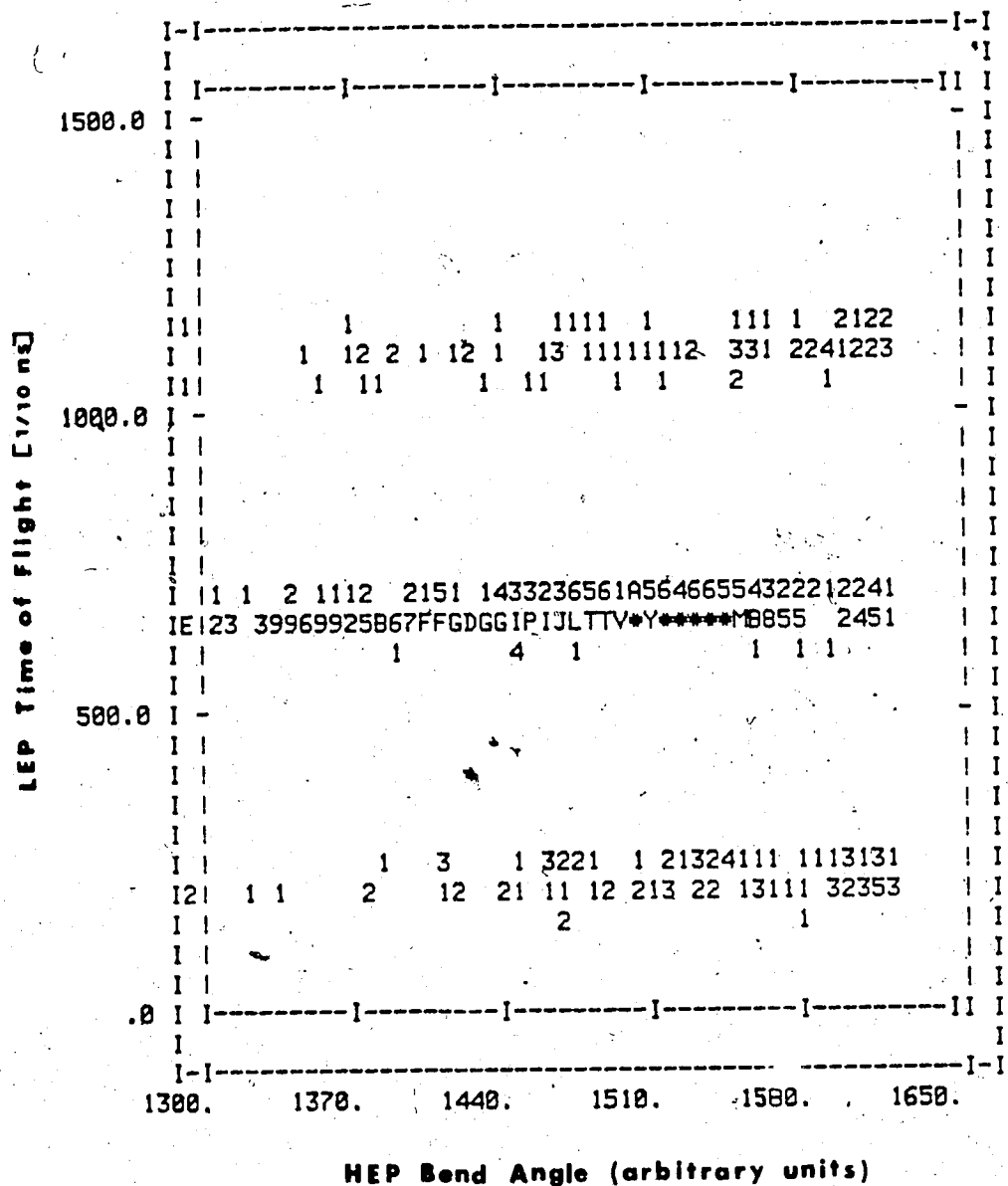


Figure 5.2: HEP bend angle through the spectrometer versus LEP time of flight.

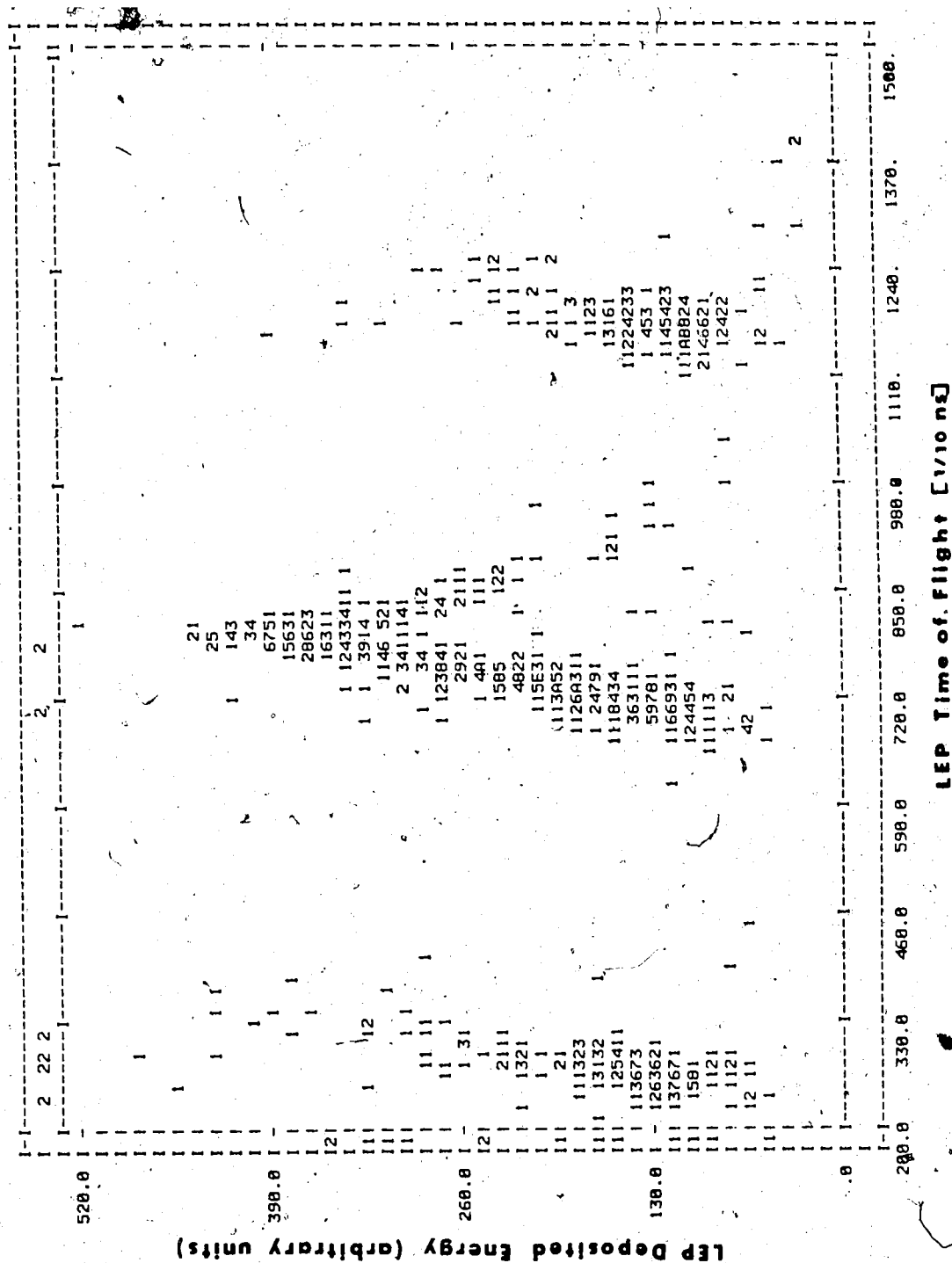


Figure 5.3: LEP time of flight versus LEP deposited energy. The central peak contains the real $pp\gamma$ events

2. 1/10 of all pulser events, gated by spin (up, down, off, busy), were copied directly. A uniform sample over the entire run was taken.
3. An event was rejected if only one Cerenkov counter fired (i.e. it was not a photon multiple), and its Cerenkov-RF time was not within ± 6 ns of the spectrum peak attributed to prompt events associated with a beam burst. Because of poor timing resolution, due in part to statistics, Cerenkovs 2, 15 and 16 had cut widths of ± 9 , ± 9 , and ± 12.5 ns respectively. Figure 5.4 is a spectrum of Cerenkov-RF time summed over all 16 counters. The figure shows the microstructure of the beam, i.e. the 5 ns beam burst separated by 43 ns. The peaks are broadened by adding the 16 counters together and by beam induced background.
4. Corrections were made to the HE proton TDC values for electronic delays and flight path distances.
5. An event was labeled a drift chamber "miss" if;
 - (a) the number of wires hit in any one VDC plane was less than three,
 - (b) no valid vertex (see section 4.1.7) was found because either,
 - i. the hit wires had a bad time structure, i.e. no discernible peak,
 - ii. the VDC track detection time was not within a very generous limit (± 300 ns) of the HEP scintillator telescope detection time. For multiple hits in the HE scintillators this limit was increased to 500 ns.

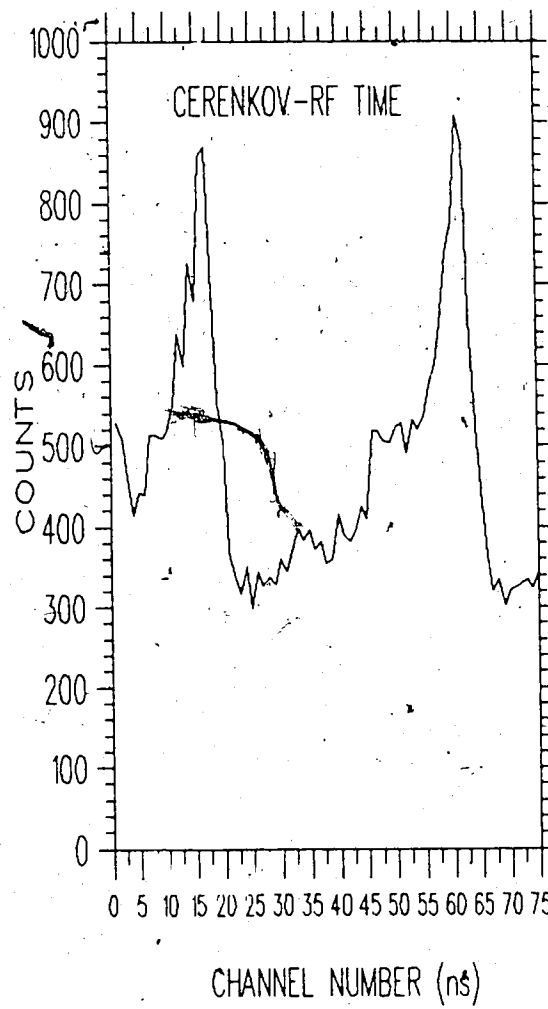


Figure 5.4: Cerenkov-RF time spectrum summed over all 16 Cerenkov detectors.

6. An event was labeled a drift chamber "multiple" if,

(a) the number of wires hit in any one VDC plane was greater than

20,

(b) more than one valid vertex was found.

7. Missing events were rejected unless only VDC plane 2U (used for y or vertical position information) was missing or if a plane was missing because the event was at a dead wire. (During the runs two wires stopped giving information but could not be fixed without a major disruption.) If the missing plane had at least one hit within ± 1 wire of a dead wire then these events were saved and later recovered in the final analysis.

For rejected missing events, a three dimensional array was incremented with indices corresponding to, the event type (3-coincidence or HE prescaled elastic), the spin condition (up, down, off, busy), and the VDC plane or planes missing.

8. A generous cut on the bend angle to eliminate elastics was made for those events which were not missing or only 2U missing, not multiple, and not HE P/S events. Figure 5.6 shows the HEP angle of bend acquired through the spectrometer vs photon scattering angle for a number of proton opening angles. $pp\gamma$ events are clearly separated from the higher energy random elastics background.

9. After applying to the HEP and LEP TDC values, corrections for electronic delays, flight path differences, and kinematics, and aligning ran-

dom peaks by adding or subtracting 43 ns, a generous cut of ± 6 ns was applied to the center of the observed peak attributed to $pp\gamma$ events, on the condition that no multiple hits were detected in any of the counters and the event was not an HE P/S or pulser.

The effect of these cuts was to reduce the amount of random data by a factor of 5, leaving about 40 "condensed" tapes for further processing.

5.3 Analysis - Processing

Analysis of the 40 skimmed tapes was performed on Digital VAX 780 and VAX 8600 computers with the software program Perseus.

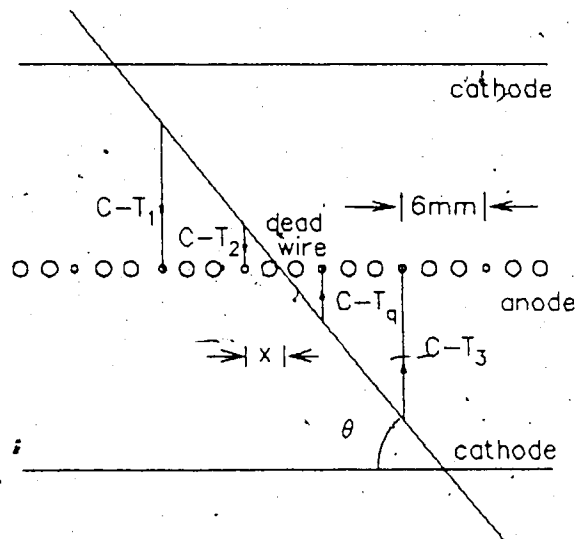
For each 3-coincidence event, the following tasks were performed. First, all 5 LE TDC values were checked to determine which LE detector was hit and whether the event was real i.e. prompt, or random (TDC value delayed or advanced by 43 ns). If more than one detector was hit the event was flagged as an LE multiple. A similar loop was made over the 8 HE TDC values, only here the random events were advanced by 43 ns over the prompt events. Figure 5.1 shows the time structure of the real and random events on a plot of LE TDC vs HE TDC. A third loop was made over the 16 Cerenkov detector TDC values. If more than one Cerenkov detector had a valid TDC, the event was flagged as a Cerenkov multiple. If there were no multiple hits for each detector type, a separate flag was set for real and random events. For random events only one in every 5 was chosen to set the flag since there

Detector	% Multiple
LE	4.2
HE	2.0
Cerenkov	1.9

Table 5.4: Detector multiples statistics.

were 5 possible random LE vs HE timing peaks (see figure 5.1). Table 5.4 is a compilation of the multiple detector hits statistics averaged over all detectors. Section 6.6 contains a more detailed listing of multiples by detector number and a description of how a correction factor for these was incorporated into the cross sections via a Monte Carlo simulation.

A VDC decoding routine was called to determine for each plane, from the raw TDC values of the struck wires, the position of an HE particle track, its angle with respect to the VDC plane, and the relative time of passage of the particle through the plane with respect to the photon detection time. Knowledge of the relative drift times of the ionization electrons along the particle path to the nearest anode wire for three contiguous wires, allows determination of all the above quantities, see figure 4.5. [For events that didn't have three contiguous wires hit because of an intervening dead VDC wire, a check was made if there were any hits within ± 1 of the dead wire. The algorithm described in figure 5.5 was then used to determine a position, angle, and mean time of passage of the track through the VDC for these cases.]



Definitions: C = unknown constant time
 T_1, T_2 , and T_3 = TDC values for wires
 T_q = unknown TDC value for dead wire
 X = distance to be determined

Unknowns: C, T_q , and X

Relations: $(C - T_3) - (C - T_q) = (C - T_2) + (C - T_q)$

By equivalent angles,

$$(C - T_1) - (C - T_2) = (C - T_3) - (C - T_q) \quad \text{and,}$$

$$((C - T_1) - (C - T_2)) / 6\text{mm} = (C - T_2) / X$$

Solution: $X = 6\text{mm}(0.5(T_3 + T_2) - T_1) / (T_2 - T_1)$

Figure 5.5: Algorithm to determine VDC quantities for the case of an event at the site of a dead wire.

For each VDC anode plane, the number of misses and multiples was determined as follows. An event was labeled a miss if any one of the following were true:

1. There were less than three contiguous wires hit, (excluding those events at a dead wire).
2. No vertex found (i.e. no wire with a minimum drift time surrounded by ones with larger times).
3. The relative VDC-HE detection time was not within 100 ns if one HE detector was hit, and 500 ns if more than one detector was hit.
4. The internal track angle was not within the generous limits determined by plotting the internal angle of good ppy events for each VDC anode plane.

An event was labeled a single multiple (SM) or a double multiple (DM) if;

1. two valid vertices ('valid' in the sense that none of the above 'missings' tests were true for the track) were found (SM),
2. the number of wires hit was greater than 30 (DM),
3. more than two valid vertices were found (DM).

Drift chamber single multiples were reduced first by comparison of internally calculated angles of the track on neighbor planes, i.e. 1 and 2, or 3 and 4. Both neighbor planes could be a single multiple but neither could be

Analysis	Tests	% Multiple
on-line	less than 5 wires struck in any one VDC	88.20
off-line	vertex required, VDC-HE time cut,	
	internal angle within limits	13.86
angle	correlation required between internal	
comparison	angles on planes 1 and 2, and, 3 and 4 (neighbor planes could both be multiple but neither could be a double multiple or a missing)	4.93
magnet axis	projection of tracks before and	
projection	after magnet to center of magnet (requires either planes 1 and 2, or 3 and 4, to have a single good track after application of off-line and angle comp- arison tests)	4.45

Table 5.5: Results of the VDC multiples reduction scheme.

a double multiple or a missing. Secondly, single multiples were reduced by projecting tracks before and after the magnet back to the magnet axis and selecting the set which was better matched. This required either planes 1 and 2 or planes 3 and 4 to have a single good track. Table 5.5 shows the results of this multiple reduction scheme for a run taken at approximately 12nA.

Those events with a single hit in each detector were then binned according

to LE detector hit, Cerenkov counter hit, and HE scattering angle (the full 10° to 30° coverage was divided into six 3.3° bins), giving 480 bins in all. After enough statistics had collected in each bin, spectra were plotted and limits of various kinematic quantities determined for each bin. These quantities were:

1. bend angle of the HE proton in traversing the C-magnet,
2. deposited energy in the LE plastic proton detectors,
3. time of flight after corrections for kinematics, delays and flight path length differences, for the HE protons,
4. time of flight for the LE protons after similar corrections.

Values of these limits were used as cuts for selecting good $pp\gamma$ events over the large random background. Figures 5.6 and 5.7 show plots of kinematic quantities 1. and 2. for which limits were determined.

Finally the following tests were applied to each event before a number of two dimensional arrays, with indices Cerenkov hit and LE hit, were incremented. (These arrays corresponded to: different spin state, up, down, or off; HE bin, by dividing VDC2 coverage into four, approximately 5° horizontal by 4° vertical sections, and a real or random event.) Tests were that the event was:

1. a triple coincidence,
2. not a pulser,

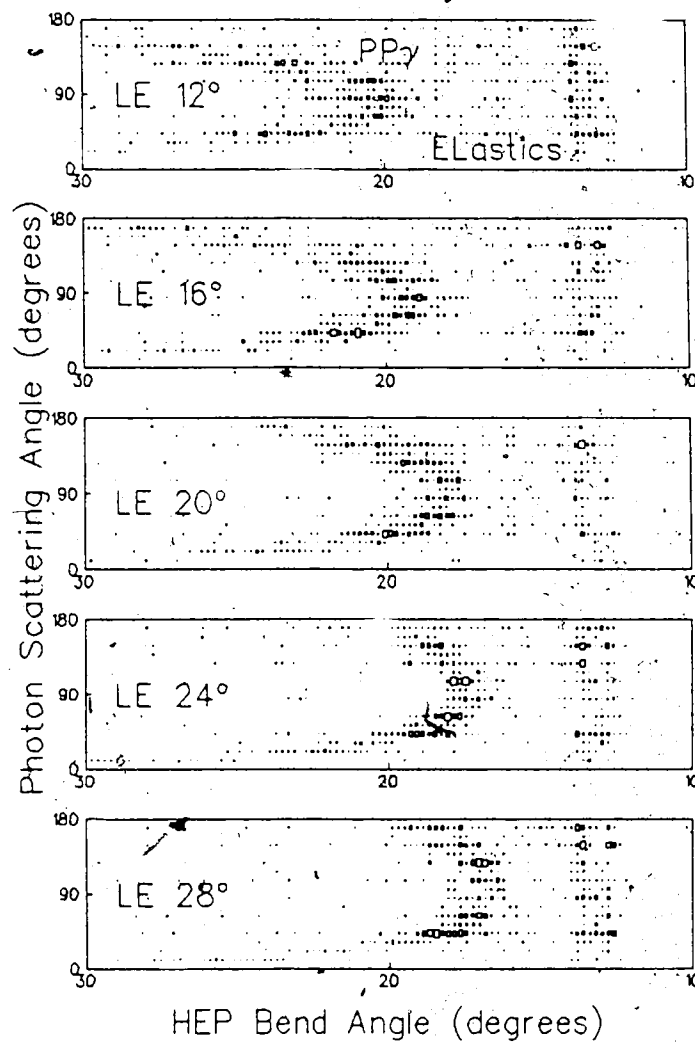


Figure 5.6: HEP angle of bend through spectrometer versus photon scattering angle, HEP bin centered at 17.5°.

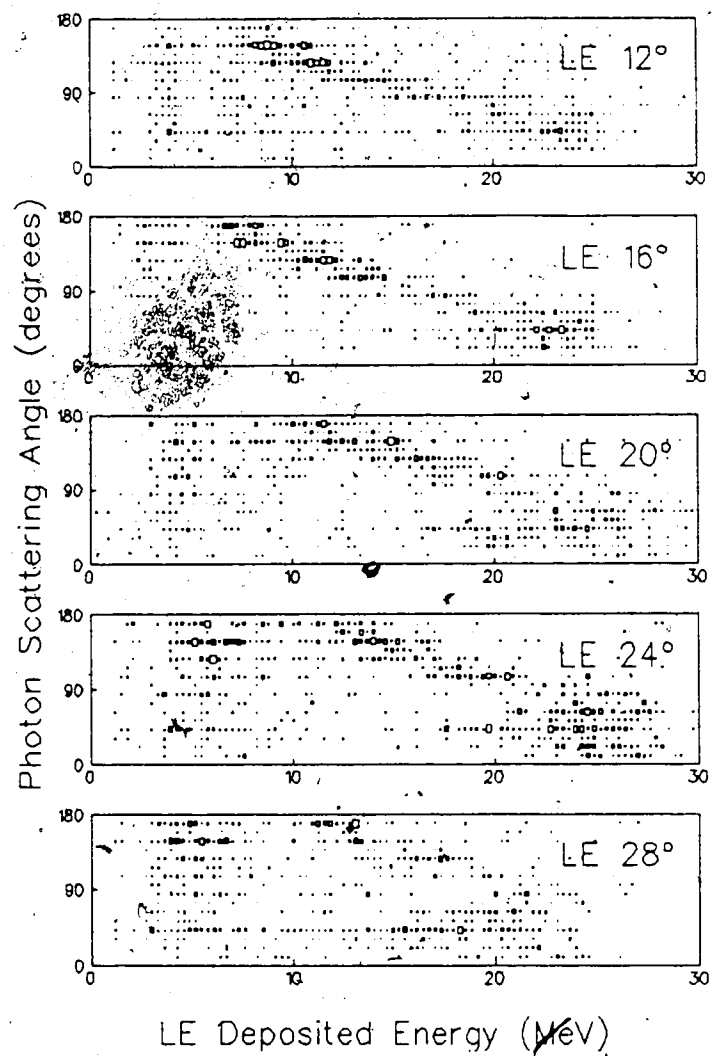


Figure 5.7: LEP deposited energy versus photon scattering angle.

3. not an HE P/S elastic,
4. a single hit in each counter type,
5. not a VDC missing, (or only plane 2U missing for the asymmetry determination),
6. not a VDC multiple (or only plane 2U multiple),
7. came from the liquid portion of the target (determined by a cut on HE vertex projection back to the target, along an axis parallel to drift chambers 1 and 2, see figure 5.8,
8. passed the HE bend angle cut,
9. passed the LE ADC cut,
10. passed the LE TDC cut,
11. passed the HE TDC cut.

Scaler events were read at the beginning and end of each run. If none of the spin gated SEM counts were zero after the first scaler read, it meant that the scalers were not zeroed at the start of the run. (Scalers were read every 5 s and the spin cycled through, 3 min spin up, 3 min spin down, and 1 min spin off.) In these cases the first scaler read ~~set~~ was subtracted from the scaler read at the end of the run. Tables 5.6 to 5.11 show the accumulated scaler and ppy event counts in the LAC and SAC respectively.

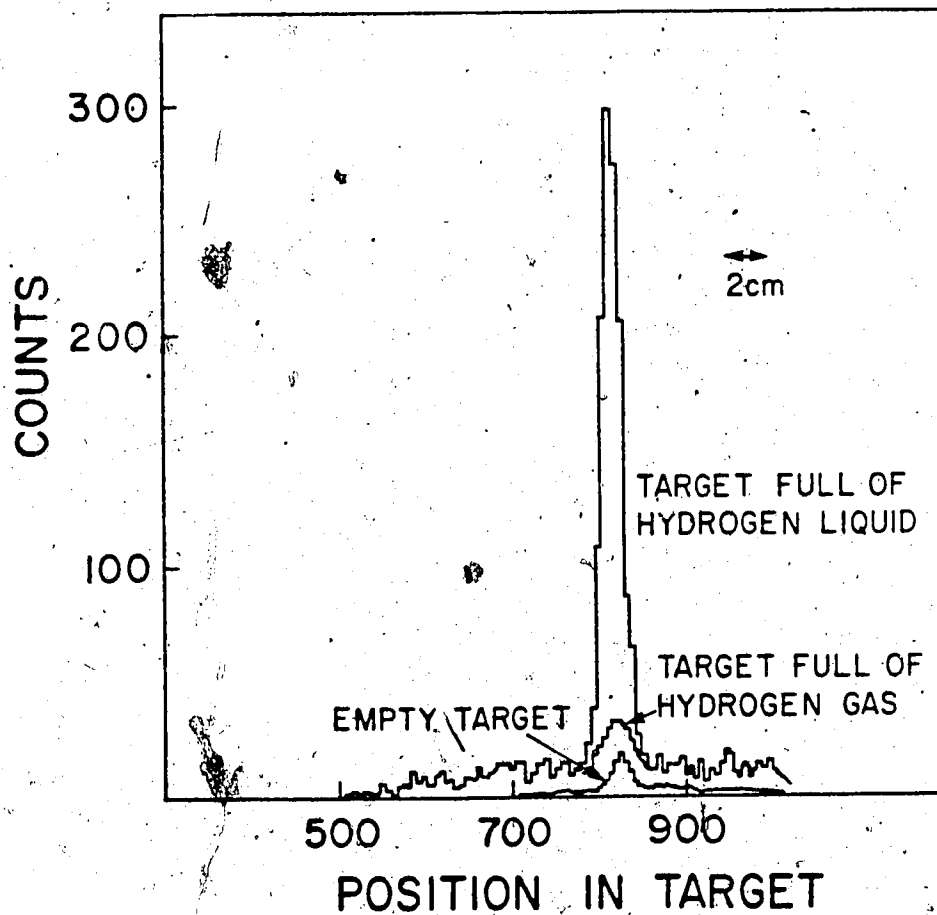


Figure 5.8: Projection of the HE proton tracks in drift chambers 1 and 2 back to the target.

LAC Scalers					
Pulser (up,dn,off)	SEM	Pol. Left	Pol. Right	Pol. Left Accidental	Pol. Right Accidental
19298573.	287591.	659981884.	385763149.	75863378.	64446566.
18987316.	280205.	373999274.	650499001.	52458118.	92827969.
7865050.	126405.	221624944.	224273872.	32178280.	40966584.
3-coinc.	HE P/S	HE4-V4	latch	pulser	60HZ
25833785.	622155.	20259749785.	19803922.	587295.	47174031.

Table 5.6: Accumulated scaler counts in the LAC.

SAC Scalers					
Pulser (up,dn,off)	SEM	Pol. Left	Pol. Right	Pol. Left Accidental	Pol. Right Accidental
28879447.	279982.	866030670.	477996603.	25712268.	28171065.
30100211.	289733.	513190433.	878362704.	14757892.	2361119.
8739531.	83801.	203392305.	197581328.	5626015.	47947.
3-coinc.	HE P/S	HE4-V4	latch	pulser	60HZ
44764949.	779402.	25603636075.	31188639.	536875.	65805534.

Table 5.7: Accumulated scaler counts in the SAC

LAC ppy Counts																
Small HE Angles (18.0° to 24.5°)																
Spin Up																
LE Angle	15	30	40	50	60	70	80	90	100	110	120	130	140	150	160	170
12	0	87	116	345	127	319	116	294	94	293	296	267	74	141	25	9
20	36	144	156	432	159	313	74	236	82	247	257	197	63	179	59	51
28	96	188	148	396	134	264	87	171	76	181	180	143	49	128	45	41
16	7	132	165	386	152	355	101	294	97	322	311	279	93	200	65	34
24	95	187	177	366	29	278	83	166	75	199	184	194	58	155	69	45
Spin Down																
12	1	85	132	346	128	305	109	260	99	341	319	277	96	104	30	11
20	45	201	169	414	155	294	81	218	87	223	286	241	94	214	66	49
28	135	201	193	404	149	288	86	169	66	185	183	189	78	169	58	64
16	4	162	194	392	185	337	116	237	111	326	339	280	84	217	69	42
24	94	207	200	433	161	318	95	203	73	245	268	248	78	186	64	47
Spin Off																
12	1	22	45	130	52	122	35	110	32	100	115	89	28	42	13	3
20	24	74	63	132	61	113	31	90	32	97	92	64	32	83	12	17
28	56	76	67	143	61	85	26	64	19	53	71	55	18	56	28	23
16	3	55	44	151	45	126	47	106	24	94	101	100	28	93	26	21
24	40	51	61	130	39	113	28	64	26	75	68	68	26	72	25	20
Large HE Angles (24.5° to 31.0°)																
Spin Up																
12	0	11	42	292	151	386	132	268	107	220	183	81	13	7	2	0
20	2	162	225	636	235	554	173	405	134	391	368	285	85	179	63	37
28	129	309	270	666	265	496	122	319	94	284	299	214	67	148	49	42
16	1	63	174	496	237	547	159	434	166	373	359	254	62	105	20	6
24	57	225	244	693	264	533	134	342	116	347	316	290	81	189	65	38
Spin Down																
12	1	7	57	276	139	394	96	302	98	229	164	70	9	9	2	0
20	3	191	239	581	210	516	166	379	152	373	330	317	84	196	53	38
28	141	305	286	600	222	443	110	295	119	264	268	257	83	181	73	52
16	1	74	168	484	213	479	152	412	137	370	339	251	66	100	20	6
24	44	265	274	608	218	487	125	370	133	321	312	286	88	190	55	46
Spin Off																
12	0	0	24	110	63	138	46	112	50	81	44	34	3	2	0	0
20	1	63	74	214	82	209	53	163	40	128	146	100	28	61	16	15
28	49	108	79	222	66	161	45	87	36	112	105	91	16	73	16	18
16	0	22	55	185	93	194	32	156	48	127	130	87	25	31	8	3
24	18	79	107	208	77	189	61	122	37	143	126	105	31	71	24	12

Table 5.8: Accumulated ppy event counts in the LAC.

LAC Random Counts																
Small HE Angles (18.0° to 24.5°)-																
Spin Up																
LE	Cerenkov Angle															
Angle	15	30	40	50	60	70	80	90	100	110	120	130	140	150	160	170
12	0	1	0	2	0	3	0	2	2	6	2	3	2	2	1	0
20	1	1	0	0	1	0	0	0	0	2	2	0	0	0	2	1
28	1	6	0	0	0	2	0	0	0	3	2	2	3	4	10	4
16	0	2	0	0	4	2	0	5	0	2	2	3	2	2	5	3
24	1	0	0	1	0	1	0	0	0	1	1	3	2	6	9	1
Spin Down																
12	0	4	0	3	1	5	1	3	1	3	7	6	1	3	1	2
20	1	5	1	2	0	1	0	1	1	0	1	0	0	0	1	5
28	1	3	2	0	0	2	1	4	3	0	1	7	1	1	3	5
16	1	3	1	0	1	2	0	2	0	3	1	4	3	5	6	2
24	1	3	0	0	1	1	2	1	1	2	6	2	0	3	8	6
Spin Off																
12	0	2	0	1	0	0	0	3	0	0	2	2	0	1	0	1
20	0	0	0	1	0	0	0	0	0	0	0	1	0	1	0	0
28	0	4	1	0	0	0	0	0	2	1	2	1	2	0	1	1
16	0	1	0	0	0	0	0	3	0	0	1	2	0	1	0	0
24	0	1	0	2	0	0	0	0	0	2	0	0	0	2	2	3
Large HE Angles (24.5° to 31.0°)																
Spin Up																
12	1	3	0	2	2	5	2	4	1	2	4	0	0	0	0	0
20	1	1	0	0	0	1	1	1	3	1	2	0	0	2	3	0
28	2	6	0	1	0	1	1	2	2	2	2	6	2	7	5	5
16	0	1	1	2	1	0	1	0	0	0	4	0	0	0	1	0
24	0	4	0	0	1	3	0	1	0	3	3	4	2	0	2	1
Spin Down																
12	1	2	1	2	2	3	0	4	2	5	3	4	0	0	0	1
20	0	6	0	2	1	1	1	4	2	7	2	3	1	1	1	2
28	0	5	0	0	2	4	0	1	2	7	4	6	1	9	10	6
16	0	1	0	3	0	2	1	5	0	6	2	4	1	0	0	0
24	0	3	1	1	3	1	3	3	2	4	6	0	1	4	6	6
Spin Off																
12	1	1	0	0	1	1	0	1	0	0	1	0	2	1	0	0
20	0	0	0	0	0	1	1	1	0	1	0	0	0	1	2	2
28	0	4	0	1	1	0	0	1	1	1	3	0	4	4	4	2
16	0	1	0	0	0	0	0	4	0	1	0	0	0	0	0	0
24	0	1	0	0	0	1	0	2	1	2	1	0	3	2	3	3

Table 5.9: Accumulated random counts in the LAC.

SAC ppy Counts																
Small HE Angles (9.9° to 14.8°)																
Spin Up																
LE Angle	Cerenkov Angle															
	15	30	40	50	60	70	80	90	100	110	120	130	140	150	160	170
12	20	102	61	191	49	128	34	124	28	167	84	219	68	312	64	208
20	62	86	54	169	47	108	30	69	28	100	39	129	36	161	40	178
28	51	57	40	114	31	73	15	43	11	61	14	76	16	56	17	79
16	25	104	81	184	55	151	34	88	24	116	73	177	51	180	68	235
24	61	95	52	169	30	93	16	53	13	73	32	79	30	118	34	131
Spin Down																
12	22	136	103	232	55	177	23	112	33	203	107	258	84	362	62	229
20	93	131	84	228	43	141	35	101	22	124	80	182	57	217	55	264
28	89	132	73	174	36	98	31	69	19	68	40	91	34	149	53	165
16	47	142	102	266	75	157	47	126	27	169	92	217	77	301	80	280
24	96	108	73	188	55	102	20	82	23	95	55	137	50	186	59	229
Spin Off																
12	6	26	23	48	25	45	10	35	9	50	27	72	28	108	24	66
20	19	33	23	52	11	35	9	29	6	43	16	28	13	51	21	83
28	22	21	19	48	8	21	6	16	5	22	16	21	10	30	13	36
16	13	42	24	75	11	33	23	23	8	33	13	52	23	97	22	72
24	18	26	27	55	18	29	7	19	5	27	11	25	9	52	8	53
Large HE Angles (14.8° to 19.8°)																
Spin Up																
12	0	67	109	398	137	344	97	337	103	359	133	330	81	190	27	33
20	31	151	132	443	124	301	71	250	60	281	125	239	89	284	97	228
28	85	156	137	434	104	275	59	168	42	179	60	159	47	163	40	139
16	2	127	157	467	123	373	90	251	63	326	150	285	85	249	74	159
24	61	161	131	434	123	284	78	220	65	221	105	188	70	225	56	201
Spin Down																
12	0	82	127	468	118	354	95	327	92	386	177	371	77	200	31	52
20	27	169	155	536	165	362	71	260	72	302	154	331	99	385	98	276
28	110	220	151	482	134	301	62	188	54	200	93	236	84	237	62	243
16	11	157	177	516	143	363	102	333	86	364	201	387	143	334	68	168
24	87	199	186	474	132	309	77	223	47	266	136	279	82	328	78	273
Spin Off																
12	0	20	42	126	42	96	30	79	27	111	53	83	27	72	9	6
20	12	53	47	153	46	112	21	58	28	74	38	97	29	109	19	65
28	25	50	54	16	34	84	17	61	22	58	27	59	25	52	10	60
16	5	27	48	139	29	134	33	85	22	95	53	118	34	94	23	55
24	18	67	41	141	43	80	16	60	14	54	26	75	31	74	18	62

Table 5.10: Accumulated ppy event counts in the SAC.

SAC Random Counts																
Small HE Angles (9.9° to 14.8°)																
Spin Up																
LE	Cerenkov Angle															
Angle	15	30	40	50	60	70	80	90	100	110	120	130	140	150	160	170
12	0	4	0	2	0	1	0	1	1	6	0	16	0	39	2	15
20	1	0	1	1	0	2	0	1	0	2	2	7	0	9	1	8
28	0	0	0	1	0	0	1	5	1	1	0	0	1	4	1	8
16	0	2	1	1	1	3	0	1	0	8	1	4	0	12	1	8
24	1	1	1	0	0	1	0	3	0	1	1	4	0	8	0	6
Spin Down																
12	3	3	0	3	0	0	0	3	1	8	1	15	0	47	3	26
20	1	0	1	1	0	1	0	0	0	6	2	6	0	11	0	12
28	0	1	0	2	0	1	0	3	0	2	0	2	0	10	0	9
16	2	3	0	6	0	4	0	2	0	4	1	9	0	12	1	13
24	0	1	0	1	0	0	0	0	0	2	0	1	0	7	1	11
Spin Off																
12	0	0	0	0	0	0	0	0	0	0	0	4	1	12	2	4
20	0	0	1	0	0	1	0	1	0	2	0	1	0	4	0	0
28	0	0	0	0	0	0	0	0	0	0	0	2	0	0	0	1
16	0	1	0	1	0	0	0	0	0	1	1	4	0	5	0	2
24	1	0	1	1	0	0	0	0	0	0	0	0	0	3	1	2
Large HE Angles (14.8° to 19.8°)																
Spin Up																
12	0	0	0	1	0	2	0	5	0	4	1	11	1	12	1	3
20	0	0	0	0	0	0	0	0	0	1	0	6	2	9	1	4
28	0	1	0	2	1	1	0	4	0	2	0	1	0	2	0	3
16	0	1	0	3	0	1	0	4	0	1	2	1	0	2	0	1
24	0	0	1	2	1	0	0	1	1	3	1	0	0	3	2	1
Spin Down																
12	0	0	0	1	0	0	0	5	1	14	0	10	1	8	3	4
20	0	1	1	0	0	1	0	1	0	4	1	2	2	15	0	7
28	0	1	1	6	1	2	0	1	0	1	0	2	2	4	1	3
16	0	2	0	2	1	1	0	0	0	3	0	5	2	9	1	4
24	0	0	0	1	0	0	0	2	0	1	1	2	3	4	1	2
Spin Off																
12	0	0	0	1	0	0	0	2	1	3	1	3	0	0	0	3
20	0	0	0	0	0	0	0	0	0	1	0	0	0	3	0	4
28	0	0	0	1	0	0	0	0	0	1	0	0	0	2	0	2
16	0	1	0	0	1	0	0	0	0	0	0	1	0	0	0	0
24	0	0	0	0	0	0	0	0	0	1	1	0	0	1	0	0

Table 5.11: Accumulated random counts in the SAC.

Chapter 6

Monte Carlo

6.1 Introduction

The collected $pp\gamma$ counts listed in tables 5.8 and 5.10 are plotted in figures 6.1 to 6.4 as a function of photon scattering angle for different proton opening angles. The events have been normalized for incident beam intensity, target thickness, and detector solid angle. These plots represent only what was observed at the end of a non-ideal detection system. To derive cross sections that can be compared with theoretical calculations, the efficiencies, multiple scattering, and phase-space acceptances, inherent in our experimental system, had to be accounted for. This amounted to nothing less than simulating the entire experiment in a software code, known as a Monte Carlo.

Events were generated at the target by observing conservation of energy and momentum, kinematics, and folding in phase-space and cross section, and then tracking these events through the experimental set-up to their

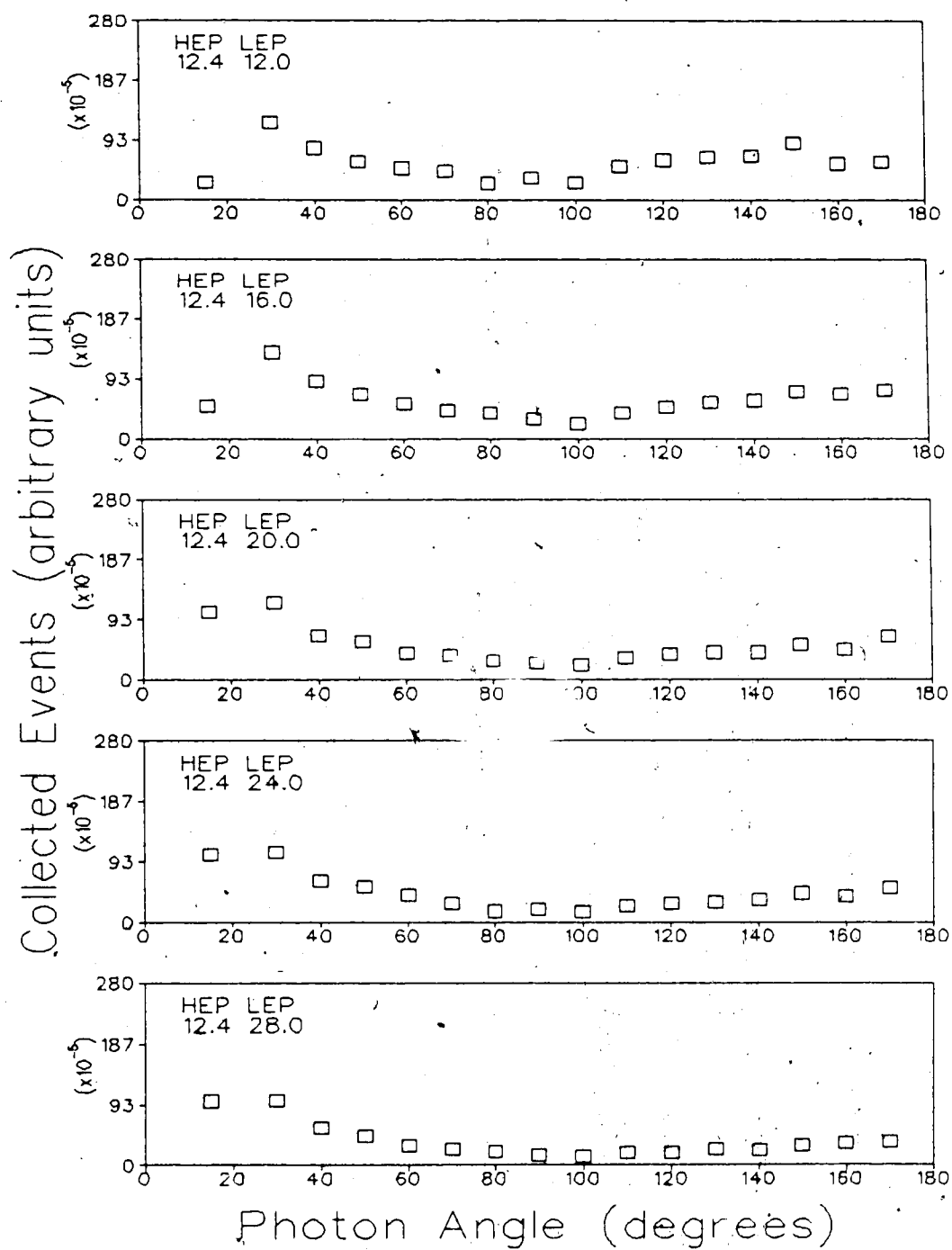


Figure 6.1: Raw collected ppy counts plotted as a function of photon scattering angle for the small angle SAC.

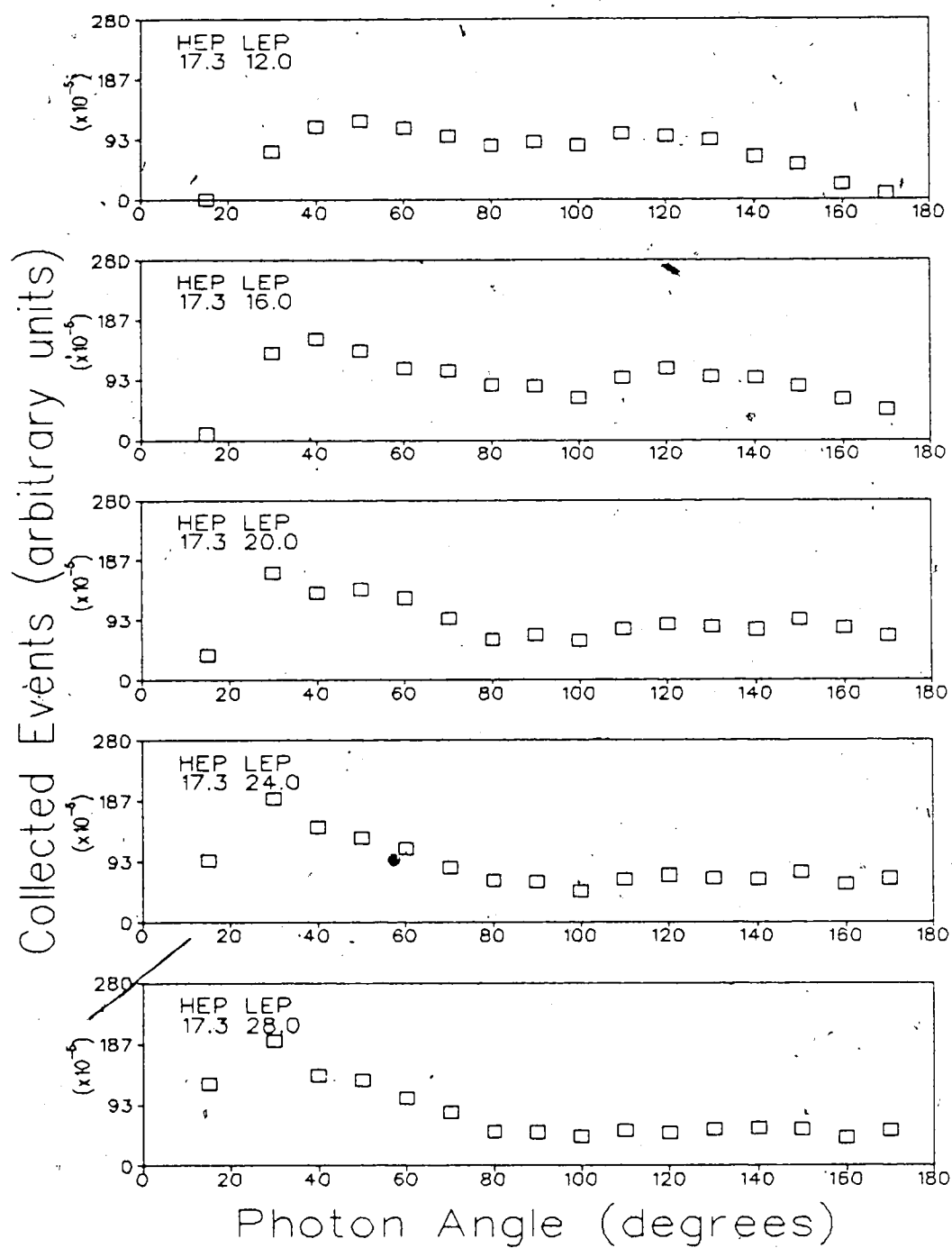


Figure 6.2: Raw collected $pp\gamma$ counts plotted as a function of photon scattering angle for the large angle SAC.

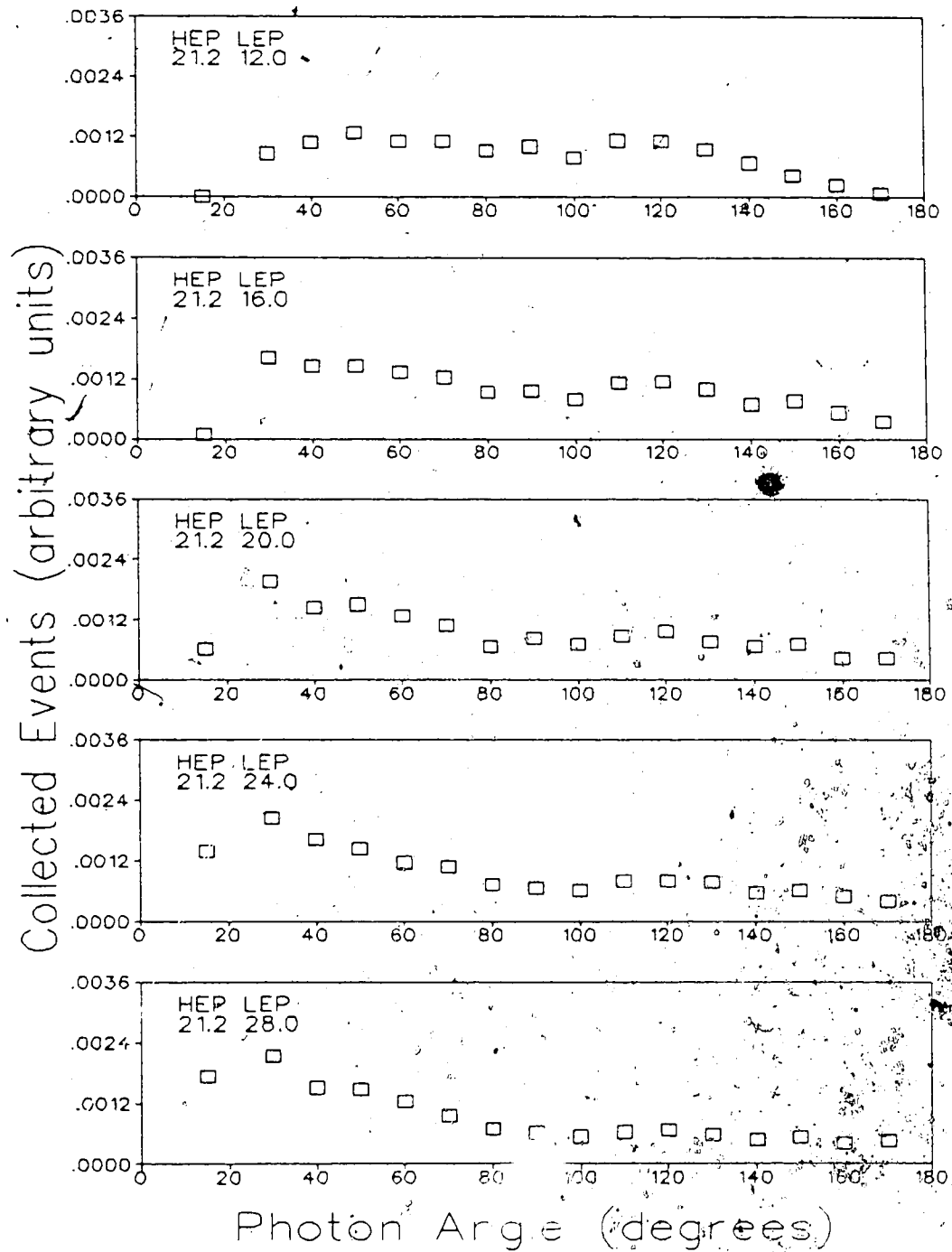


Figure 6.3: Raw collected $pp\gamma$ counts plotted as a function of photon scattering angle for the small angle LAC. Note the larger scale on the y-axis than for the SAC plots.

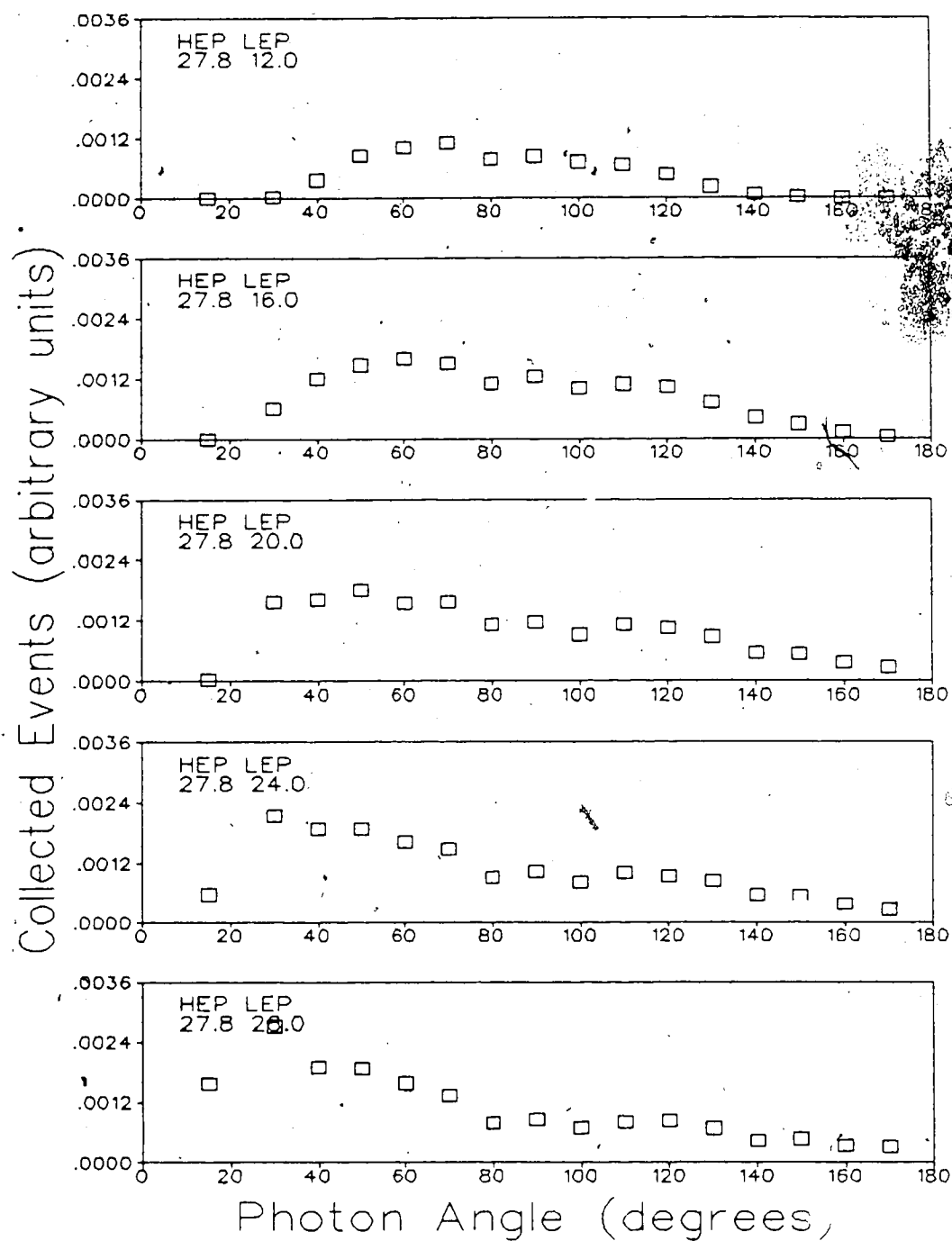


Figure 6.4: Raw collected $pp\gamma$ counts plotted as a function of photon scattering angle for the large angle LAC.

trigger counters.

The particles are tracked twice. First, to be called the IDEAL case, the particles are not affected after generation and the number of events that end up within the solid angles of the theoretical cross sections are counted. In the second trace, to be called the REAL case, events falling within the solid angles specified by the experimental detectors are counted and all the physics that could affect the particle on its trip to the trigger counters is taken into account. This includes multiple scattering and energy degradation as the protons traverse different materials, Compton scattering and pair production of the photon, the effect of the magnetic field on the protons, and also various inefficiencies in the particle detection systems.

These REAL events then represent what is actually detected by our system while the IDEAL events represent what we could hope to measure given the theoretical cross sections and an ideal detection system. The ratio of IDEAL/REAL events for a given 3-coincidence bin, represents the correction factor that must be applied to our measured data before they can be meaningfully compared with theory.

To some extent, the particular theoretical cross section folded into the event generation biases the values of these correction factors. This, however, arises only from the differences in the variation of the different theoretical predictions over the extent of a particular bin since both the REAL and IDEAL events have this same cross section folded in. The difference in variation of the cross sections derived from the Paris and Bonn potentials is small. Cross sections derived from the Paris potential were folded into our

event generation.

A flow chart of the Monte Carlo is given in figures 6.5 and 6.6 and a detailed description follows.

6.2 Description

The Monte Carlo was developed from the three-body event generating routine GDEC 3, taken from the CERN GEANT library. Before describing the code, we introduce some abbreviations, the coordinate system, and some approximations.

6.2.1 Abbreviations and Definitions

HEP - High energy proton - that detected on the opposite side of the beam line to the photon.

LEP - Low energy proton - that detected on the same side of the beam line as the photon.

SAC - Small angle configuration, $9.9^\circ < \theta_{HEP} < 19.8^\circ$.

LAC - Large angle configuration, $18.0^\circ < \theta_{HEP} < 31.0^\circ$.

VERTEX - Position within the H_2 target at which the event is generated.

TRACK - Direction cosines, coordinates, and 4 - momenta of a particle.

VDC - vertical drift chamber - used to determine the track of the HEP's.

REAL DETECTOR LIMITS - the actual physical limits of the detector plus an allowance for multiple in-scattering of the proton: equal to approximately

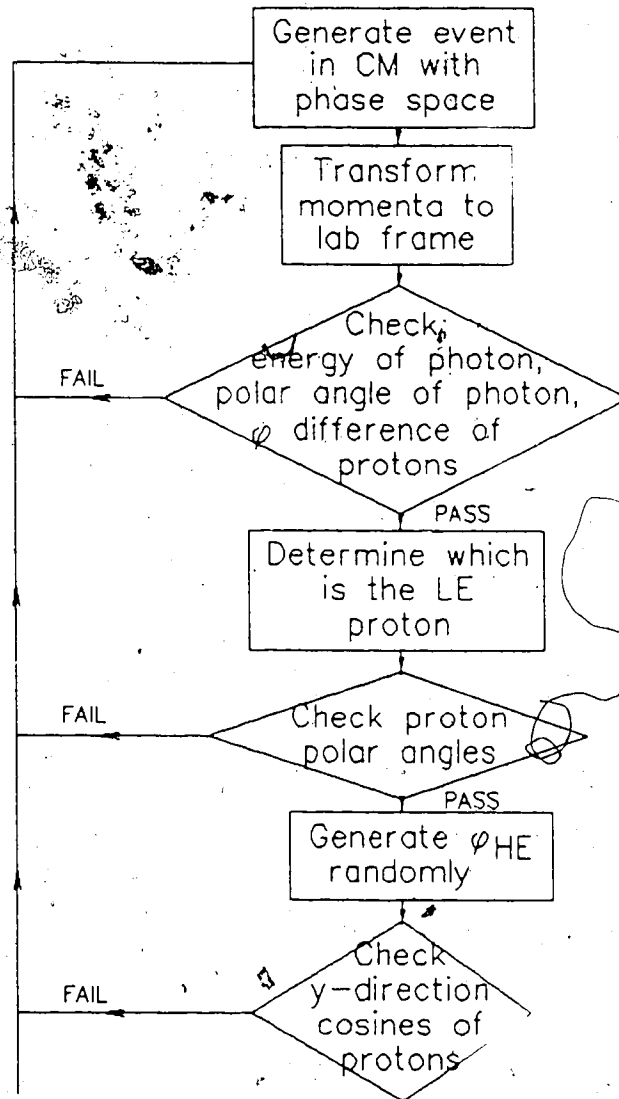


Figure 6.5: Flow chart of Monte Carlo code. Part one.

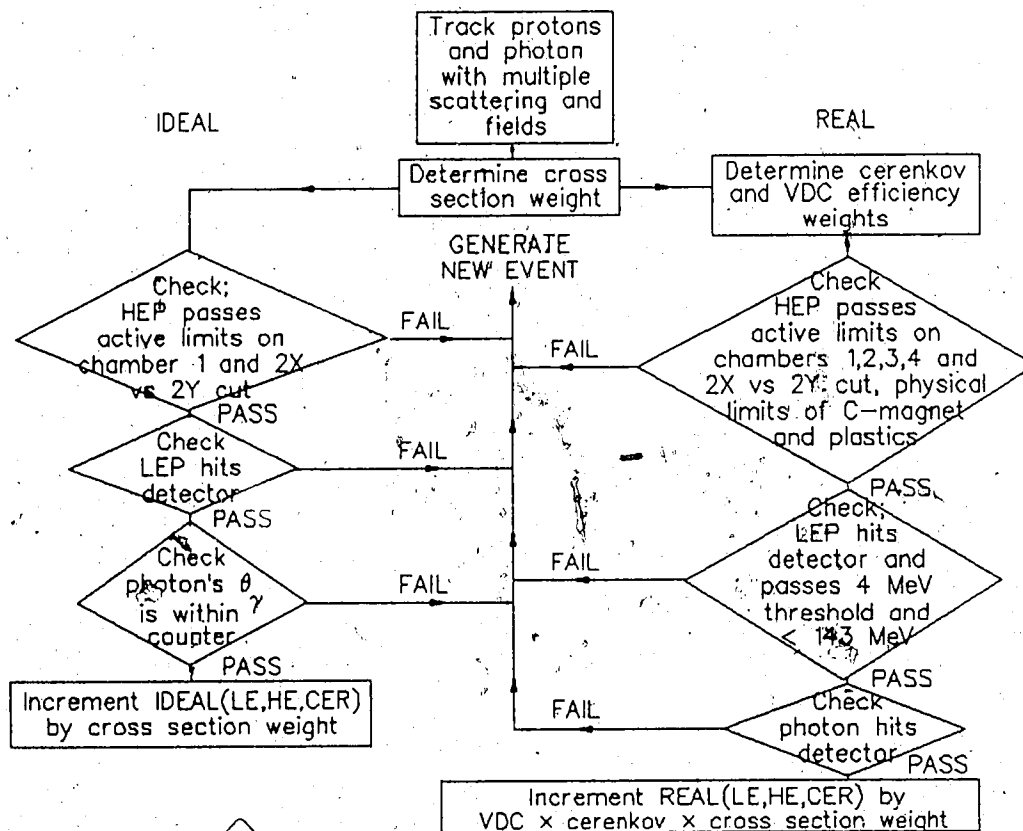


Figure 6.6: Flow chart of Monte Carlo code. Part two.

2.5 times the root mean squared multiple scattering of the proton at the detector.

MULTIPLE SCATTERING - multiple scattering plus energy loss.

6.2.2 The Coordinate System

Coordinates are given in a Cartesian system with the z-axis initially along the beam axis. Any rotation of the system is always about the vertical y-axis.

Multiple scattering distances listed are those measured along an axis parallel to the z-axis. The actual thickness the particle traverses will depend on its direction cosines.

6.2.3 Approximations

Although practically many simplifications and approximations had to be made, only those considered most serious (but justifiable), are listed below:

1. All events are generated within the 5 mm thick liquid hydrogen portion of the target. Without this simplification the geometry becomes complicated, making the efficiency for photon detection extremely difficult to calculate. The solid angle subtended by the cerenkov detectors would be a complicated function of vertex position along the target axis, and the amount of absorbing intervening material between the event vertex and the counters would be vertex position dependent. This approximation is justified since the detectors were shielded from

observing most of the gas. Also, good intrinsic resolution of the VDC's gave good definition of the liquid portion of the target to which a cut was applied.

2. No multiple scattering through air is calculated while the HE proton is in the field of the C-magnet because of the complication this presents to the ray tracing. The proton is however multiple scattered through an equivalent thickness of Cu divided into two sections placed just before and after the field.
3. The magnetic field drops to zero at the site of the anode plane of VDC 3. The field is actually $\sim 4\%$ of the gap field value in this region. To correct for this, the amplitude of the gap field was increased to give the correct angle of bend for protons of all energies.

6.3 Beam Proton

Before a ppy event is generated, a beam proton is created at the entrance to the 101.8 cm long H₂ target cylinder. Its x and y value at entrance is chosen at random from a gaussian beam profile centered at $x = y = 0$ with vertical/horizontal standard deviations of 2/2 mm, and its energy is chosen at random from a gaussian distribution centered at 280 MeV with a standard deviation of 2 MeV. The proton is then tracked with multiple scattering through the .05 mm thick kapton target end cap, 509 mm H₂ gas, .01 mm kapton (liquid H₂ tgt. window), and an amount $5.0 \times ran$ mm

of liquid H_2 , where ran = random number between 0 and 1 (distance the beam particle travels in the target before interacting strongly and producing a bremsstrahlung event).

6.4 Event Generation

The three-body event generator, GDECA3, of the CERN GEANT library was used. A bremsstrahlung event is generated uniformly in the c.m. system with the initial decay of the available energy into a proton and a piece that subsequently decays into the second proton and the photon. The events thus generated are weighted for phase space.

The 4-momentum vectors generated for each particle are then Lorentz transformed from the c.m. to the lab system. Spherical coordinates θ and ϕ are calculated for each particle from the lab momenta. A number of checks are made to make sure the event lies within a useful region of phase space.

These are, in order:

1. The energy of the photon must be above a generous limit of 35 MeV.
2. The polar angle θ_γ of the photon must be between 10° and 179° .
3. The difference between the azimuthal angles of the two protons must be $> 140^\circ$ (LAC), 120° (SAC). (The maximum ϕ subtended by the proton detectors is 14.5° for LEP detector #1, closest to the beam line. An allowance is made for multiple in-scattering.)

If any of these fail, a new event is generated.

Which of the protons is to be designated the LEP and HEP is now determined from their azimuthal angles ϕ and the ϕ of the photon. Checks are then made that:

1. The HEP's polar angle θ_{HEP} , is between 14° and 34° (LAC), 6° and 23° (SAC).
2. The LEP's polar angle θ_{LEP} , is between 8° and 32° (LAC), 6° and 34° (SAC).

A new event is generated if either of these fail.

Because the event is symmetric under a rotation of all particle momenta by ϕ about the beam axis, the efficiency for acceptance is increased by choosing a ϕ_{chosen} for the HEP proton at random between the limits set by the maximum ϕ allowed by the vertical solid angle cut on VDC 2 plus an allowance for multiple scattering, giving $\pm 15^\circ$ (LAC), $\pm 23^\circ$ (SAC), HE detector of $\pm 6.1^\circ$. The difference, $\phi_{shift} = \phi_{generated} - \phi_{chosen}$, is applied to the other particles by rotating their momenta through this amount. Because the detector limits are more uniform in θ^y (angle with respect to y-axis), acceptance efficiency is increased by checking that the particle's θ^y is within limits of $90 \pm 5.0^\circ$, (LAC) and (SAC), for the HEP and $90 \pm 5.0^\circ$ (LAC), $90 \pm 7.0^\circ$ (SAC) for the LEP. If not a new event is generated and the process repeated.

In summary, the following limits are used in deciding whether or not to

keep the event. If any of these fail, a new event is generated.

For the LAC,

1. $8^\circ < \theta_{LEP} < 32^\circ$,
2. θ_{LEP}^y within $\pm 5^\circ$ of x-z plane,
3. $14^\circ < \theta_{HEP} < 34^\circ$,
4. θ_{HEP}^y within $\pm 5^\circ$ of x-z plane,
5. $10^\circ < \theta_\gamma < 179^\circ$.

For the SAC,

1. $6^\circ < \theta_{LEP} < 34^\circ$,
2. θ_{LEP}^y within $\pm 7^\circ$ of x-z plane,
3. $6^\circ < \theta_{HEP} < 23^\circ$,
4. θ_{HEP}^y within $\pm 5^\circ$ of x-z plane,
5. $10^\circ < \theta_\gamma < 179^\circ$.

Generated events satisfying these limits were stored on magnetic tape for further processing.

6.5 Tracking

Tracking refers to the process of following the final state protons from their interaction point to their trigger counters. The two protons were tracked

twice. First, the 'ideal case', without multiple scattering, magnetic fields, finite ϕ_γ detector acceptance, or limited detector efficiencies. Second, the 'real case', with all the above. For a large part of the tracking the same code was used for both cases since a parameter passed to the multiple scattering routine allowed the multiple scattering to be turned on or off.

Tracking from the interaction point to the target cylinder window exit was identical for both the LE and HE proton as the target flask was symmetric with respect to the beam line. The materials through which the protons multiple scatter before passing the exit windows of the cylinder were, in order, $(0.5 - Z_{int})$ cm liquid H_2 , .01 mm kapton (liquid H_2 window), $2.5 - \sqrt{(x^2 + y^2)}/\tan(\theta)$ cm H_2 gas, as measured parallel to the incident beam axis, and finally through a .05 mm kapton window. Here θ is the proton polar angle and x and y are the coordinates of the proton at the liquid H_2 window. At this point the symmetry with respect to the beam line is broken and the tracking of the two protons differs.

6.5.1 Tracking the LE Proton

•The following tasks are performed for each of the LE detectors:

1. A transformation of the track of the proton is made into a new coordinate system, by rotating about the y-axis, with the origin kept at the center of the target but the z-axis at an angle θ corresponding to that of the center of each detector.

2. The x and y coordinates of the proton's track at a distance $z = 100$ cm, (approximate location of the LEP detectors), in this new coordinate system are determined. No multiple scattering is required here since in both the real and ideal case the proton is traversing vacuum.
3. These x and y values are checked to see if they lie within the extrapolated x (@100 cm) and y (@100 cm) limits of the particular LE detector. (Extrapolated limits are used since the distances to the LE detectors vary slightly from 93.3 cm to 104.35 cm.) If they are acceptable a flag is assigned the value of the detector number. In any case, the coordinates of the proton and its energy at this point are recorded.

6.5.2 Tracking the HE Proton

To facilitate tracking, the coordinate system is rotated by an angle of; 65.8° (LAC), 65.0° (SAC), about the y-axis, from the system's original configuration, so that the scattering chamber window and VDC's 1 and 2 are perpendicular to the new z-axis, (see figure 3.1).

For the 'ideal' case the HE proton is tracked to the sites of the X-anode planes of chambers 1 and 2, and the x,y coordinates saved and compared with the active limits of the plane. If the proton went through the active area, a flag is set. This completes the proton tracking for the 'ideal' case.

For the 'real' case the HE proton is multiple scattered through a 1/16 in. aluminum δ ray shield, through vacuum to the scattering chamber window, through a thickness .127 mm kapton window, and then multiple scattered

through air a distance that puts it 2 cm from the anode plane of VDC 1. Multiple scattering within the chamber is approximated by a thickness 0.279 mm mylar before the anode plane which is equivalent to the sum total of all foils and gas within the chamber. The x,y coordinates of the proton at this first anode plane are determined and saved. For this 'real' case VDC #2 is within the magnetic field of the dipole 'C' magnet and the field's effect on the track of the proton is considered. (The field at the site of the anode plane ranged from approx. $0 \rightarrow 10\%$ of the gap field of ~ 10 KG.) A transformation is made to a system with its origin at the center of the magnet and its z-axis perpendicular to the magnet's sides. The proton is multiple scattered in air to the beginning of the dipole field map just before VDC2. (The field map covers ± 76.2 cm along z and $+40.6, -81.3$ cm along x in this magnet coordinate system.)

The field map of the dipole magnet (taken at 7.987 KG. but scaled up to 10 KG) consisted of 31 planes perpendicular to the z-axis and spaced 5.08cm apart along z for which the field in the y - direction, as a function of x, was specified by 7 coefficients of a power series of x from x^0 to x^6 . The track of the proton is incremented 1.5 cm at a time until it reaches either the field map region or intersects the x anode plane of VDC 2. (Only part of chamber 2 is within the field map.) The two closest field planes are determined at each increment within the field region. The value of the field at the x-coordinate of the particle, on both planes, is calculated from the field coefficients, and the value of the field at the site of the proton is then determined by a linear interpolation between the two plane values. Direction cosines of the particle

are corrected for the field deflection over an arc length of 1.5 cm. If the track of the particle intersects chamber 2 before or while in the field, the x,y values at the anode plane are saved and a 'hit' flag set.

In the fringe field region, i.e. outside of the pole gap, the real field has horizontal components that could cause vertical focusing or defocusing of the HE protons depending on their direction of motion with respect to these components. To simulate this for the REAL case, use was made of Stoke's theorem which says that the integral of the components of a magnetic field around a closed loop must be zero, i.e.

$$\oint \vec{B} \cdot d\vec{l} = 0. \quad (6.1)$$

Figure 6.7 shows the situation. The problem is to determine the horizontal component of the field, B_z , given the gradient of the vertical field B_y . From the figure and equation 6.1,

$$B_z \cdot Z = (B_2 - B_1)Y. \quad (6.2)$$

where Z is the displacement between the two closest field planes to the proton, and Y is the vertical height of the proton from the median plane. $B_y(1)$ and $B_y(2)$ are the values of the vertical field at neighboring field planes. From the determined values of B_z , a vertical deflection for the proton was calculated and applied to its track at each increment of 1.5cm.

At a distance of 20 cm from the upstream pole edge, and at every increment until 20 cm after the downstream pole edge, the x-coordinate of the proton is checked to see if it is within the extent of the field map since the

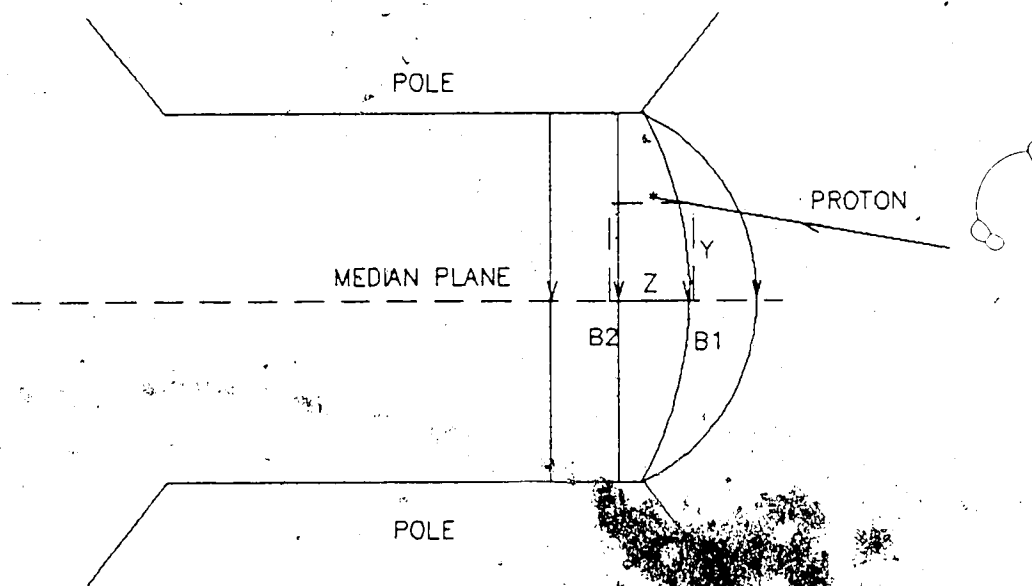


Figure 6.7: Use of Stoke's theorem to determine the vertically focusing horizontal components of the C-magnet field.

real physical limits of the magnet coils extend from ~ -20 cm to $+20$ cm beyond the pole in the z-direction and to the field map in the x-direction. At both the entrance and exit of the pole, the y-coordinate of the particle was checked to see if it is within the gap height of ± 5 cm. The protons are tracked through the field until they reach a distance of 27.5 cm (LAC), 40 cm (SAC), beyond the back of the magnet pole. (The field map extends further but continued tracking in the field introduces the extra complication of having VDC 3 within the field. The field along at the anode plane of VDC 3 ranges from $\sim 0 \rightarrow 5\%$ of the gap maximum. To compensate, the magnitude of the field is increased to give the correct bend to all protons.)

Next, a rotation is made of the coordinate system into one with the z-axis perpendicular to VDC's 3 and 4, with its origin at the target. The proton is multiple scattered in air until 2 cm before the anode plane of chamber 3, and then multiple scattered through a thickness of mylar equivalent to the thickness of chamber window material plus the chamber gas. The value of the coordinates at the anode plane are stored and a chamber hit or miss flag set. A similar procedure is followed through to chamber 4. Finally, the proton is multiple scattered in air to the HE detectors and checked on acceptance. The proton then suffers multiple scattering through a 3.18 mm aluminum cover plate on the back of VDC4, through air, and through the 6.35 mm thick plastic neutral veto and its 3.18 mm thick aluminum support, before finally arriving at the HE trigger detectors. This completes the tracking for the protons in the REAL case.

6.5.3 Tracking the Photon

For the 'ideal' case, the polar angle θ_γ of the photon is checked to see if it is within the polar angle subtended by a cerenkov counter in the horizontal plane containing the beam line.

For the 'real' case, the in-plane scattering angle of the photon is determined from the initial momentum components at the interaction point. If this angle is within the angle subtended by one of the cerenkov counters then the photon is projected to the face of this detector where the x and y coordinates (z-axis through the center of the detector) are determined. If the detector is a cube, a check is made to see if both the absolute value of x and y are less than the 1/2 width and height (7.46 cm), of the counter. If the detector is a cylinder, the quantity $\sqrt{x^2 + y^2}$ must be less than the 6.35 cm radius.

6.6 Efficiency Weighting and Binning

Ideal Events

For the 'ideal' case a cross section weight is determined by interpolating the square of the matrix element (cross section with phase space factor divided out), on a four dimensional grid of the variables, θ_γ , θ_{HEP} , θ_{LEP} , and ϕ_{LEP} , (obtained after a rotation such that $\phi_{HEP} = 0$). This number is normalized to a value between 0 and 1 by dividing it by the maximum $|matrix\ element|^2$ for the particular configuration, LAC or SAC.

An array IDEAL(LE,HE,CER) is incremented by an amount equal to the cross section weight if the following tests are passed:

1. The HEP passes within the active limits of chamber 1.
2. The HEP passes the solid angle cuts on anode planes 2X and 2Y which were applied to the experimental data.
3. The LEP hits one of its detectors.
4. The photon has a polar angle θ_γ within the polar angles subtended by one of the cerenkov detectors, as measured in the horizontal plane containing the beam line.

The binning indices have the following definitions; LE - low energy proton detector number; HE - each configuration has two HE bins corresponding to, LAC $18.0^\circ \rightarrow 24.5^\circ$ and $24.5^\circ \rightarrow 31.0^\circ$, and SAC $9.9^\circ \rightarrow 14.8^\circ$ and $14.8^\circ \rightarrow 19.8^\circ$; CER - cerenkov detector number.

Real Events

A cross section weight was determined as in the 'ideal' case.

The efficiency of each photon detector was determined at the upper and lower kinematic limits of the photon energy (for a given LE, HE, and CER bin) with a separate Monte Carlo program "EGS". This program determines the total energy deposited within the Pb glass by the electrons and positrons which develop as a result of the three photon interaction processes, the pho-

photoelectric effect, Compton scattering and pair production. Input to the program are, the type and an estimate of the amount of material intervening between the production point and the glass, the initial scattering angle with respect to the detector axis, the initial photon energy, and the material and thickness of the detector. (Figure 4.3 shows the location, and tables A.1 and A.2 the amount, of absorbing material between the target and cerenkov detectors.) The output consists of the number of photon events which deposit an energy within a given interval as a function of the average energy of the interval. The efficiency is calculated as the number of events with deposited energy above a 20 MeV discriminator threshold, divided by the total number of events. [An inefficiency correction is included to account for photon events that pair produce or Compton scatter in the absorber before the detector. The minimum ionizing electrons produced as a result deposit enough energy to trigger the charged particle veto that is in anti-coincidence with the Pb glass detectors.] Appendix A contains a complete description of the procedure used to obtain efficiencies from EGS.

A linear interpolation is made between calculated efficiencies at the two kinematic limits to determine it at the particular photon energy of the event.

The VDC efficiencies due to missing and multiple events were determined as follows from the '3% - even' (those not subjected to the cuts of the 'skimming' process). First, the area of each VDC plane was divided into 4 equal sections. The % not missing on a given plane was calculated as the ratio of those events which were good in all planes (i.e. not missing and not multiple), to those events that were good in all planes except had

a missing in the given plane plus those that were good in all planes. The position of the missing along a given plane was determined from the position of the track in a neighbor plane. Results for the LAC and SAC appear in tables 6.1 and 6.2 respectively. The % not multiple remaining after an attempt to resolve them (section 5.3) was determined from the ratio of those events that were good in all planes to those that were good in all planes except had a multiple in at least one plane plus those that were good in all planes. Table 6.3 shows these efficiencies as a function of position on anode plane 2X. The real events were weighted for the VDC efficiencies by determining what section of a particular chamber the event passed through, and then assigning the efficiency of that section to the event.

Cerenkov and LE detector not multiples were determined for a given detector from the ratio of those events which had a single cerenkov (or LE) hit over those that had a single hit plus those that were multiple. The results are given in tables 6.4 and 6.5.

Before an event was accepted and counted, a number of tests were placed on the energies of the two protons. The energy of the LEP at its detector had to be greater than 1 MeV to be accepted by the discriminators, and be less than 143 MeV or it would penetrate the absorber behind its detector and trigger its elastic veto counter. Also the energy of the HEP at its plastic detectors had to be greater than the discriminator threshold of 1 MeV.

In summary, an array REAL(LE,HE,CER) was incremented by an amount equal to the product of the weights of the cross section, VDC not multiple

large \rightarrow small angles					
VDC 1X	\uparrow	.845	.833	.836	.813
	\downarrow	.860	.860	.863	.849
	off	.840	.842	.850	.826
VDC 2X	\uparrow	.951	.933	.949	.953
	\downarrow	.958	.941	.952	.956
	off	.952	.937	.952	.954
VDC 2H	\uparrow	.848	.882	.928	.946
	\downarrow	.843	.874	.928	.960
	off	.842	.889	.924	.961
VDC 3X	\uparrow	.963	.975	.981	.921
	\downarrow	.961	.976	.983	.934
	off	.950	.972	.982	.927
VDC 4X	\uparrow	.966	.978	.962	.866
	\downarrow	.970	.981	.962	.866
	off	.974	.980	.966	.860

Table 6.1: VDC not missing efficiencies for the LAC.

large \rightarrow small angles					
VDC 1X	\uparrow	.781	.750	.717	.660
	\downarrow	.808	.773	.748	.693
	off	.789	.762	.736	.682
VDC 2X	\uparrow	.858	.960	.956	.900
	\downarrow	.856	.969	.957	.900
	off	.865	.956	.960	.902
VDC 2H	\uparrow	.955	.958	.961	.956
	\downarrow	.959	.963	.967	.960
	off	.961	.959	.963	.959
VDC 3X	\uparrow	.911	.976	.981	.974
	\downarrow	.919	.978	.981	.975
	off	.913	.974	.982	.976
VDC 4X	\uparrow	.925	.978	.979	.970
	\downarrow	.916	.975	.978	.971
	off	.934	.976	.978	.972

Table 6.2: VDC not missing efficiencies for the SAC.

large \rightarrow small angles					
(LAC)	\uparrow	.747	.758	.787	.806
	\downarrow	.820	.833	.857	.876
	off	.765	.783	.824	.826
(SAC)	\uparrow	.727	.760	.804	.828
	\downarrow	.802	.824	.853	.873
	off	.755	.786	.822	.849

Table 6.3: VDC not multiple efficiencies for the LAC and SAC as a function of position on anode plane 2N.

		12°	16°	20°	24°	28°
(LAC)	\uparrow	.957	.916	.916	.912	.938
	\downarrow	.942	.907	.908	.905	.929
	off	.948	.912	.910	.907	.934
(SAC)	\uparrow	.972	.928	.922	.916	.939
	\downarrow	.960	.922	.912	.907	.928
	off	.966	.927	.917	.912	.934

Table 6.4: LE detector not multiple efficiencies for the LAC and SAC.

	15°	30°	40°	50°	60°	70°	80°	90°
(LAC) ↑	.978	.984	.975	.979	.966	.979	.964	.979
↓	.978	.985	.975	.979	.969	.980	.968	.981
off	.978	.985	.973	.978	.966	.979	.967	.979
	100°	110°	120°	130°	140°	150°	160°	170°
(LAC) ↑	.962	.967	.964	.973	.952	.980	.984	.986
↓	.968	.972	.968	.975	.957	.981	.985	.985
off	.963	.968	.966	.973	.953	.981	.983	.985
	15°	30°	40°	50°	60°	70°	80°	90°
(SAC) ↑	.972	.975	.960	.973	.950	.970	.953	.974
↓	.973	.975	.960	.975	.952	.970	.956	.975
off	.973	.975	.959	.974	.952	.968	.955	.974
	100°	110°	120°	130°	140°	150°	160°	170°
(SAC) ↑	.955	.978	.950	.976	.949	.983	.963	.982
↓	.956	.978	.955	.976	.952	.983	.965	.984
off	.955	.978	.956	.976	.954	.983	.964	.983

Table 6.5: Cerenkov detector not multiple efficiencies for the LAC and SAC.

and not missing efficiency, cerenkov detection (see appendix A for a table of values) and not multiple efficiency, and LE not multiple efficiency, if the following tests were satisfied:

1. The HEP passed within the active limits of all chambers (1,2,3 and 4).
2. The HEP was within solid angle cuts on anode planes 2X and 2Y that were applied to the experimental data.
3. The HEP passes within the physical limits of the C-magnet.
4. The HEP passes within the physical limits of its plastic trigger counters.
5. The energy of the HEP at its trigger counters is above 1 MeV.
6. The LEP hits one of its detectors.
7. The energy of the LEP at its detector is above a 1 MeV threshold.
8. The energy of the LEP at its detector is below 143 MeV.
9. The photon passes within the physical limits of a cerenkov detector.

The ratio of IDEAL/REAL was used to correct the experimental counts in a given bin before the cross sections were formed. Values of this ratio for the LAC and SAC are given in tables 6.6 and 6.7 respectively.

LAC Ratio of Ideal to Real Monte Carlo Counts																
Small HE Angles (18.0° to 24.5°)																
LE Angle	Cerenkov Angle															
	15	30	40	50	60	70	80	90	100	110	120	130	140	150	160	170
12			9.0	6.3	9.7	6.8	11.6	12.4	19.6	12.3	12.3	15.5	28.3	26.0	42.8	
16		8.2	10.1	6.9	10.8	7.3	13.0	14.5	17.1	11.8	13.0	15.1	29.8	25.6	46.2	
20		10.5	9.2	7.3	13.4	8.2	13.7	14.5	21.2	12.7	13.6	16.7	27.4	24.6	41.0	27.8
24	9.9	9.9	12.1	8.3	11.3	9.5	17.6	17.6	21.4	14.2	18.1	20.4	28.7	25.8	39.6	37.6
28	11.1	10.8	12.1	9.8	13.3	9.5	20.3	18.8	25.5	15.6	20.2	23.3	46.1	29.0	46.7	31.7
Large HE Angles (24.5° to 31.0°)																
12					12.3	8.3	14.1	15.9	22.5	15.2	18.7	31.8	99.7			
16				8.0	11.4	9.4	15.3	15.9	22.2	15.2	16.0	19.5	41.8	37.4	88.0	
20			12.7	9.2	11.6	9.4	15.6	16.4	22.4	15.1	16.2	20.3	38.1	30.5	48.7	
24		11.7	12.0	9.3	12.3	10.1	18.5	19.0	20.9	14.5	17.3	21.4	42.4	31.1	56.6	38.8
28	12.8	11.1	11.5	9.2	15.0	9.6	18.9	20.1	27.8	20.8	21.5	21.7	54.1	33.2	40.3	40.3

Table 6.6: Ratio of IDEAL to REAL monte carlo counts for the LAC.

SAC Ratio of Ideal to Real Monte Carlo Counts																
Small HE Angles (9.9° to 14.8°)																
LE Angle	Cerenkov Angle															
	15	30	40	50	60	70	80	90	100	110	120	130	140	150	160	170
12		8.4	11.0	6.5	9.3	7.1	9.9	11.6	17.6	9.2	16.8	12.4	24.5	14.5	31.2	17.0
16	10.7	6.7	9.8	6.7	10.7	8.7	15.5	12.6	20.9	12.3	14.9	14.4	25.3	17.5	32.1	18.2
20	11.0	8.6	9.5	7.9	10.9	8.9	12.9	12.3	18.7	12.5	16.0	14.5	29.2	15.3	40.8	17.2
24	10.7	11.0	12.7	7.8	12.7	9.0	21.1	15.4	16.5	11.2	20.2	12.3	28.6	19.8	37.8	19.0
28	11.5	10.5	12.5	7.0	16.9	9.1	22.0	16.8	16.7	14.7	17.3	18.8	47.9	18.6	43.3	17.2
Large HE Angles (14.8° to 19.8°)																
12					10.4	7.0	14.3	12.0	18.0	10.5	16.0	13.3	27.6	29.7	71.3	
16				6.8	9.9	7.1	13.6	11.8	20.6	11.7	14.6	13.2	26.4	19.5	39.8	
20			11.4	6.8	11.1	7.4	15.5	13.9	24.8	10.7	16.5	15.6	33.1	20.3	48.0	20.6
24		10.4	11.0	7.3	11.6	7.8	14.6	13.8	20.3	11.7	19.4	14.7	30.6	21.1	37.0	19.4
28		9.0	12.2	8.5	10.7	8.7	14.0	15.9	22.1	13.2	17.1	19.4	36.3	21.0	48.5	20.0

Table 6.7: Ratio of IDEAL to REAL monte carlo counts for the SAC.

Chapter 7

pp γ Analyzing Powers and Cross Sections

7.1 Analysing Powers

The ratio of the difference of the spin up and spin down pp γ cross sections over their sum was taken to form the pp γ analyzing powers. (The polarization of the incident proton beam was cycled through three minutes of spin up, one minute of spin off, three minutes of spin down, and one minute of spin off again.) The analysing powers were obtained from the accumulated pp γ counts according to

$$A_y = \frac{(N^\uparrow - R^\uparrow)/n_{inc}^\uparrow LT^\uparrow - (N^\downarrow - R^\downarrow)/n_{inc}^\downarrow LT^\downarrow}{P^\uparrow(N^\uparrow - R^\uparrow)/n_{inc}^\uparrow LT^\uparrow + P^\downarrow(N^\downarrow - R^\downarrow)/n_{inc}^\downarrow LT^\downarrow}$$

The real $N^{l(l)}$ and random $R^{l(l)}$ counts collected in a given bin are listed in tables 5.8 to 5.11. The number of incident protons $n_{inc}^{l(l)}$ was determined from the SEM counts N_{SEM} as

$$n_{inc}^{(1)} = N_{SEM}^{(1)} / (NI \cdot 1.0 \times 10^9 nC / C \cdot 1.602 \times 10^{-19} C / \text{proton})$$

Here $N_{SEM}^{(1)}$ is the total number of SEM counts in the spin up(down) mode, and NI is the number of SEM counts per nC of charge, determined by calibrating the SEM with a Faraday cup shortly after the data taking runs. This number was found to equal 7.122 and gives the number of incident protons for spin up, down and off as, respectively, 1.691×10^{16} , 1.664×10^{16} , 6.894×10^{15} (LAC) and 2.531×10^{16} , 2.638×10^{16} , 7.660^{15} (SAC). The polarization of the incident beam was determined from the polarimeter scalars as

$$P^{(1)} = \frac{1}{A(CH_2)} \cdot \frac{(L^{(1)} - L_{acc}^{(1)}) - (R^{(1)} - R_{acc}^{(1)})}{(L^{(1)} - L_{acc}^{(1)}) + (R^{(1)} - R_{acc}^{(1)})} \quad (7.1)$$

Here $L^{(1)}, R^{(1)}$ is the number of left, right polarimeter coincidences, and $L_{acc}^{(1)}, R_{acc}^{(1)}$ is the number of left, right accidental coincidences. (See Section 4.1.2) $A(CH_2)$ is the analysing power of the polarimeter, determined to be .3719 from an empirical formula which gives the ratio of the analysing power of CH_2 over that of hydrogen as a function of incident proton energy T_p :

$$\frac{A(CH_2)}{A(H)} = 1.0830 - \left(\frac{T_p}{100} \right) \left[.07486 - \left(\frac{T_p}{100} \right) .00823 \right]$$

For an incident energy of 280 MeV, $A(H) = .3965$, and the values of the polarization from equation 7.1 for spin up and down, corrected for the instrumental asymmetry of the polarimeter, are respectively 73.6%, 76.6% (LAC), and 78.0%, 74.2% (SAC). Computer live time $LT^{(1)}$ was determined as the ratio of the number of pulser events setting the latch and recorded on tape to the number of pulser triggers submitted to the system, counted with

a scaler. The pulsers were triggered off the polarimeter coincidences (section 4.1.9) so they scaled with the real 3-coincidence $pp\gamma$ events, and thus gave an accurate measure of the real live time. In the spin up, down and off mode, live time was respectively 80.91%, 82.90%, 77.95% (LAC) and 79.37%, 79.75%, 79.09% (SAC).

The statistical error in the analysing power is calculated as

$$1_{\nu} = \sqrt{\left(\frac{\partial A_{\nu}}{\partial N^I}\right)^2 (\delta N^I)^2 + \left(\frac{\partial A_{\nu}}{\partial R^I}\right)^2 (\delta R^I)^2 + \left(\frac{\partial A_{\nu}}{\partial N^{\perp}}\right)^2 (\delta N^{\perp})^2 + \left(\frac{\partial A_{\nu}}{\partial R^{\perp}}\right)^2 (\delta R^{\perp})^2},$$

where $\delta N^{I(\perp)} = \sqrt{N^{I(\perp)}}$, and $\delta R^{I(\perp)} = \sqrt{R^{I(\perp)}}$.

The analysing powers and these statistical errors are plotted in figures 7.1 to 7.4 along with theoretical calculations for the Bonn and Paris potential models, as well as the Soft Photon Approximation (SPA). (Chapter 2 and appendix D contain a complete description of these curves.) For the plots at LE angles 14° and 22° , two adjacent LE bins were added together to improve the experimental statistics. Angles listed on these plots correspond to the center of an 8° wide LE bin. The plots at an LE angle of 28° contain only a single bin 4° wide. The HE bins for all plots are 5° wide. The abscissa is photon detection angle, divided into 16 bins of width ranging from approximately 5° (cylinders) to approximately 11° (cubes), (see Appendix E).

The theoretical curves plotted have been averaged over 4 coplanar points equally spaced within the HE and LE bins for 18 cerenkov angles equally spaced between 0° and 180° . Tables 7.1 and 7.2 show the ratio of the relative error of this procedure to the statistical error of the sample data within the bin, for the LAC and SAC. This relative error is defined as the

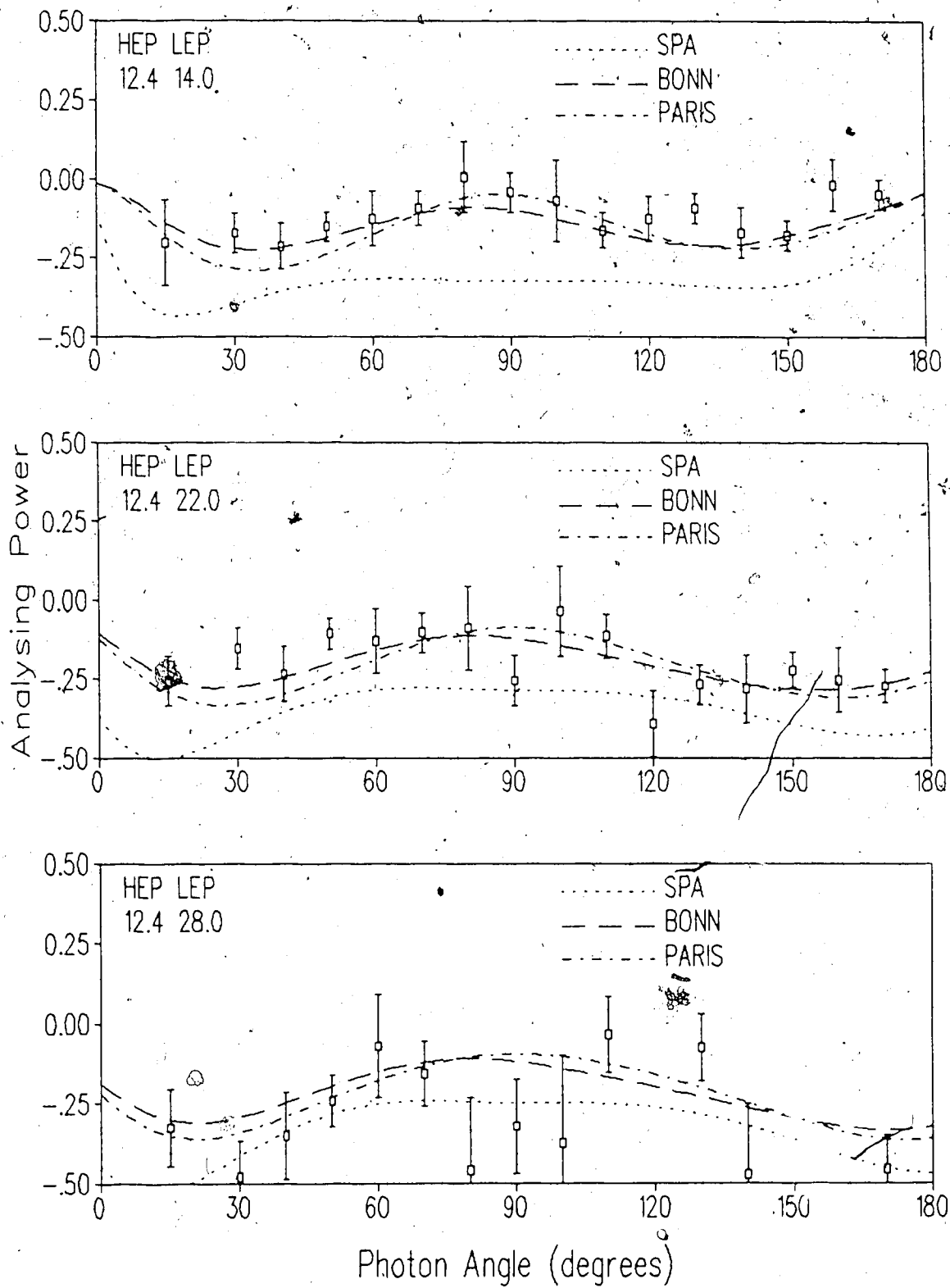
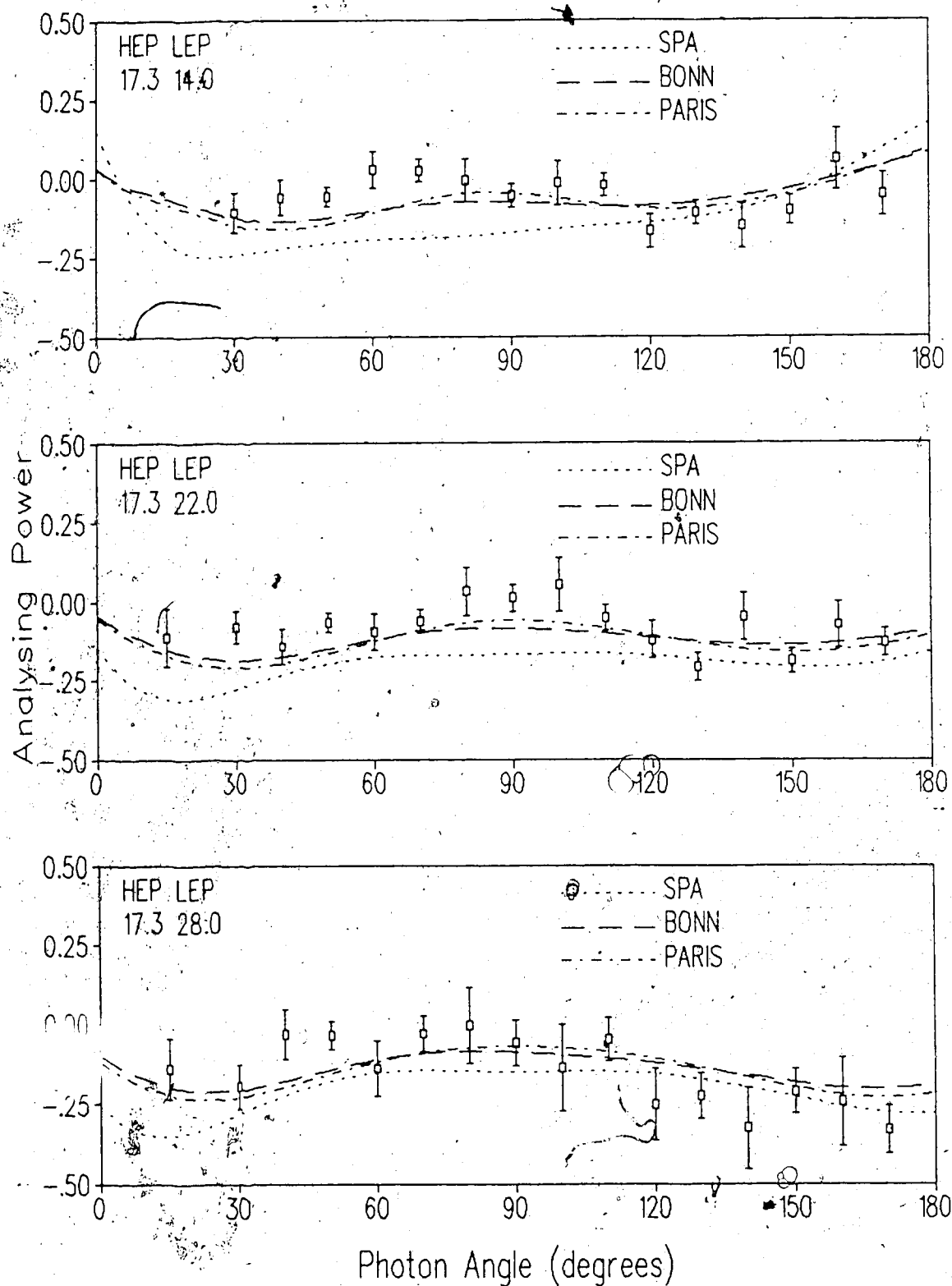


Figure 7.1: $pp\gamma$ analysing powers for the small angle SAC.

7.2: $pp\gamma$ analysing powers for the large angle SAC.

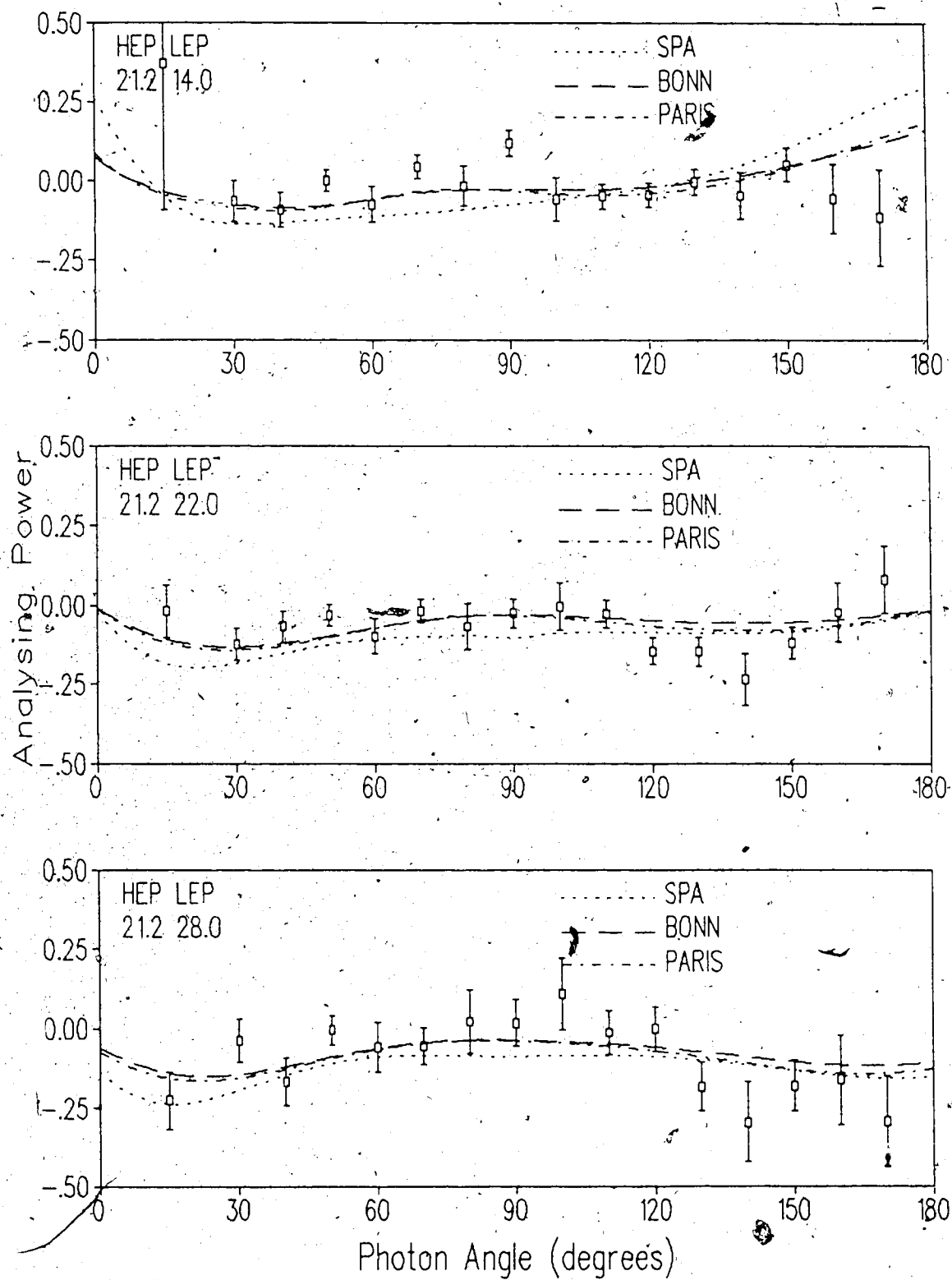


Figure 7.3: $pp\gamma$ analysing powers for the small angle LAC.

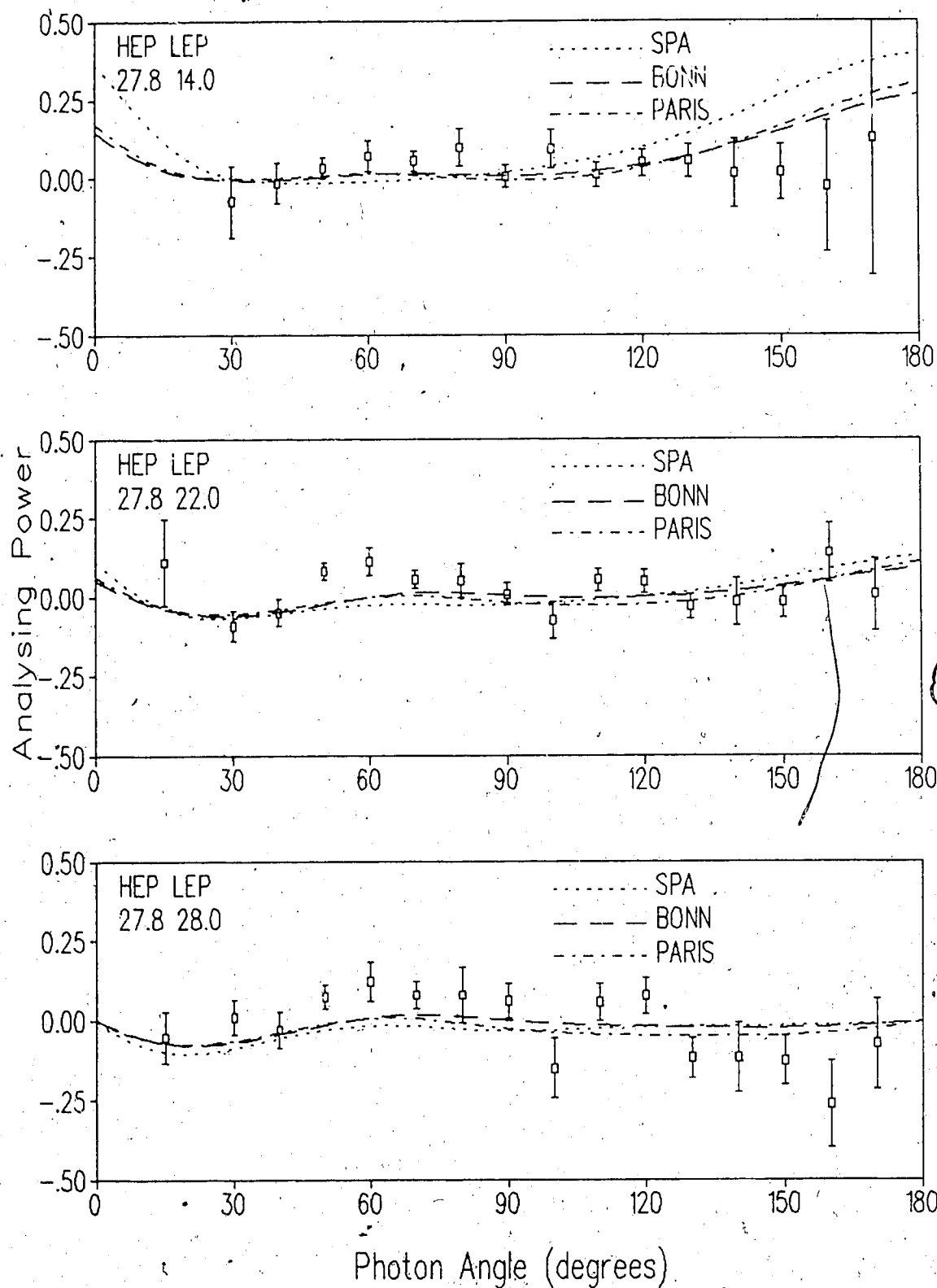


Figure 7.4: $pp\gamma$ analysing powers for the large angle LAC.

difference in the analysing power determined by a cross section weighted 4 point coplanar average and the cross section weighted 16 point non-coplanar average. Generally the error is less than 2% with the worst cases being 5.8% (LAC) and 4.9% (SAC).

7.2 $pp\gamma$ Cross Sections

The three-fold unpolarized differential cross sections $\frac{d^3\sigma}{d\Omega_{HE}d\Omega_{LE}d\theta_\gamma}$, were calculated from the number of $pp\gamma$ events collected within a bin $\delta\Omega = \delta\Omega_{HE}\delta\Omega_{LE}\delta\theta_\gamma$ as;

for the incident beam polarized data,

$$\left. \frac{d^3\sigma}{d\Omega_{HE}d\Omega_{LE}d\theta_\gamma} \right|_{\uparrow\uparrow} = \frac{Z}{P^\uparrow + P^\downarrow} \left[\frac{P^\uparrow(N^\uparrow - R^\downarrow)}{n_{inc}^\uparrow LT^\uparrow} + \frac{P^\downarrow(N^\downarrow - R^\uparrow)}{n_{inc}^\downarrow LT^\downarrow} \right];$$

and for the incident beam unpolarized data,

$$\left. \frac{d^3\sigma}{d\Omega_{LE}d\Omega_{LE}d\theta_\gamma} \right|_0 = Z \left[\frac{n^\circ - R^\circ}{n_{inc}^\circ LT^\circ} \right].$$

- Here

$$Z = \frac{\epsilon(\delta\Omega)}{\delta\Omega_{HE}\delta\Omega_{LE}\delta\theta_\gamma n_{tgt} t}$$

where $\epsilon(\delta\Omega)$ is the Monte Carlo correction factor, for a given bin $\delta\Omega$, determined from the ratio of IDEAL to REAL events as listed in tables 6.6 and 6.7. n_{tgt} is the number of target protons per unit volume, which for liquid hydrogen is $= 4.222 \times 10^{22}/cm^3$. The target thickness t was nominally 0.500 cm but re-normalized by comparing the measured cross section for pp elastic scattering to the expected value (appendix B). The results were .385cm

θ_γ	ΔA_y^{theo}	$\frac{\Delta A_y^{theo}}{\Delta A_y^{exp}}$	$\Delta \sigma^{theo}(mb)$	$\frac{\Delta \sigma^{theo}}{\Delta \sigma^{exp}}$
degrees	$\times 10^{-3}$	%	$\times 10^{-4}$	%
15	0.796	0.9	0.208	5.8
30	0.208	0.4	0.118	3.6
40	0.174	0.3	0.090	2.2
50	0.509	0.7	0.089	3.4
60	0.851	1.3	0.100	1.8
70	1.120	2.5	0.122	5.8
80	1.140	1.3	0.152	3.6
90	0.953	1.8	0.188	5.1
100	0.774	0.8	0.231	4.0
110	0.650	1.1	0.285	8.6
120	0.548	1.0	0.366	11.1
130	0.390	0.6	0.504	19.6
140	0.089	0.1	0.762	9.4
150	0.580	0.7	1.400	41.
160	2.620	1.7	4.190	96.1
170	9.190	5.8	1.200	21.8

Table 7.1: The error introduced by averaging over only 4 coplanar points ΔA_y^{theo} and $\Delta \sigma^{theo}$, and the ratio of this error to the statistical experimental error. Results are for an HE bin centered at 27.8° and a 4° wide LE bin centered at 28.0° (LAC).

θ_γ	ΔA_y^{theo}	$\frac{\Delta A_y^{theo}}{\Delta A_y^{exp}}$	$\Delta \sigma^{theo}(mb)$	$\frac{\Delta \sigma^{theo}}{\Delta \sigma^{exp}}$
degrees	$\times 10^{-3}$	%	$\times 10^{-5}$	%
15	0.524	0.4	0.164	0.7
30	0.541	0.8	0.113	1.1
40	0.599	0.8	0.119	0.4
50	0.610	1.3	0.144	1.5
60	0.529	0.6	0.179	0.9
70	0.365	0.6	0.218	2.5
80	0.196	0.2	0.257	2.2
90	0.134	0.2	0.296	2.3
100	0.194	0.1	0.336	1.8
110	0.291	0.5	0.382	3.4
120	0.451	0.6	0.401	1.2
130	0.488	1.0	0.470	2.9
140	0.678	0.8	0.713	1.3
150	0.952	2.1	1.070	4.6
160	1.330	1.6	2.230	4.6
170	2.290	4.9	8.690	42.6

Table 7.2: The error introduced by averaging over only 4 coplanar points ΔA_y^{theo} and $\Delta \sigma^{theo}$, and the ratio of this error to the statistical experimental error. Results are for an HE bin centered at 12.4° and a 4° wide LE bin centered at 12.0° (SAC).

(LAC) and .388cm (SAC). The solid angle bin $\delta\Omega_{LE}$ was that subtended by the LE plastic scintillators, approximately 6.086 msr (appendix E). The solid angle bin $\delta\Omega_{HE}$ was that subtended by a software cut, applied during the analysis of the experimental data, to VDC2 X vs H scatter plot (appendix E). (This cut was also applied to both the REAL and IDEAL Monte Carlo events.) The polar angle subtended by a particular cerenkov counter $\delta\theta_\gamma$, had values ranging from 4.4° (cylinders) to 10.7° (cubes). Appendix E contains a list of these.

$P^{(1)}$ is the incident beam polarization in the spin up and down modes as outlined in section 7.1.

$N^{(1)(o)}$ are the number of real $pp\gamma$ events collected within a particular bin, listed in tables 5.8 and 5.10.

$R^{(1)(o)}$ are the number of random 3-coincidence events collected within a particular bin, listed in tables 5.9 and 5.11.

$n_{inc}^{(1)(o)}$ are the number of incident beam protons obtained from the spin gated SEM counts as calculated in section 7.1.

The system live times $LT^{(1)(o)}$ were obtained from the pulser events, as described in section 7.1.

The total unpolarized differential cross sections were obtained by combining the unpolarized with the polarized data,

$$\sigma = \frac{\sigma^{11}/(\delta\sigma^{11})^2 + \sigma^0/(\delta\sigma^0)^2}{1/(\delta\sigma^{11})^2 + 1/(\delta\sigma^0)^2}$$

where σ is short for $\frac{d^3\sigma}{d\Omega_{LE}d\Omega_{HE}d\theta_\gamma}$.

Statistical errors in the cross sections were calculated as,

$$\delta\sigma^{(1)} = \sqrt{\left[\frac{\partial\sigma^{(1)}}{\partial N^1}\right]^2 (\delta N^1)^2 + \left[\frac{\partial\sigma^{(1)}}{\partial R^1}\right]^2 (\delta R^1)^2 + \left[\frac{\partial\sigma^{(1)}}{\partial N^1}\right]^2 (\delta N^1)^2 + \left[\frac{\partial\sigma^{(1)}}{\partial R^1}\right]^2 (\delta R^1)^2}$$

$$= \frac{Z}{P^1 + P^1} \sqrt{\left[\frac{P^1}{n_{inc}^1 LT^1}\right]^2 (N^1 + R^1) + \left[\frac{P^1}{n_{inc}^1 LT^1}\right]^2 (N^1 + R^1)} \quad (7.2)$$

$$\delta\sigma^o = \sqrt{\left[\frac{\partial\sigma^o}{\partial N^o}\right]^2 (\delta N^o)^2 + \left[\frac{\partial\sigma^o}{\partial R^o}\right]^2 (\delta R^o)^2} = \frac{Z}{LT^o n_{inc}^o} \sqrt{N^o + R^o}$$

The error in the combined cross section is,

$$\delta\sigma^o = \sqrt{\frac{1}{1/(\delta\sigma^{(1)})^2 + 1/(\delta\sigma^o)^2}}$$

Cross sections with statistical errors are plotted in figures 7.5 to 7.12, along with theoretical curves for the Bonn, Paris and Soft Photon Approximation. The data is normalized arbitrarily by multiplying by a factor of 0.667. (A discussion of this factor is left to section 8.1.)

Because of the sensitivity of the Monte Carlo correction factors to the amount of absorbing material and angle of bend through the magnet, for lower energy protons, only those cross section bins are plotted for which less than 10% of the REAL events were lost due to one or more of the following effects:

1. penetration of the higher energy LE protons through their CH₂ absorber and into their veto counters,

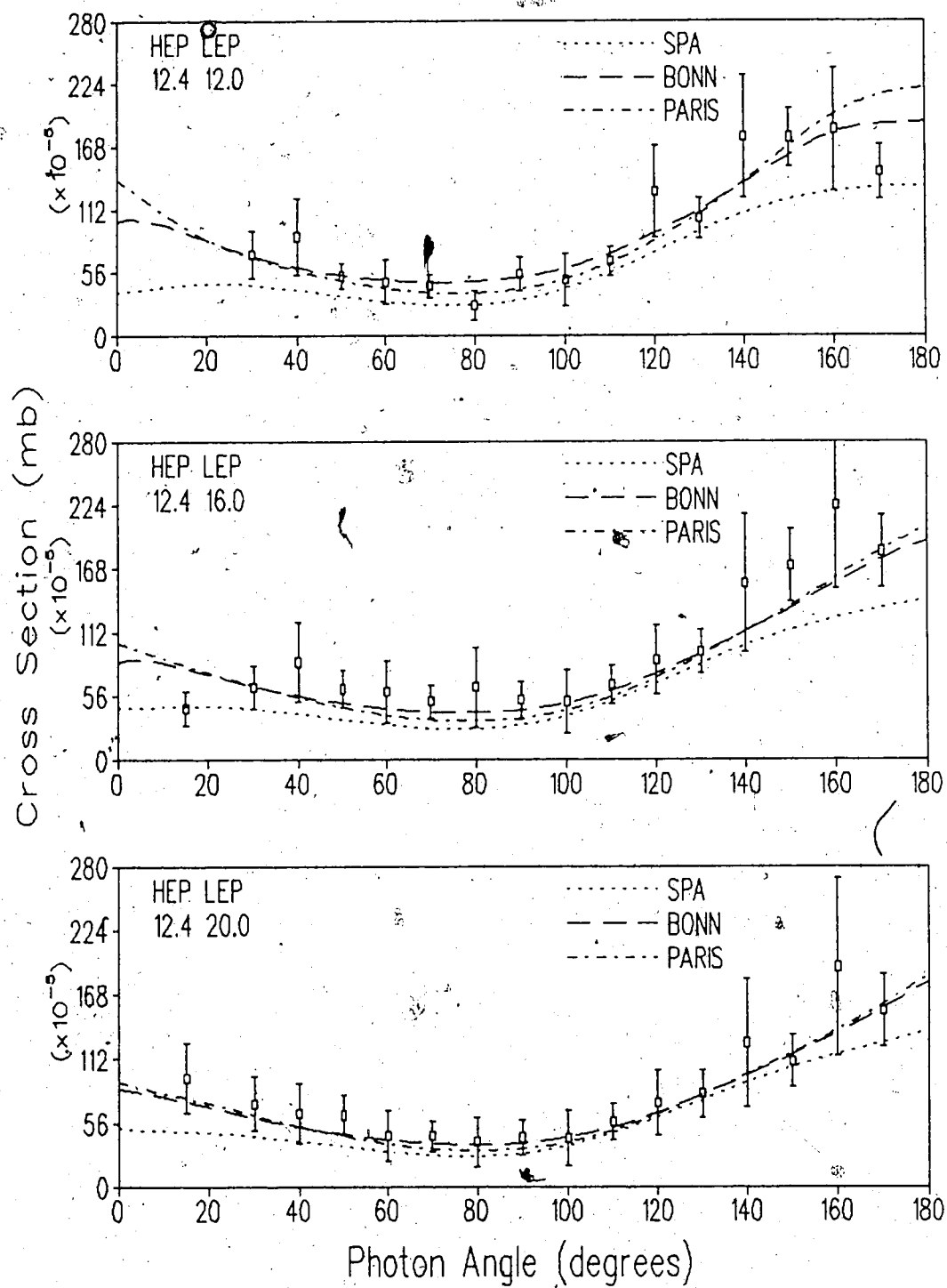


Figure 7.5: $pp\gamma$ cross sections for the small angle SAC. The data is arbitrarily normalized by multiplying by a factor of 0.667.

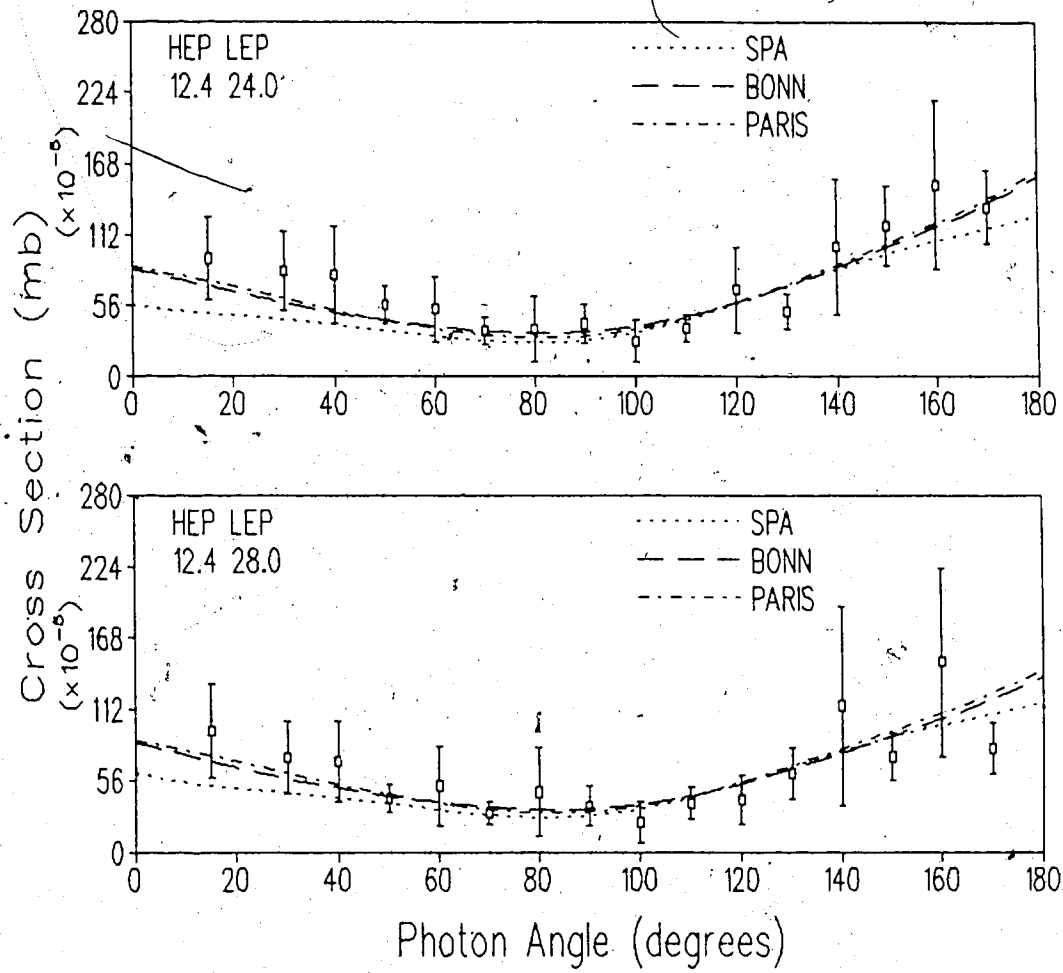


Figure 7.6: $pp\gamma$ cross sections for the small angle SAC. The data is arbitrarily normalized by multiplying by a factor of 0.667.

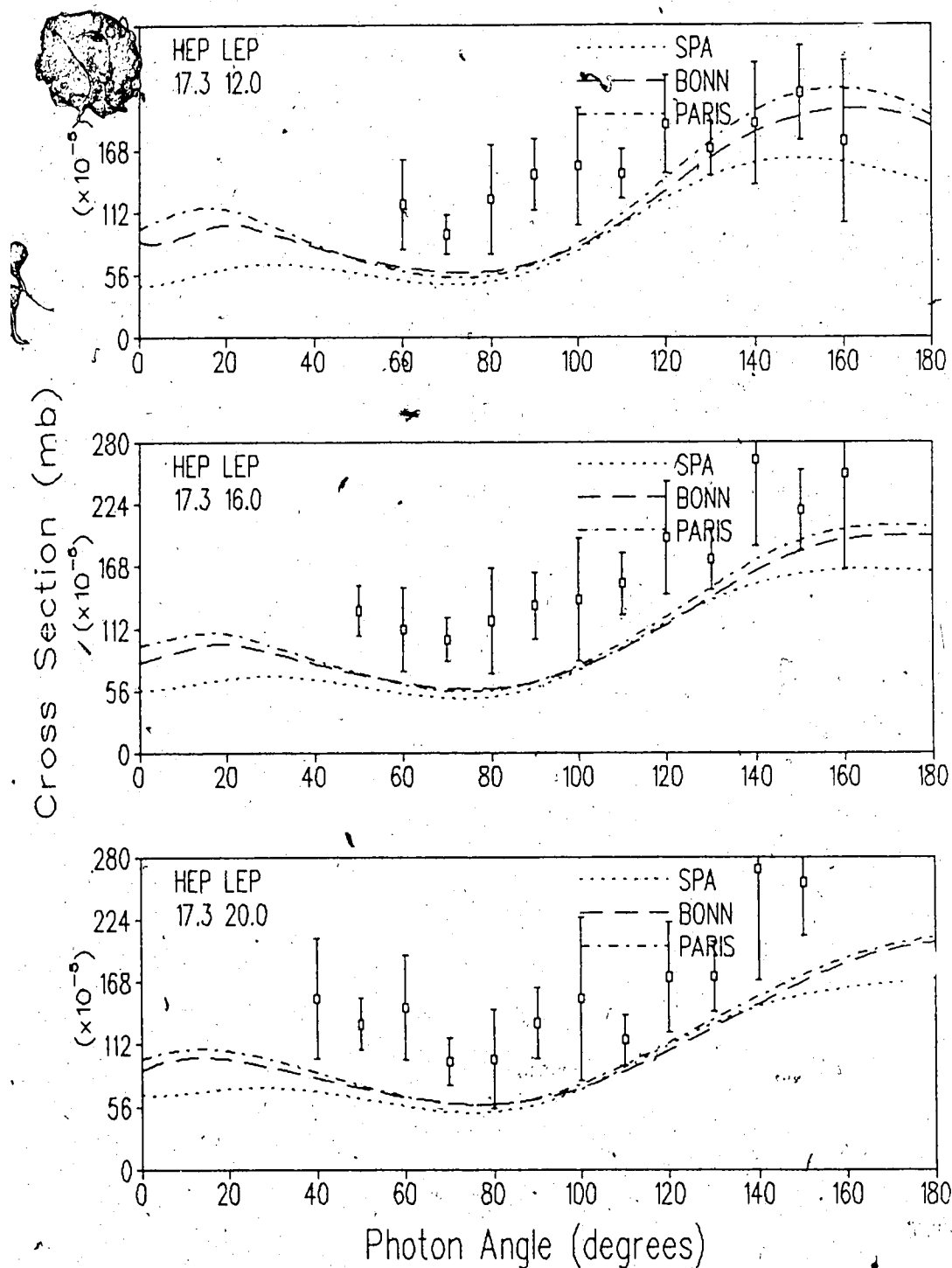


Figure 7.7: $pp\gamma$ cross sections for the large angle SAC. The data is arbitrarily normalized by multiplying by a factor of 0.667.

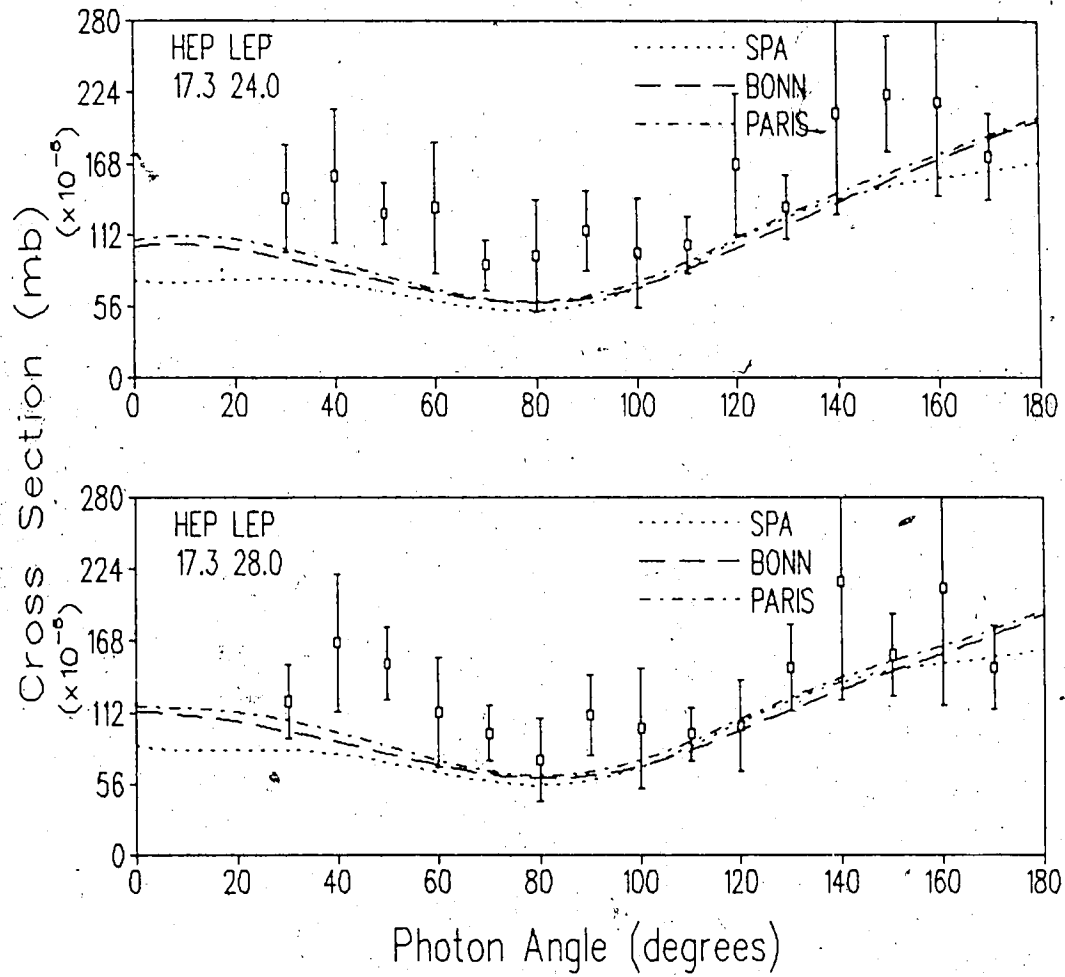


Figure 7.8: $pp\gamma$ cross sections for the large angle SAC. The data is arbitrarily normalized by multiplying by a factor of 0.667.

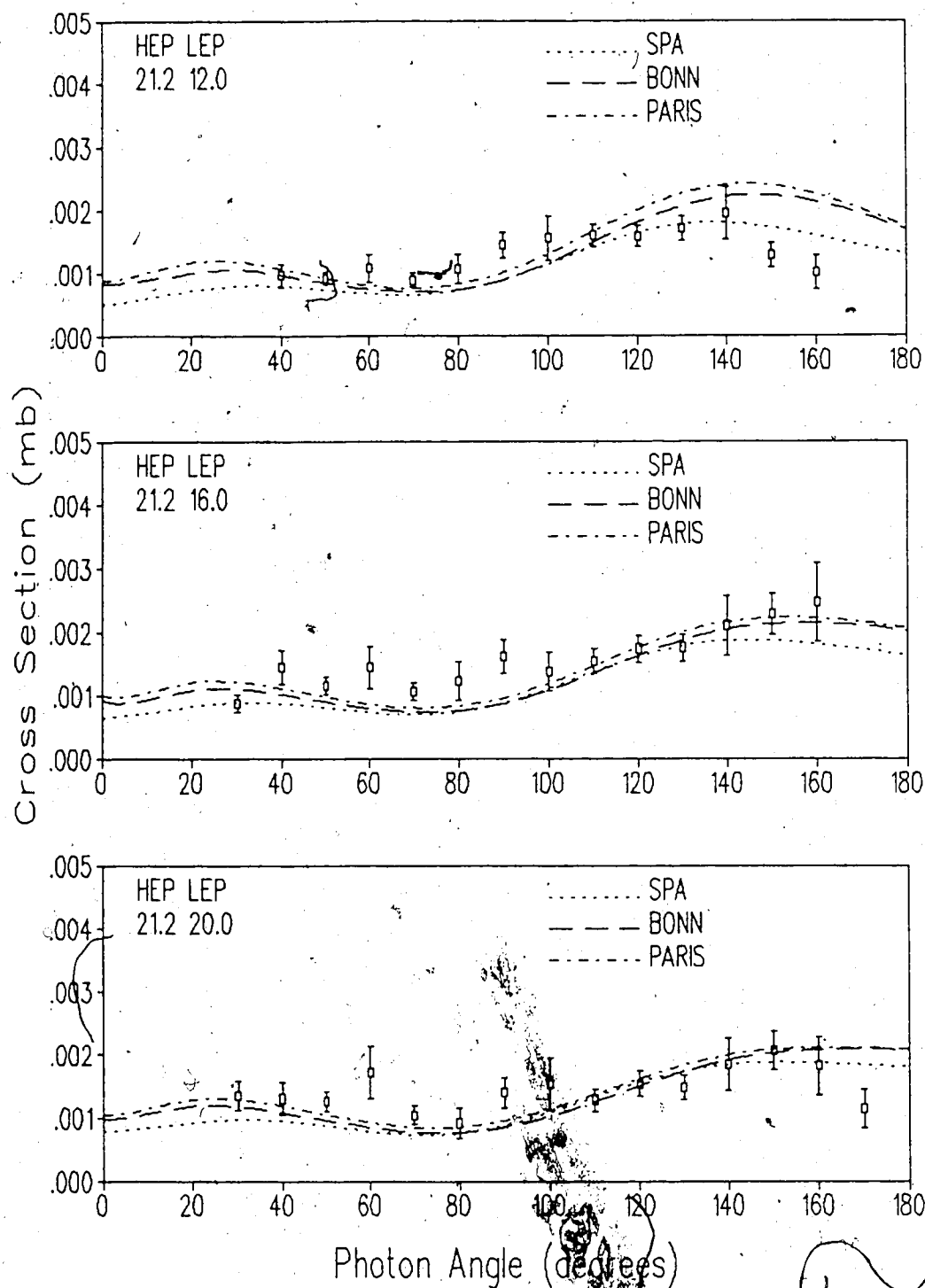


Figure 7.9: $pp\gamma$ cross sections for the small angle LAC. The data is arbitrarily normalized by multiplying by a factor of 0.667.

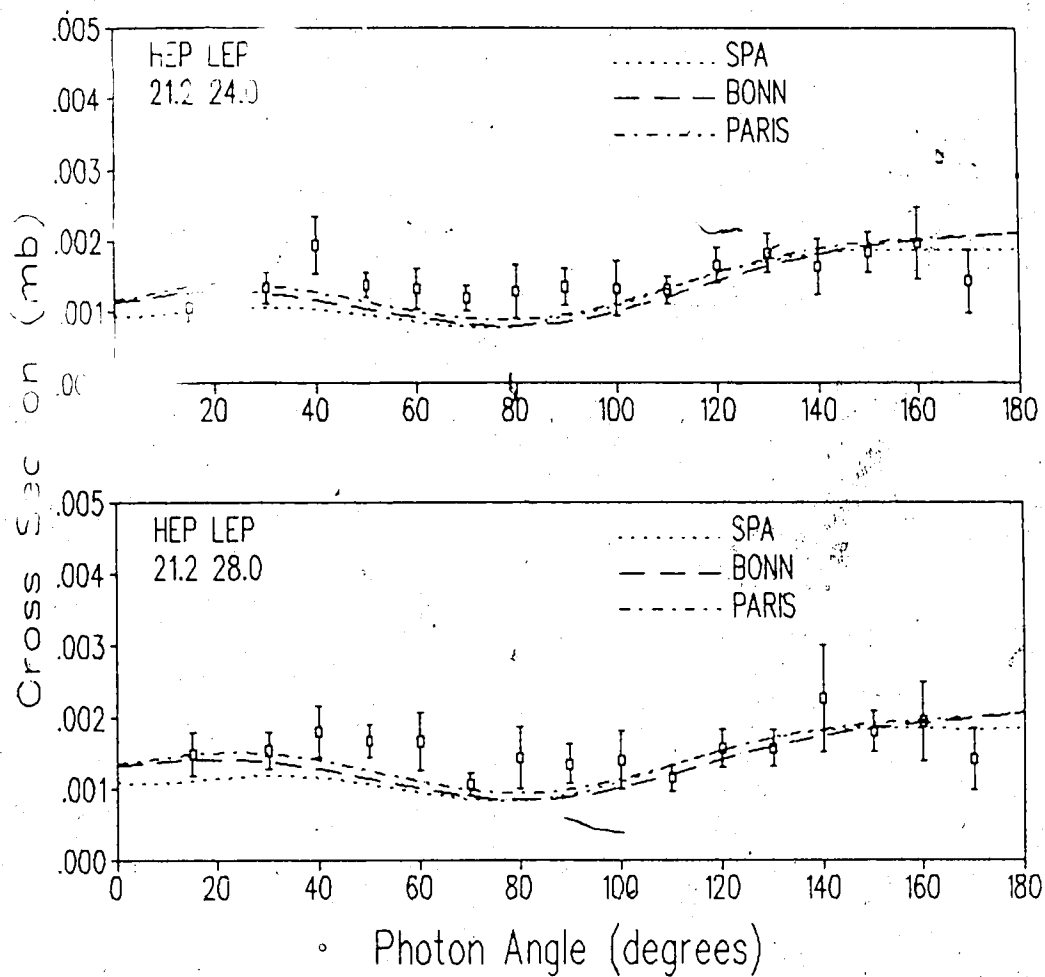


Figure 7.10: $\gamma\gamma$ cross sections for the small angle LAC. The data is arbitrarily normalized by multiplying by a factor of 0.667.

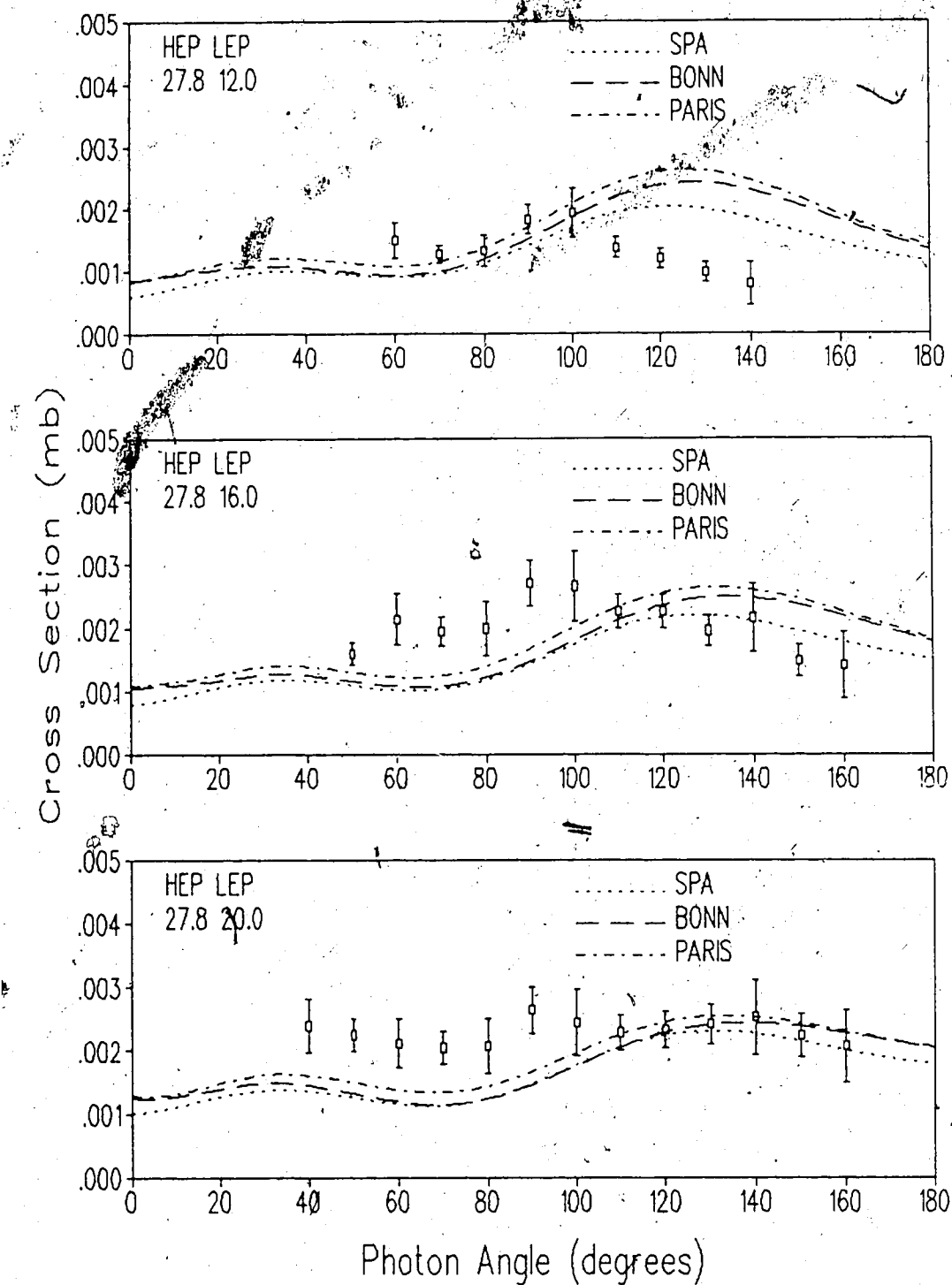


Figure 7.11: $pp\gamma$ cross sections for the large angle LAC. The data is arbitrarily normalized by multiplying by a factor of 0.667.

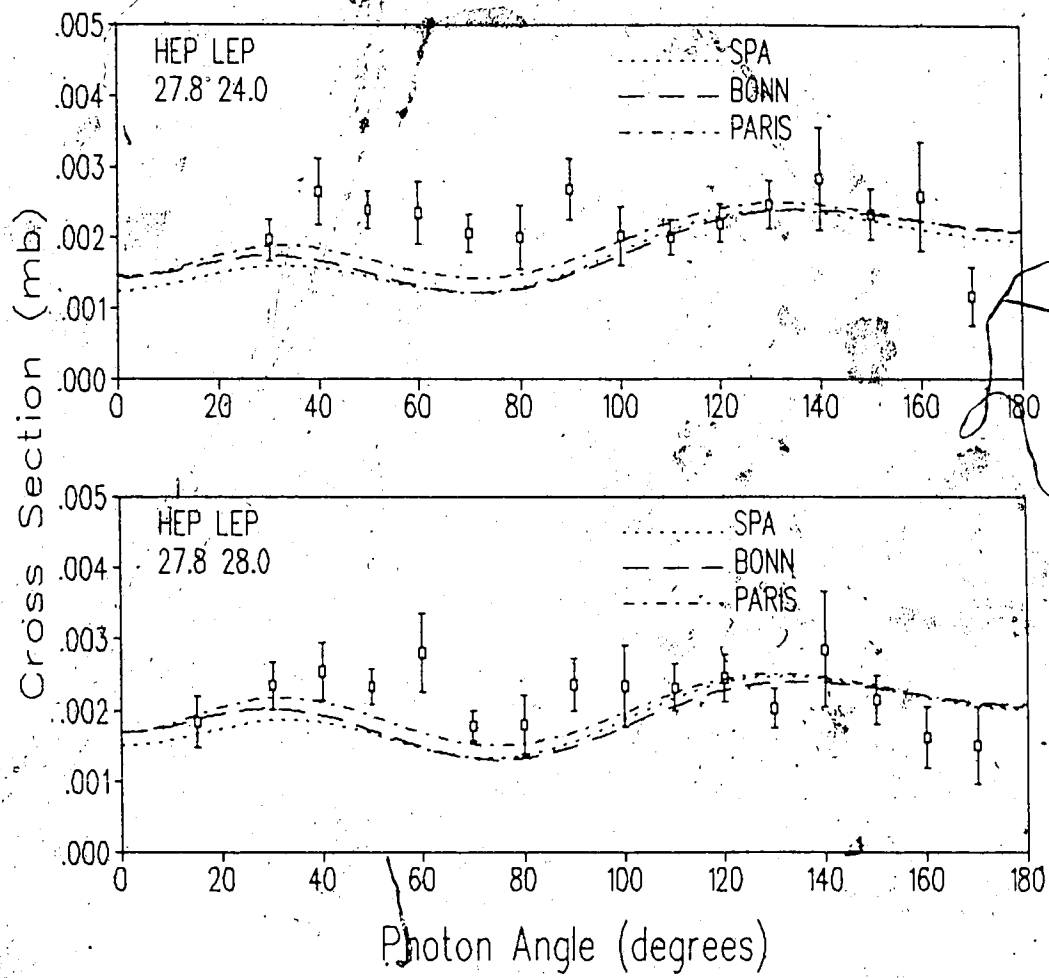


Figure 7.12: $pp\gamma$ cross sections for the large angle LAC. The data is arbitrarily normalized by multiplying by a factor of 0.667.

2. complete absorption of lower energy HE protons before they reached the trigger counters,
3. lower energy HE protons being bent into the end 20 cm region of the HE detector array. Detection of these events will be very sensitive to the amount of energy-degrading material before the C-magnet.

As with the analysing powers, the theoretical cross section curves have been averaged (with a cross section weight), over 4 coplanar points within the HE and LE bins. The errors introduced by this averaging are listed in tables 7.1 and 7.2 for the bins plotted. In general these errors are much smaller than the statistical errors of the data, except at largest photon scattering angles.

Appendix F contains an estimation of the systematic errors and appendix G contains a listing of the numerical values of the analysing powers, the cross sections, and their statistical errors.

Chapter 8

Results and Conclusions

8.1 Results; Asymmetries and Cross Sections

The χ^2 of the measured asymmetries with respect to the Bonn and Paris potential calculations, as well as the SPA are listed in table 8.1. The asymmetry results leave no doubt that the potential models give a more accurate description of the $pp\gamma$ interaction than does the SPA. This is in contrast to the conclusions of most prior bremsstrahlung experiments. Reference [26] contains a summary of some of these. Near on-shell, our results are consistent with both the potential models and the SPA which predict small analysing powers. Going further off-shell, our results follow the potential models which diverge from the SPA.

The measured cross sections, as normalized to the elastic results (appendix C), are consistently larger than the predicted values. Reasonable normalization to the theory is obtained if the data is multiplied by a factor

SAC HEP Angle = 12.4°			
LEP Angle	SPA	BONN	PARIS
14.0	10.804	0.845	1.282
22.0	5.566	0.986	1.743
28.0	1.272	1.545	1.393
SAC HEP Angle = 17.3°			
LEP Angle	SPA	BONN	PARIS
14.0	8.078	2.429	2.352
22.0	6.308	2.056	2.078
28.0	2.203	1.272	1.352
LAC HEP Angle = 21.2°			
LEP Angle	SPA	BONN	PARIS
14.0	4.191	1.814	1.842
22.0	2.272	1.549	1.329
28.0	1.498	1.108	1.052
LAC HEP Angle = 27.8°			
LEP Angle	SPA	BONN	PARIS
14.0	1.998	0.782	0.950
22.0	3.264	2.219	2.448
28.0	2.584	1.860	1.983

Table 8.1: χ^2 values per data point for the asymmetry plots of Chapter 7.

Each plot contains 16 data points.

of 0.667. This discrepancy is larger than the estimated systematic error of 17% (appendix F). Although very exhaustive checks on the data acquisition, analysis procedure, and Monte Carlo failed to uncover an error, we do not rule out this possibility. It should be noted however, that the theoretical calculations of Fearing et al. do not include double scattering or momentum dependent terms. The only calculation of these terms to date are those by Brown [17] at 158 MeV which indicate a contribution to the cross section of $\sim 15\%$. The terms are expected to contribute more as the incident proton energy increases.

8.2 Conclusion

The important physics that has come out of this experiment is first, a direct observation of the off-shell nature of the nuclear force has been made. Secondly, contrary to the conclusions of prior $pp\gamma$ experiments, potential model calculations are, as theoretically anticipated, far better at predicting the off-shell nature of the interaction $p + p \rightarrow p + p + \gamma$ than is the SPA. This experiment rules out any significant cancellation of the off-shell terms. It is suggested that the better agreement of most of the earlier experiments with the SPA has been a result of the inherent difficulties in normalizing experimental absolute cross sections. More faith can be put in the results of the present experiment for two reasons. First, statistics have been improved by an order of magnitude over the best of the earlier experiments. Secondly, analysing powers were measured, and these do not involve the normalization

difficulties of the cross sections.

Although the χ^2 values tend to favor the Bonn potential, it would perhaps be too bold to suggest this experiment could select the most appropriate existing potential for the nuclear force. The statistical errors are, in most bins, larger than the differences between the Paris and Bonn potentials in both the cross sections and the analysing powers. The kinematics of this experiment meant we were studying the reaction at off-shell momenta between 1.0 and 2.5 fm⁻¹ where the P-wave amplitude is more important. Calculations show that the Bonn and Paris potentials differ most in S-wave off-shell behavior, but here however, the off-shell effects are in general smaller.

A more definitive statement on the appropriateness of various potential models will require first a theoretical determination of regions where the modern potentials differ significantly in their off-shell behavior to make another pp γ experiment statistically feasible. Already, such proposals are being pursued by members of our group.

Bibliography

- [1] M. K. Srivastava and Donald W. L. Sprung. Off-shell behavior of the nucleon-nucleon interaction. In J.W. Negele and E. Vogt, editors, *Advances in Nuclear Physics*, chapter 2, Plenum Press, New York, 1980.
- [2] M. L. Halbert. In S.M. Austin and G.M. Crawley, editors, *The Two Body Force in Nuclei*, Plenum Press, New York, 1972.
- [3] J.V. Jovanovich, L.G. Greeniaus, J. McKeown, T.W. Miller, D.G. Peterson, W.F. Prickett, K.F. Suen, and J.C. Thompson. *Phys. Rev. Lett.*, 26:277, 1971.
- [4] L.G. Greeniaus, J.V. Jovanovich, R. Kerchner, T.W. Miller, C.A. Smith, and K.F. Suen. *Phys. Rev. Lett.*, 35:696, 1975.
- [5] J.V. Jovanovich, C.A. Smith, and L.G. Greeniaus. *Phys. Rev. Lett.*, 37:631, 1976.
- [6] B.M.K. Nefkens, O.R. Sander, and D.I. Sober. *Phys. Rev. Lett.*, 38:876, 1977.
- [7] J.G. Rogers, J.L. Beveridge, D.P. Gard, H.W. Fearing, A.N. Anderson,

- J.M. Cameron, L.G. Greeniaus, C.A. Goulding, C.A. Smith, A.W. Stetz, J.R. Richardson, and R. Frascaria. *Phys. Rev.*, C22:2512, 1980.
- [8] R. W. Workman. *A Modern Potential Model Calculation of Proton-Proton Bremsstrahlung*. Master's thesis, University of British Columbia, 1984.
- [9] R.L. Workman and Harold W. Fearing. *Phys. Rev.*, C34:780, 1986.
- [10] M. Sobel and A. Cromer. *Phys. Rev.*, 132:2698, 1963.
- [11] B. Gottschalk, W. Schlaer, and K. Wang. *Nuclear Physics*, 75:549, 1966.
- [12] R. E. Warner. *Phys. Lett.*, 18:289, 1965.
- [13] I. Slaus, J. W. Verba, J. R. Richardson, R. F. Carlson, W. T. H. van Oers, and L. S. August. *Phys. Rev. Lett.*, 17:536, 1966.
- [14] J. Thompson, S. Naqvi, and R. Warner. *Phys. Rev.*, 156:1156, 1967.
- [15] I. Duck and W. A. Pearce. *Phys. Lett.*, 21:669, 1966.
- [16] *Proc. Int. Conf. on Light Nuclei, Few Body Problems, and Nuclear Forces*, Brela, Yugoslavia, July 1967.
- [17] V. Brown. *Phys. Lett.*, 25B:506, 1967.
- [18] Private communication with H. W. Fearing.
- [19] M. K. Liou and M. I. Sobel. *Annals of Physics*, 72:323-352, 1972.
- [20] J.D. Bjorken and S.D. Drell. *Relativistic Quantum Mechanics*. International Series in Pure and Applied Physics, McGraw Hill, 1964.

- [21] R. Vinh Mau. *Mesons in Nuclei*, page 151. Volume 4, North-Holland Publishing, 1979.
- [22] M.H. MacGregor, R.A. Arndt, and R.M. Wright. *Phys. Rev.*, 182:1714, 1969.
- [23] R. Machleidt, K. Holinde, and Ch. Elster. *Phys. Repts.*, 149, May 1986.
- [24] R. Machleidt. Nuclear forces within a consistent meson-exchange model. In *Symposium on Quarks and Nuclear Structure*, Bad Honnef, W. Germany, June 1983.
- [25] F. E. Low. *Phys. Rev.*, 110:974, 1958.
- [26] H. W. Fearing. Some comments on the soft-photon approach to proton-proton bremsstrahlung. In *International Conference on the Nucleon-Nucleon Interaction*, TRIUMF, Vancouver, B.C. Canada, July 1977.
- [27] H. Feshbach and D.R. Yennie. *Nucl. Phys.*, 37:150, 1962.
- [28] T.H. Burnett and N.M. Kroll. *Phys. Rev. Lett.*, 20:86, 1968.
- [29] H.W. Fearing. *Phys. Rev.*, D7:243, 1973.
- [30] K.W. Ehlers. *Nucl. Instr. & Meth.*, 32:309, 1965.
- [31] B.L. Donnally. In H.H. Barschall and W. Haeberli, editors; *Proc. 3rd International Symposium on Polarization Phenomena in Nuclear Reactions*, page 295, 1971.

- [32] An event analysis program used at the University of Alberta, written by L.G. Greeniaus and obtained through private communication.
- [33] A.R. Mortimer and J.R. Stokoe. *A Liquid Hydrogen or Deuterium Target System with Closed Cycle Refrigeration*. report 237, Rutherford Laboratory, 1971.
- [34] An event acquisition program used at the University of Alberta, written by P.W. Green and obtained through private communication.
- [35] M. Gell-Mann and M.L. Goldberger. *Phys. Rev.*, 91:398, 1953.

Appendix A

Cerenkov Detector Efficiencies

Photon detection efficiencies required for cross section normalization were calculated with a separate Monte Carlo code, EGS, and then incorporated into the larger Monte Carlo that simulated the entire experiment. The objective was to determine an integrated efficiency over the face of the counter for detection of photons, given an initial photon energy, intervening absorbing material between the target and detector, the geometry of the Pb glass, and the threshold of the discriminator.

A diagram of the inside of the scattering chamber and the intervening photon absorbing material is given in figure 4.3. A listing of absorber thickness, representing an integrated average over the detector solid angle, is given in tables A.1 and A.2.

Tables of photon energy loss for the various interaction processes (photo electric effect, compton scattering, and pair production) were supplied as input to the code for all absorber materials except Teflon (CF_2), for which

C#	target flange (steel)	target cylinder (steel)	LE detector (NE110)	Teflon absorber (AL equiv.)	Chamber wall (AL)	CH ₂ absorber (CH ₂)
1	0	0	.611	0	1.27	11.048
2	0	0	.350	1.34	1.29	11.190
3	0	0	0	4.01	2.13	0
4	0	0	0	3.50	3.08	0
5	0	.092	0	2.87	1.99	0
6	0	.085	0	2.46	1.68	0
7	1.69	0	0	3.67	1.47	0
8	2.69	0	0	4.96	2.12	0
9	1.69	0	0	5.04	2.02	0
10	0	.085	0	5.30	.716	0
11	0	.092	0	5.74	.730	0
12	.423	.105	0	7.00	.764	0
13	.500	.124	0	8.29	.826	0
14	0	.164	0	9.86	.942	0
15	0	.252	0	9.36	1.12	0
16	0	.649	0	8.49	1.95	0

Table A.1: Photon absorber thicknesses intervening between target and Pb glass detectors. Units of cm.

C ^ν #	LE veto (NE110)	C ^ν veto (NE110)	mag. shield (steel)
1	.641	.320	.079
2	.320	.320	.079
3	0	.320	.079
4	0	.320	.079
5	0	.320	.079
6	0	.320	.079
7	0	.320	.079
8	0	.320	.079
9	0	.320	.079
10	0	.320	.079
11	0	.320	.079
12	0	.320	.079
13	0	.320	.079
14	0	.320	.079
15	0	.320	.079
16	0	.320	.079

Table A.2: More photon absorber thicknesses intervening between target and Pb glass detectors. Units of cm.

tables were not available. Instead of Teflon, an appropriate thickness of aluminum was substituted. This thickness was estimated from the ratio of the mass attenuation coefficients for aluminum and Teflon. The validity of such an approximation was tested by comparing the code results using both iron and aluminum substitutes for Teflon. Agreement was found to within the statistical errors of the initial 3000 photon sample.

Events were generated from a point source at the target, uniformly and randomly into the solid angle subtended by the counters. The photons were then tracked through the absorber, taking account of direction changes and energy degradation arising from the photon interaction mechanisms. For each detector, two runs were made, one at the minimum of the kinematic photon energy limit, and the other at the maximum. The actual three dimensional geometry of the Pb glass was input. If the resultant energy deposited within the Pb glass was below a 20 MeV threshold (due to non-interacting photons, electron showers leaving the glass at the edges, or loss of photon energy within the absorber), the event was not counted. Also, if the energy deposited within the 3.18 mm thick plastic charged particle veto, in front of each Pb glass detector, by pair produced or Compton scattered minimum ionizing electrons, was above the 0.5 MeV threshold of the veto, the event was not counted. Figure A.1 shows the distribution of electron energy deposited within the veto counters. The peaks correspond to one, two, or three minimum ionizing electrons.

The efficiency of the glass, for a particular incident photon energy, was obtained as the ratio of the number of photons with over 20 MeV deposited

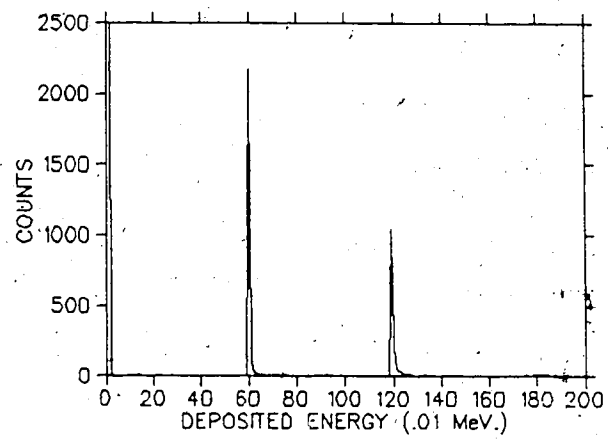


Figure A.1: Distribution of electron deposited energy within the cerenkov veto counters. The peaks correspond to one or two minimum ionizing electrons.

within the Pb glass and less than 0.5 MeV deposited within the veto counter, over the number of photons in sample (= 3000). Tables A.3 and A.4 show the efficiencies of the cerenkov detectors at the average photon energy of the bin.

C _ν	Angle (degrees)	Avg. Energy (MeV)	Efficiency
1	15	158	.712
2	30	148	.649
3	40	136	.616
4	50	124	.587
5	60	116	.645
6	70	108	.648
7	80	99	.636
8	90	92	.422
9	100	88	.558
10	110	82	.578
11	120	79	.556
12	130	76	.506
13	140	71	.462
14	150	68	.417
15	160	67	.418
16	170	66	.372

Table A.3: Photon detection efficiencies in the LAC.

C _v	Angle (degrees)	Avg. Energy (MeV)	Efficiency
1	15	155	.704
2	30	134	.646
3	40	122	.620
4	50	111	.575
5	60	101	.644
6	70	94	.636
7	80	88	.623
8	90	83	.416
9	100	81	.548
10	110	78	.564
11	120	75	.564
12	130	72	.491
13	140	71	.464
14	150	72	.414
15	160	72	.424
16	170	72	.376

Table A.4. Photon detection efficiencies in the SAC.

Appendix B

Target Empty and Target Vacuum Runs

Periodically throughout the main data taking runs, the liquid hydrogen target was emptied by closing the filler tube and allowing H_2 gas to boil off and escape as the target heated. Although it was assumed adequate time was given between closing the filler tube and starting a target empty run, no guarantees could be given that only H_2 gas remained. Also the density of the gas did not remain constant during the run but decreased as the target warmed up. The 3-coincidence events collected in such runs could therefore be attributed in some part to the real $pp\gamma$ events coming from the remaining hydrogen and in some part to the random background associated with the walls of the target. The relative contribution of these two components could not be determined just from the target empty data alone. This data did however serve as a consistency check between the elastic data used for cross section normalization and the real bremsstrahlung 3-coincidence data.

To determine the background attributed solely to the target walls, a completely evacuated target run was taken, with the target at room temperature, after completion of the LAC data taking. This procedure could only be done at the end of a run segment because of the time required to bring the temperature of the hydrogen down to the liquid state. Unfortunately because of an earlier than anticipated stop of the beam, no target vacuum data was taken in the SAC. There is however, little reason to suspect that the LAC and SAC target backgrounds would be different.

The target empty and target vacuum data were analysed using the same algorithms used for the target full data for both the 3-coincidence and HE P/S elastic events, (see section 5.3). The number of real and random events were counted for all bins and spin states and added together to provide adequate statistics for target empty, and vacuum data. A number of corrections were applied to the target full, empty, and vacuum counts. These corrections were for,

1. n_{inc} , number of incident protons obtained from SEM counts, normalized to 1 for target full data,
2. DT, dead time correction obtained from the pulser events and weighted by the SEM counts for a particular spin state.
3. MISS, a VDC missings correction obtained from the 3% events. This value was found to be relatively independent of spin and similar for the different target state runs.
4. MUL, a VDC multiples correction, weighted for spin via SEM values

(different spin states had different currents).

A listing of these corrections and the 3-coincidence counts, before and after the corrections, is given in table B.1. The ratio of the total corrected counts for target empty and target vacuum over target full data, is for the LAC,

$$\begin{aligned} \text{Total Counts} \frac{\text{Empty}}{\text{Full}} &= 5.29 \pm .24\% \\ \frac{\text{Vacuum}}{\text{Full}} &= 0.48 \pm .10\% \end{aligned}$$

and for the SAC,

$$\text{Total Counts} \frac{\text{Empty}}{\text{Full}} = 12.01 \pm .60\%$$

(No vacuum/full data was taken.) The difference between the SAC and LAC empty/full ratios is attributed partly to the difference in target emptying procedure for the two configurations and partly because more gas is viewed from the smaller angles of the SAC. A vacuum to full ratio of less than 0.5% implies that the target walls contributed an insignificant amount to the real 3-coincidence events.

For the HE P/S elastic data the ratio of target empty to target full and target vacuum to full was, in the LAC

$$\begin{aligned} \frac{\text{Empty}}{\text{Full}} &= 6.96 \pm .23\% \\ \frac{\text{Vacuum}}{\text{Full}} &= 1.34 \pm .04\% \end{aligned}$$

and for the SAC,

$$\frac{\text{Empty}}{\text{Full}} = 15.36 \pm .42\%$$

From the scaler attached to the $HE \cdot HE VETO$ coincidence for the LAC,

$$\frac{Vacuum}{Full} = 1.70\%$$

in close agreement with that of the event by event data.

pp γ Data (LAC)							
Target	Reals	Randoms	n_{inc}	DT	MISS	MUL	Counts
Full	71838	729	1.00	1.226	1.534	1.354	181022 \pm 679
Empty	522	26	10.20	1.058	1.534	1.166	9569 \pm 430
Vacuum	53	32	17.81	1.314	1.534	1.156	871 \pm 190
pp γ Data (SAC)							
Full	52044	841	1.00	1.255	1.572	1.358	137244 \pm 606
Empty	433	31	19.45	1.102	1.572	1.217	16489 \pm 822

Table B.1: Corrections to the target empty and vacuum data. The column labeled 'Counts' represents the real events after subtraction of the randoms and application of all corrections.

Appendix C

PP Elastic Analysis

A sample of pp elastic events was taken simultaneously along with the 3-coincidence events to provide a normalization for the $pp\gamma$ cross sections and to serve as a check on the polarization of the incident beam.

The trigger for these events was HEP detector #4 (fourth from the beam line of the 8 scintillators and roughly in the middle of the array) in coincidence with its veto behind the copper degrader. If the pulse heights from the scintillators, at the discriminators, were above a 30mV threshold, a coincidence was formed by an LRS 622 unit. Because of the high elastic cross section in comparison to that for bremsstrahlung, a prescaler selected only one in every 2^{15} coincidences to set the master gate (see figure 4.8).

The data words for the event consisted of VDC TDC values for each struck wire along the track of the proton, for each VDC anode plane. The common start for these TDC's was the detection of the proton at HE trigger scintillator # 4, and the stops were the detection of the ionized electrons at

the anode sensing wires.

The analysis of the elastic events was significantly different from that of the pp events. No cuts were made during the on-line acquisition: all events went directly to tape. In the skimming, only VDC missing events were rejected except if the missing was only plane 2U or a missing at a dead wire. The number of rejected misses was recorded for each run. The event was considered a candidate for a good elastic if the DCR bit signaling an elastic coincidence was set at the event:

1. Was not a VDC missings.
2. Was not a multiple. (An attempt was first made to resolve these multiples through comparison of internal VDC angles, magnet axis projection, etc., see section 5.3.)
3. Had an angle of bend through the spectrometer of an elastic.
4. Had an event vertex within the liquid region (the same as cut 7, section 5.3, applied to the pp γ events).
5. Had a trajectory that passed through a 2X vs 2H solid angle cut on the anode planes of VDC2. (Bins were centered at 27.5° (LAC) and 16.5° (SAC).)

The analysing power for the elastics was determined from

$$A_v = \frac{N^1 MUL^1 MISS^1 / n_{inc}^1 LT^1 - N^1 MUL^1 MISS^1 / n_{inc}^1 LT^1}{P^1 N^1 MUL^1 MISS^1 / n_{inc}^1 LT^1 + P^1 N^1 MUL^1 MISS^1 / n_{inc}^1 LT^1}$$

Spin	Polarization	n_{inc}	HE P/S	LT	MUL	MISS
↑	.740	1.673×10^{16}	28917	.804	1.339	1.526
↓	.769	1.644×10^{16}	22009	.824	1.207	1.492
off	.044	7.024×10^{15}	10126	.774	1.289	1.544

Table C.1: Accumulated HE P/S events and correction factors for the LAC. The spin up and down polarizations have been corrected for the instrumental asymmetry of the polarimeter.

where $N^{(1)}$ is the number of good elastic events acquired in the spin up(down) modes and $n_{inc}^{(1)}$ is the number of incident protons, determined from the number of SEM counts (section 7.1). $LT^{(1)}$ is the system live time obtained from the ratio of the the number of pulser events acquired on tape over the number of pulsers submitted, as recorded by scalers. The multiples $MUL^{(1)}$ and missings $MISS^{(1)}$ corrections were determined in the same manner as those for the $pp\gamma$ events, section 6.6. The polarization of the incident beam $P^{(1)}$ was obtained from the polarimeter scalers as defined in equation 7.1. Values of the number of good elastic events, the number of incident protons, the live time, multiples and missings corrections, and the beam polarization for the accumulated are given in tables C.1 and C.2 for the LAC and SAC respectively. An analysing power was determined for each run separately and then a statistically weighted average taken. Plots of the analysing power as

Spin	Polarization	n_{inc}	HE P/S	LT	MUL	MISS
↑	.790	2.140×10^{16}	41308	.799	1.331	1.458
↓	.744	2.221×10^{16}	26116	.802	1.219	1.389
off	.034	6.346×10^{15}	10203	.799	1.265	1.457

Table C.2: Accumulated HE P/S events and correction factors for the SAC. The spin up and down polarizations have been corrected for the instrumental asymmetry of the polarimeter.

a function of run number are given in figures C.1 and C.2. The statistically weighted averages are 0.269 ± 0.006 (LAC) and 0.410 ± 0.006 (SAC). The expected values at the bin centers are 0.285 (LAC) and 0.394 (SAC). The elastic cross sections were determined from,

for the polarized data

$$\left. \frac{d\sigma}{d\Omega_{HE}} \right|_{\uparrow\downarrow} = \frac{Z}{P^{\uparrow} + P^{\downarrow}} \left[\frac{P^{\uparrow} N^{\uparrow} MUL^{\uparrow} MISS^{\uparrow}}{n_{inc}^{\uparrow} LT^{\uparrow}} + \frac{P^{\downarrow} N^{\downarrow} MUL^{\downarrow} MISS^{\downarrow}}{n_{inc}^{\downarrow} LT^{\downarrow}} \right],$$

and for the incident beam unpolarized data

$$\left. \frac{d\sigma}{d\Omega_{HE}} \right|_0 = Z \left[\frac{N^0 MUL^0 MISS^0}{n_{inc}^0 LT^0} \right],$$

Here

$$Z = \frac{2^{15} R_{loss}}{n_{tgt} t \Omega_{HE}},$$

where the factor 2^{15} corrects for the prescaling. n_{tgt} is the number of target protons per unit volume, which for liquid hydrogen is $4.222 \times 10^{22}/cm^3$, and

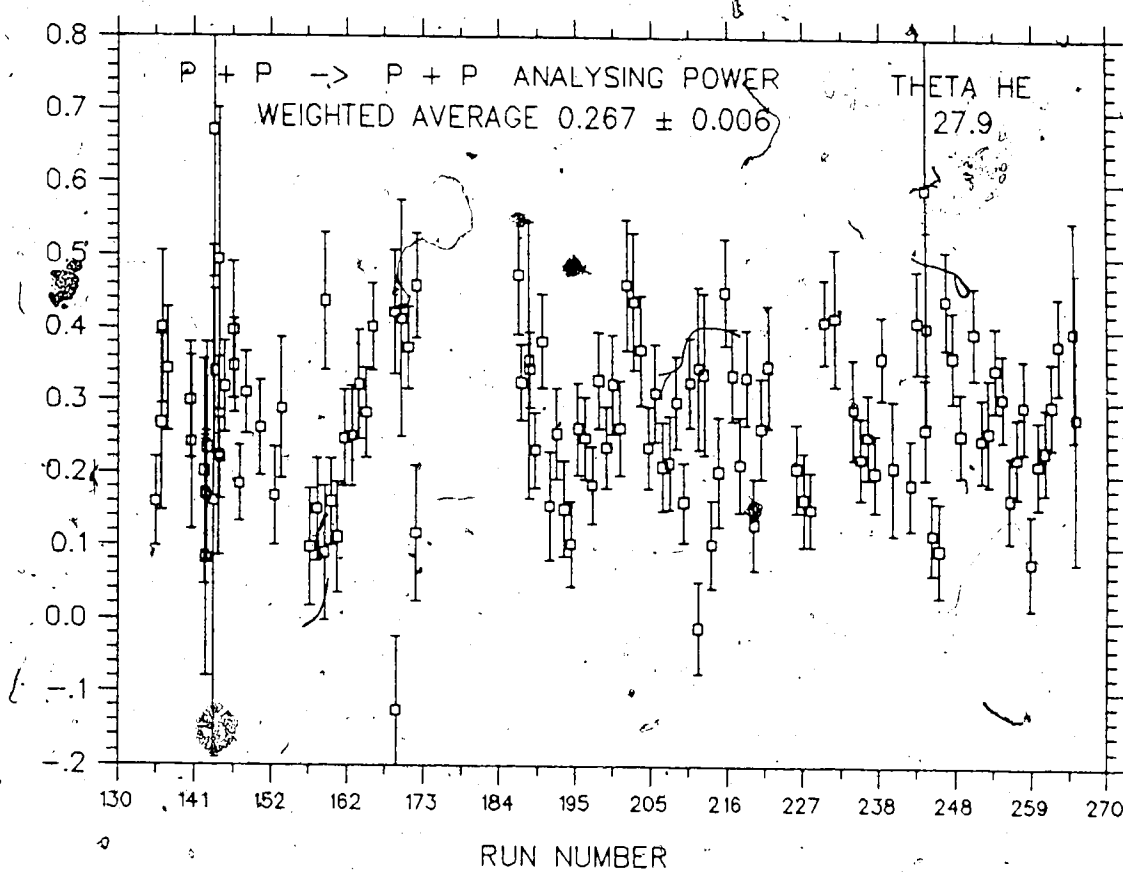


Figure C.1: FF P/S elastic analysing powers as a function of run number, or time, for the LAC.

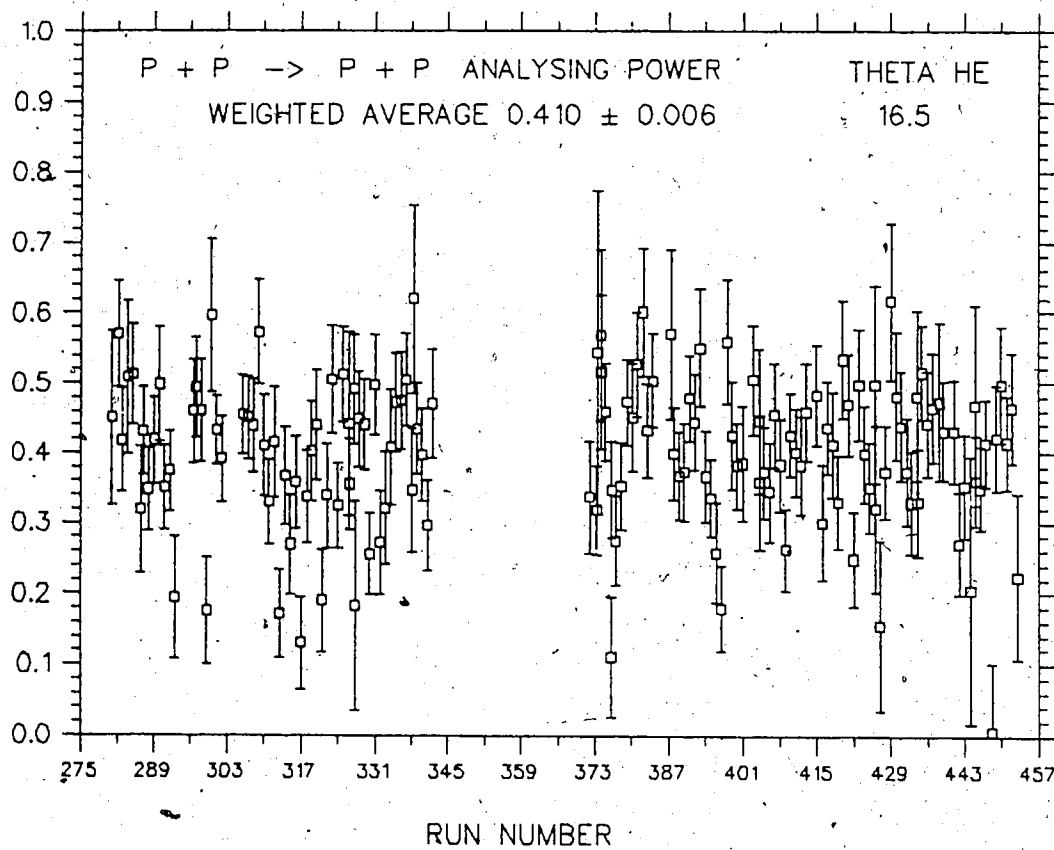


Figure C.2: HE P/S elastic analysing powers as a function of run number, or time, for the SAC.

t is the target thickness, nominally 0.500 cm. R_{loss} is a correction for elastic reaction losses in the Cu absorber between the HE4 trigger scintillator and its veto. Some of the elastics will undergo a nuclear reaction in the absorber and not be detected in the veto counter. However, of those that do undergo a nuclear reaction some will have their reaction products detected. The value of the correction, which depends on the thickness of the Cu absorber, the total reaction cross section and the range of the proton at the particular energy, was found to be 1.15 (LAC) and 1.17 (SAC). The solid angle Ω_{HE} was determined from the cut applied to the X and Y anode planes of VDC2 (actually Y was converted to a true vertical height H and the cut applied to X vs H). These were determined to be 0.594 msr (LAC) and 0.521 msr (SAC).

The total unpolarized cross sections were obtained by combining the unpolarized with the polarized data according to

$$\frac{d\sigma}{d\Omega_{HE}} = \frac{\sigma^{11}/(\delta\sigma^{11})^2 + \sigma^0/(\delta\sigma^0)^2}{1/(\delta\sigma^{11})^2 + 1/(\delta\sigma^0)^2},$$

where σ is short for $d\sigma/d\Omega_{HE}$ and $\delta\sigma$ is the statistical error.

Plots of the cross sections as a function of run number are given in figures C.3 and C.4. The statistically weighted averages and the expected values, assuming the nominal 0.500 cm thick target, at the bin centers are, respectively, 10.96 ± 0.04 (LAC), 12.31 ± 0.04 (SAC) and 14.22 (LAC), 15.88 (SAC). Data points far below the mean values are believed to be the results of runs taken while the target was still warm and perhaps boiling.

The $pp\gamma$ cross sections were normalized with respect to the elastic analysis

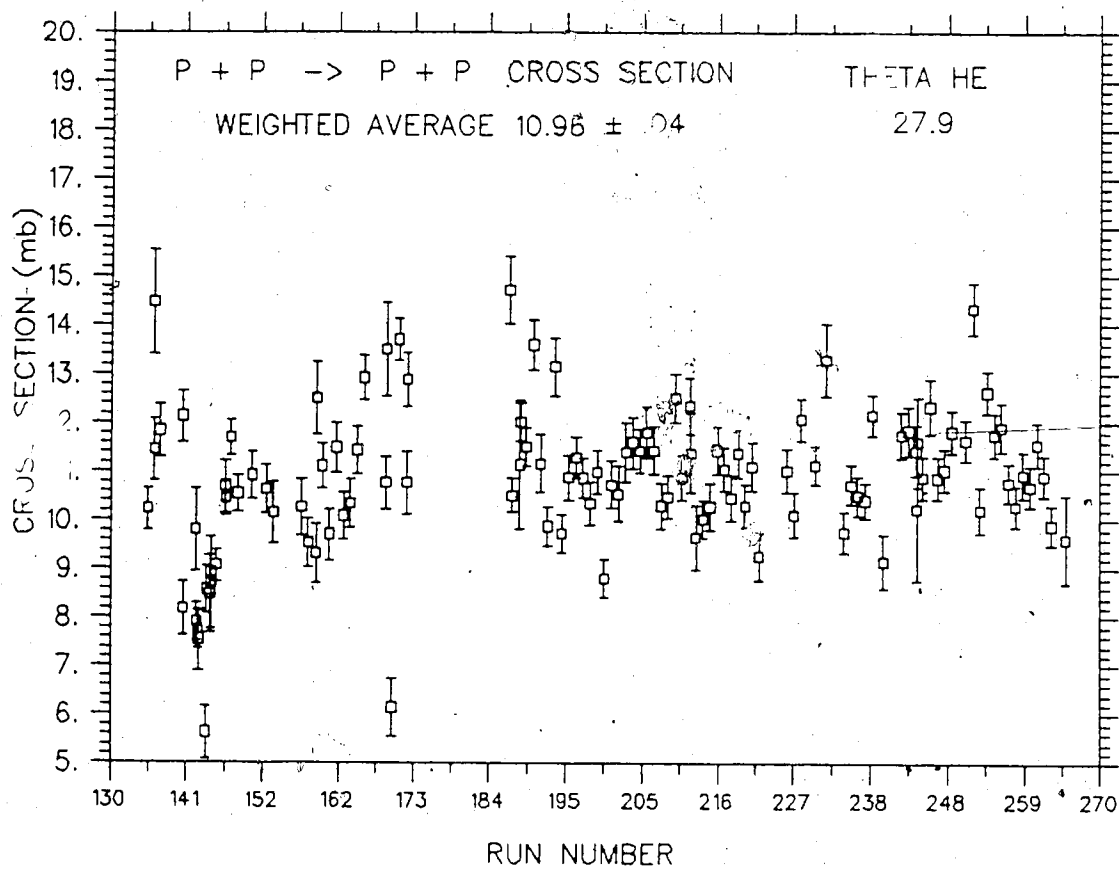


Figure C.3: HE P/S elastic cross sections as a function of run number, or time, for the LAC.

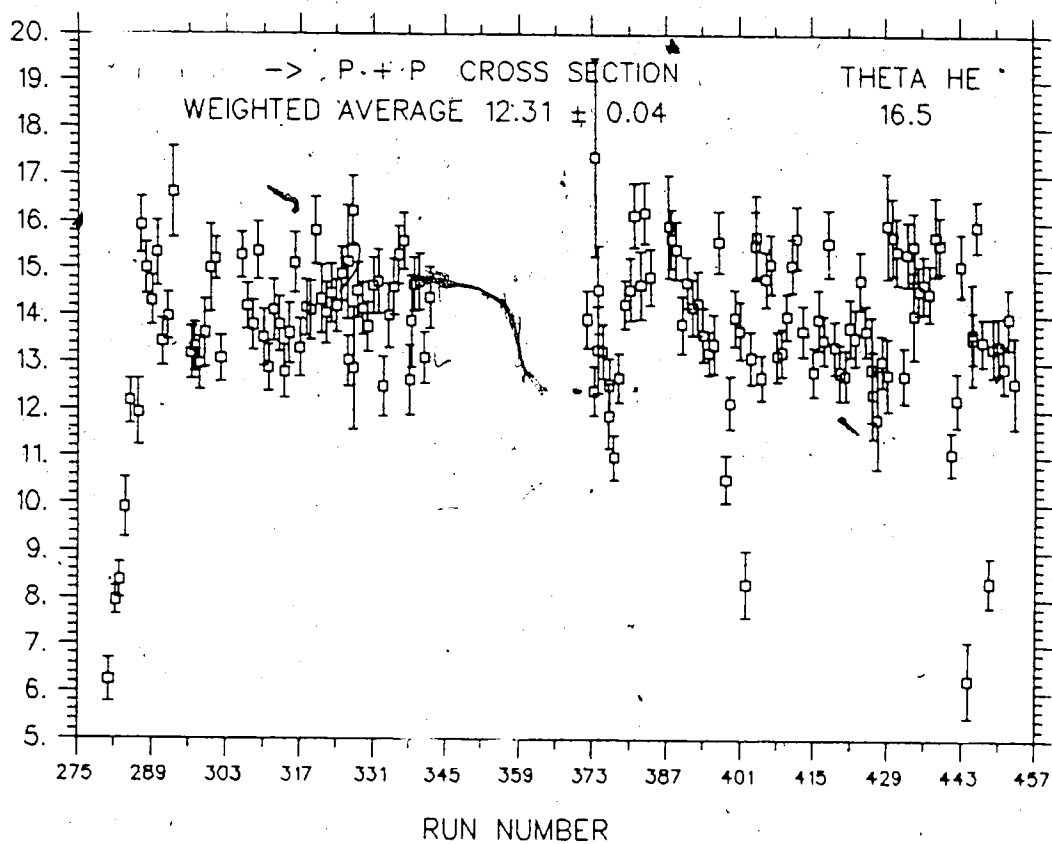


Figure () HE P/S elastic cross sections as a function of run number, or
 time, for the SAC.

by using the renormalized target thickness obtained from the ratio of the average elastic cross sections over the expected values times the nominal thickness of 0.500 cm. This gives, for the LAC,

$$0.500 \times \frac{10.96}{14.22} = 0.385 \text{ cm},$$

and for the SAC,

$$0.500 \times \frac{12.31}{15.88} = 0.388 \text{ cm}.$$

Appendix D

Potential Model Calculations of Fearing and Workman

Complete details of the bremsstrahlung calculation by Fearing and Workman are given in reference [8]. Here we give only a summary of the main ingredients that, when combined together, distinguish their calculation from older ones. It would be helpful to read chapter 2, describing a generic $pp\gamma$ calculation, before continuing.

The most important advance is the use of two modern potentials, the Paris and Bonn potentials, in their calculation. They obtain the invariant $pp\gamma$ amplitude, by using the non-relativistic Lippmann-Schwinger equation with its T-matrix form and the two-potential formalism of Gell-Mann and Goldberger[35]. The full Hamiltonian is $H_0 + V_{em} + V_N$, where H_0 is the free part, V_N is the strong N-N interaction treated to all orders, and V_{em} is the weak electromagnetic interaction taken to first order only. They arrive at an equation almost like equation 2.12 plus equation 2.18, representing

respectively single scattering and double scattering, but without the term coming from the momentum dependence of the nuclear potential. These momentum dependent and the double scattering terms are neglected in any case (see section 2.2.7). The calculation is however done in the CM so the effect of this neglect is minimized.

Relativistic kinematics are used throughout and relativistic spin corrections to the electromagnetic interaction are included. These corrections are equivalent to terms 4 and 5 of equation 2.9 which were obtained by Liou and Sobel[19] by applying a Foldy-Wouthuysen transformation, to third order in $\frac{K \cdot E \cdot p}{m_p}$, to the Dirac equation (see section 2.2.4).

The $p - p$ off-shell interaction matrix is obtained from both the Paris and Bonn potentials. They derive it, for each partial wave, by writing it as the product of the on-shell interaction matrix and a half-off-shell function F_l (equation 2.14). This is substituted into the partial wave momentum space Lippmann-Schwinger equation and solved for F_l . It should be noted here that the $1-\pi$ exchange amplitudes, important to the higher partial waves, are not dropped as they are in some older calculations. Coulomb corrections, to simulate interference between the strong and electromagnetic interactions, are next added to the half-off-shell NN amplitudes[8].

The corrected strong and electromagnetic vertex terms are combined through the two potential T-matrix formalism to give an equation like 2.15 for the single scattering terms of the $pp\gamma$ amplitude. No double scattering terms have yet been included by Fearing although an effort to do so is under way. Brown [17] has calculated the contribution from such terms to be $\sim 15\%$.

of the integrated cross section at 158 MeV.

The sensitivity of the cross sections and asymmetries to the inclusion of the various corrections is investigated by Workman [8]. In general the relativistic spin correction is found to be most important and the asymmetries are found to be much more sensitive than the cross sections over all.

Appendix E

Solid Angles Subtended by Detectors

This appendix summarizes the geometry of the particle detectors.

E.1 Low Energy Protons (LEP)

The LEP's were detected within the polar angles of 10.0° to 30.0° in five 4° bins. Two forward detectors, 6.24×8.46 cm high, were located 93.45 cm from the target. The other three, 6.98×9.46 cm high, were located 104.33 cm from the target. All detectors covered approximately $\pm 2.6^\circ$ out of the horizontal plane. The forward detectors subtended a solid angle at the target of 6.064 msr, while the backward detectors subtended a slightly larger solid angle of 6.086 msr.

E.2 High Energy Protons (HEP)

The HEP's were detected within polar angles of 9.9° to 31.0° . Data taking was divided into two configurations, the large angle configuration (LAC) covering 18.0° to 31.0° , and the small angle configuration (SAC) covering 9.9° to 19.8° . The solid angle for these protons was defined by a cut on the X and Y anode planes of drift chamber # 2. This allowed detection of protons that were approximately $\pm 1.4^\circ$ (LAC) and $\pm 1.2^\circ$ (SAC) out of the horizontal plane. Each configuration was divided into two bins. The polar angle ranges, central value, distances, and solid angles subtended by these four bins are listed in table E.1.

Configuration	Polar Angles degrees	Center degrees	Distance cm	Solid Angle msr
SAC	9.9 - 14.8	12.4	171.9	4.293
	14.8 - 19.8	17.3	154.4	4.543
LAC	18.0 - 24.5	21.2	136.7	7.179
	24.5 - 31.0	27.8	125.8	7.498

Table E.1: Polar angle ranges, central value, distances, and solid angles subtended by the four HEP bins.

E.3 Photon Detectors

The Pb glass detectors covered the polar angle range from about 13° to 172° in 16 bins: one for each detector. The $14.9\text{ cm} \times 14.9\text{ cm}$ cubes detected photons to approximately $\pm 5.4^\circ$ out of the horizontal plane while the 12.7 cm diameter cylinders detected them to about $\pm 2.9^\circ$. Tables E.2 and E.3 give the detector type, central angle, distance from the target, and solid angle subtended at the target, for all 16 counters in the LAC and SAC respectively.

C#	Type	Central Angle degrees	Distance cm	Polar Angle 1/2 Width °	Solid Angle msr
1	cyl	15	164.6	2.209	4.670
2	cube	30	163.5	2.612	8.33
3	cyl	40	128.4	2.831	7.68
4	cube	50	93.8	4.550	25.34
5	cyl	60	126.6	2.870	7.90
6	cube	70	92.5	4.611	26.03
7	cyl	80	125.6	2.893	8.02
8	cube	90	93.0	4.586	25.74
9	cyl	100	125.6	2.893	8.02
10	cube	110	93.8	4.550	25.34
11	cube	120	93.5	4.562	25.48
12	cube	130	93.0	4.586	25.74
13	cyl	140	123.9	2.934	8.25
14	cube	150	92.5	4.611	26.03
15	cyl	160	124.8	2.913	8.13
16	cyl	170	130.7	2.781	7.42

Table E.2: Central angles, distances, 1/2 widths, and solid angles of Cerenkov detectors in the LAC

C#	Type	Central Angle degrees	Distance cm	Polar Angle 1/2 Width °	Solid Angle msr
1	cyl	15	152.0	2.392	6.02
2	cube	30	151.7	2.815	9.67
3	cyl	40	128.4	2.831	8.51
4	cube	50	80.0	5.327	34.80
5	cyl	60	123.9	2.934	9.25
6	cube	70	80.0	5.327	34.80
7	cyl	80	124.4	2.922	9.18
8	cube	90	80.0	5.327	34.80
9	cyl	100	124.4	2.922	9.18
10	cube	110	79.5	5.361	35.24
11	cyl	120	105.4	3.448	13.06
12	cube	130	80.0	5.327	34.80
13	cyl	140	121.9	2.982	9.58
14	cube	150	80.0	5.327	34.80
15	cyl	160	124.9	2.910	9.10
16	cube	170	80.0	5.327	34.80

Table E.3: Central angles, distances, 1/2 widths, and solid angles of Cerenkov detectors in the SAC

Appendix F

Systematic Errors

This appendix contains a description of systematic errors.

F.1 Errors that Normalize Out

Since the $pp\gamma$ cross sections were normalized to the elastic cross sections, certain uncertainties which were the same for both detection systems would normalize out and need not be considered. These include

1. the actual target thickness,
2. computer dead time,
3. the number of incident beam protons.

F.2 Errors in Measurement

These arise from uncertainty in determining the solid angles subtended by the detectors and in defining the polar angle of the center of the bins.

F.2.1 Cerenkov Detectors

Distances 'r' to counters was measured to an estimated accuracy of ± 0.5 cm. There is negligible error in measurement of the dimensions of the counters detection surface. Since the cross sections are compared with theoretical predictions for a full ϕ_γ acceptance, the only relevant error is in one dimension θ_γ . Now,

$$\frac{\Delta\theta_\gamma}{\theta_\gamma} = \frac{\Delta r}{r},$$

which, for detectors positioned from 80 to 160 cm, ranges from 0.6% to 0.3%. The polar angles of the bin centers were estimated to be known to within $\pm 1.0^\circ$ which is roughly 9% to 23% of their acceptance and thus negligible in comparison with the uncertainty introduced by averaging over the finite acceptance of the counters.

F.2.2 LE Detectors

Distance 'r' from the target errors are estimated at ± 0.3 cm and in dimension (x,y) measurement, ± 0.1 cm. The uncertainty in the solid

angle is then

$$\begin{aligned}\frac{\Delta\Omega}{\Omega} &= 2\frac{\Delta r}{r} + \frac{\Delta x}{x} + \frac{\Delta y}{y} \\ &\simeq \frac{2(.3)}{100.0} + \frac{0.1}{6.5} + \frac{0.1}{9.0} = 3.2\%.\end{aligned}$$

An estimated error of $\pm 0.1^\circ$ in the polar angle of the center of the detector is again negligible considering the 4° acceptance.

F.2.3 HE Detectors

The error in the distance from the target for the anode planes of 2X and 2Y is estimated at $\pm 1.0\text{cm}$. However, since the same error is inherent in the elastic cross section, the only error in distance to be considered is that arising from the uncertainty of the angle of the HE bin center for the $pp\gamma$ events with respect to that for the elastics. If a generous angle error of $\pm 1.0^\circ$ is allowed, the uncertainty in the distance, given that the chamber makes an angle of 25° with respect to the beam line, is

$$\begin{aligned}\frac{\Delta r}{r} &= \frac{\sin(90 - (\theta_{HE} + 25) + 1)}{\sin(90 - (\theta_{HE} + 25))} - 1 \\ &\simeq \frac{\sin(51.2)}{\sin(50.2)} - 1 = 1.4\%(SAC) \\ &\simeq \frac{\sin(41.5)}{\sin(40.5)} - 1 = 2.0\%(LAC).\end{aligned}$$

(F.1)

The error in the dimensional cut on 2X vs 2H should be small given the good intrinsic resolution of the drift chambers. An upper limit would

be ± 0.1 cm. In this case,

$$\begin{aligned}\frac{\Delta\Omega}{\Omega} &= 2\frac{\Delta r}{r} + \frac{\Delta x}{x} + \frac{\Delta y}{y} \\ &\approx 2(.014) + \frac{0.1}{14.} + \frac{0.1}{8.} = 4.7\%(SAC) \\ &\approx 2(.020) + \frac{0.1}{14.} + \frac{0.1}{8.} = 6.0\%(LAC)\end{aligned}\quad (F.2)$$

F.3 Errors in Efficiency Calculations

The biggest contributor in this category is the uncertainty in the photon detection efficiencies derived through the Monte Carlo code EGS. These stem from;

- (a) error in the determination of the absorber thicknesses between the target and detector, integrated over the solid angle of the detector,
- (b) uncertainty in the discriminator thresholds,
- (c) uncertainty inherent in the code itself which obviously must make some simplifications in simulating photon interaction mechanisms,
- (d) geometrical effects such as light coupling, etc.

Concerning point 1, a survey of the calculated detector efficiencies showed that a difference in absorber thickness of 10% results in a change in efficiency (at the photon energies of this experiment), of very roughly, 3%. (A 10% uncertainty in the integrated absorber thickness is probably a liberal but reasonable estimate.)

Concerning point 2, the code was run for a number of different detectors, each with a number of different discriminator thresholds centered around 20 MeV. The result was, on average

$$\frac{dEff}{dE_{thresh}}|_{thresh=20MeV} = 0.34\%/MeV$$

A maximum uncertainty in the discriminator thresholds of 7 MeV would mean an uncertainty in the detector efficiency of 2.4%, making them rather insensitive to thresholds.

Concerning point 3, the codes accuracy is quoted at 10%.

Concerning point 4, geometrical effects are probably not important since 70 MeV electron data gave high efficiencies of around 97%.

F.3.1 VDC Missing and Multiple Efficiencies

What is important here is not the error in the absolute, but rather in the relative efficiencies between the section of the chambers the elastics pass through and those sections the $pp\gamma$ events pass through. Since the missing efficiencies of the different sections vary by less than $\sim 6\%$, except for VDC 1 which is 10%. It is highly unlikely that the relative uncertainty is greater than a few percent per plane, giving a total of roughly 10% for all planes. For multiples the total variation is $\sim 10\%$ suggesting an uncertainty of perhaps 2%.

F.4 Other Errors

- (a) Error in the empirical values for the elastic cross sections at 16.5° (SAC) and 27.8° (LAC) are both about 1%.
- (b) Error in the estimate of the number of elastic protons that undergo a nuclear reaction in the Cu absorber but whose reaction products are detected in the scintillator behind the Cu. This depends on (besides the absorber thickness) the geometry of the scintillator hodoscope, i.e. the final scintillator should be well oversized. The difference between all reaction products being detected and no reaction products detected would be 18% (LAC) and 22% (SAC). A reasonable estimate of the error in the number of protons that react but are not detected (72% (LAC) and 66% (SAC)) would be 10%. This could then effect the cross sections by introducing an uncertainty of 1.8% (LAC) and 2.2% (SAC).

F.5 Conclusions

Taking the square root of the sum of the squares of all these errors, we estimate a total systematic error in the cross sections of 17% for both the small and large angle configurations.

The only systematic errors in the analysing powers could be those arising from an uncertainty in the polarization of the incident proton beam. This has contributions from an uncertainty in the analysing

power of hydrogen of 1%, and from the uncertainty in the observed instrumental asymmetry of the polarimeter (section 4.1.2) of perhaps 1%. Thus, the total systematic error is approximately 1.5%.

Appendix G

Analysing Powers and Cross Sections, Numerical Values

Tables of numerical values for the analysing powers and cross sections are given in the following pages.

SAC Small HE Angles (12.4°).

LE Angle 14.0°			LE Angle 22.0°			LE Angle 28.0°		
θ_γ	A_γ	Error	θ_γ	A_γ	Error	θ_γ	A_γ	Error
15.0	-0.199	0.137	15.0	-0.255	0.079	15.0	-0.326	0.120
30.0	-0.170	0.063	30.0	-0.152	0.066	30.0	-0.487	0.114
40.0	-0.213	0.073	40.0	-0.233	0.086	40.0	-0.353	0.136
50.0	-0.148	0.046	50.0	-0.104	0.049	50.0	-0.242	0.082
60.0	-0.122	0.087	60.0	-0.127	0.101	60.0	-0.068	0.161
70.0	-0.089	0.054	70.0	-0.101	0.064	70.0	-0.155	0.103
80.0	0.011	0.112	80.0	-0.087	0.131	80.0	-0.466	0.230
90.0	-0.038	0.063	90.0	-0.254	0.080	90.0	-0.324	0.148
100.0	-0.065	0.128	100.0	-0.031	0.142	100.0	-0.378	0.275
110.0	-0.160	0.055	110.0	-0.111	0.070	110.0	-0.032	0.120
120.0	-0.122	0.071	120.0	-0.395	0.106	120.0	-0.602	0.227
130.0	-0.089	0.048	130.0	-0.267	0.063	130.0	-0.073	0.104
140.0	-0.167	0.080	140.0	-0.281	0.106	140.0	-0.479	0.222
150.0	-0.175	0.046	150.0	-0.220	0.056	150.0	-0.568	0.126
160.0	-0.014	0.083	160.0	-0.252	0.102	160.0	-0.674	0.211
170.0	-0.044	0.047	170.0	-0.270	0.053	170.0	-0.462	0.108

SAC Large HE Angles (17.3°)

LE Angle 14.0°			LE Angle 22.0°			LE Angle 28.0°		
θ_γ	A_γ	Error	θ_γ	A_γ	Error	θ_γ	A_γ	Error
15.0	-0.879	0.554	15.0	-0.110	0.092	15.0	-0.138	0.095
30.0	-0.104	0.064	30.0	-0.076	0.051	30.0	-0.195	0.070
40.0	-0.057	0.055	40.0	-0.140	0.055	40.0	-0.029	0.078
50.0	-0.055	0.031	50.0	-0.063	0.030	50.0	-0.033	0.044
60.0	0.030	0.058	60.0	-0.093	0.057	60.0	-0.137	0.087
70.0	0.029	0.035	70.0	-0.059	0.037	70.0	-0.027	0.055
80.0	-0.004	0.067	80.0	0.035	0.076	80.0	-0.002	0.119
90.0	-0.051	0.038	90.0	0.015	0.043	90.0	-0.056	0.071
100.0	-0.012	0.071	100.0	0.057	0.085	100.0	-0.134	0.136
110.0	-0.019	0.036	110.0	-0.050	0.041	110.0	-0.047	0.068
120.0	-0.165	0.052	120.0	-0.120	0.059	120.0	-0.253	0.112
130.0	-0.106	0.037	130.0	-0.206	0.043	130.0	-0.225	0.070
140.0	-0.149	0.069	140.0	-0.045	0.074	140.0	-0.326	0.128
150.0	-0.098	0.045	150.0	-0.187	0.040	150.0	-0.210	0.070
160.0	0.064	0.097	160.0	-0.071	0.074	160.0	-0.243	0.138
170.0	-0.049	0.068	170.0	-0.128	0.043	170.0	-0.333	0.075

LAC Small HE Angles (21.2°)

LE Angle 14.0°			LE Angle 22.0°			LE Angle 28.0°		
θ_γ	A_γ	Error	θ_γ	A_γ	Error	θ_γ	A_γ	Error
15.0	0.366	0.462	15.0	-0.019	0.082	15.0	-0.230	0.091
30.0	-0.065	0.064	30.0	-0.124	0.050	30.0	-0.039	0.068
40.0	-0.093	0.054	40.0	-0.066	0.050	40.0	-0.170	0.074
50.0	0.000	0.035	50.0	-0.031	0.033	50.0	-0.006	0.047
60.0	-0.074	0.056	60.0	-0.100	0.056	60.0	-0.060	0.079
70.0	0.044	0.037	70.0	-0.018	0.038	70.0	-0.055	0.057
80.0	-0.016	0.063	80.0	-0.067	0.074	80.0	0.021	0.101
90.0	0.117	0.041	90.0	-0.025	0.046	90.0	0.017	0.073
100.0	-0.058	0.067	100.0	-0.003	0.075	100.0	0.108	0.113
110.0	-0.049	0.038	110.0	-0.028	0.044	110.0	-0.013	0.070
120.0	-0.044	0.038	120.0	-0.147	0.043	120.0	-0.002	0.070
130.0	-0.003	0.041	130.0	-0.149	0.046	130.0	-0.185	0.076
140.0	-0.046	0.074	140.0	-0.238	0.082	140.0	-0.300	0.128
150.0	0.052	0.053	150.0	-0.122	0.051	150.0	-0.183	0.080
160.0	-0.055	0.108	160.0	-0.023	0.094	160.0	-0.163	0.142
170.0	-0.113	0.152	170.0	0.079	0.106	170.0	-0.297	0.144

LAC Large HE Angles (27.8°)

LE Angle 14.0°			LE Angle 22.0°			LE Angle 28.0°		
θ_γ	A_γ	Error	θ_γ	A_γ	Error	θ_γ	A_γ	Error
15.0	-1.358	4.704	15.0	0.110	0.139	15.0	-0.054	0.081
30.0	-0.075	0.114	30.0	-0.093	0.047	30.0	0.010	0.054
40.0	-0.016	0.064	40.0	-0.051	0.043	40.0	-0.030	0.056
50.0	0.030	0.034	50.0	0.080	0.027	50.0	0.072	0.038
60.0	0.070	0.049	60.0	0.112	0.044	60.0	0.119	0.061
70.0	0.054	0.032	70.0	0.054	0.029	70.0	0.078	0.044
80.0	0.097	0.058	80.0	0.050	0.055	80.0	0.079	0.088
90.0	0.004	0.036	90.0	0.007	0.035	90.0	0.059	0.054
100.0	0.091	0.060	100.0	-0.075	0.059	100.0	-0.151	0.094
110.0	0.009	0.039	110.0	0.053	0.036	110.0	0.056	0.057
120.0	0.046	0.042	120.0	0.048	0.037	120.0	0.076	0.056
130.0	0.053	0.053	130.0	-0.032	0.039	130.0	-0.119	0.063
140.0	0.014	0.109	140.0	-0.018	0.074	140.0	-0.117	0.110
150.0	0.017	0.089	150.0	-0.019	0.049	150.0	-0.127	0.076
160.0	-0.026	0.208	160.0	0.136	0.095	160.0	-0.266	0.135
170.0	0.126	0.435	170.0	0.005	0.114	170.0	-0.075	0.141

SAC Small HE Angles (12.4°)

LE Angle 12.0°			LE Angle 16.0°			LE Angle 20.0°			LE Angle 24.0°			LE Angle 28.0°		
θ_γ	$\sigma(\mu b)$	Error	θ_γ	$\sigma(\mu b)$	Error	θ_γ	$\sigma(\mu b)$	Error	θ_γ	$\sigma(\mu b)$	Error	θ_γ	$\sigma(\mu b)$	Error
15.0			15.0	0.410	0.116	15.0	0.899	0.248	15.0	0.951	0.287	15.0	0.963	0.328
30.0	0.710	0.181	30.0	0.733	0.194	30.0	0.793	0.223	30.0	0.814	0.254	30.0	0.875	0.210
40.0	0.834	0.262	40.0	0.944	0.344	40.0	0.645	0.225	40.0	0.822	0.338	40.0	0.698	0.261
50.0	0.520	0.098	50.0	0.657	0.147	50.0	0.669	0.169	50.0	0.609	0.139	50.0	0.437	0.099
60.0	0.529	0.192	60.0	0.613	0.246	60.0	0.473	0.206	60.0	0.540	0.223	60.0	0.566	0.318
70.0	0.423	0.087	70.0	0.479	0.115	70.0	0.440	0.116	70.0	0.356	0.096	70.0	0.291	0.071
80.0	0.266	0.119	80.0	0.657	0.310	80.0	0.389	0.184	80.0	0.399	0.246	80.0	0.384	0.221
90.0	0.536	0.126	90.0	0.530	0.147	90.0	0.466	0.145	90.0	0.420	0.140	90.0	0.371	0.137
100.0	0.491	0.192	100.0	0.461	0.208	100.0	0.474	0.230	100.0	0.296	0.149	100.0	0.230	0.136
110.0	0.676	0.112	110.0	0.673	0.146	110.0	0.544	0.129	110.0	0.398	0.099	110.0	0.385	0.104
120.0	1.245	0.332	120.0	0.858	0.250	120.0	0.728	0.234	120.0	0.669	0.281	120.0	0.418	0.169
130.0	1.089	0.161	130.0	1.014	0.182	130.0	0.844	0.186	130.0	0.552	0.125	130.0	0.569	0.152
140.0	1.949	0.545	140.0	1.517	0.492	140.0	1.126	0.411	140.0	1.099	0.486	140.0	1.107	0.618
150.0	1.789	0.230	150.0	1.698	0.275	150.0	1.118	0.195	150.0	1.153	0.260	150.0	0.788	0.171
160.0	1.891	0.490	160.0	2.188	0.613	160.0	1.982	0.692	160.0	1.504	0.565	160.0	1.359	0.565
170.0	1.434	0.204	170.0	1.851	0.278	170.0	1.523	0.263	170.0	1.333	0.248	170.0	0.823	0.173

SAC Large HE Angles (17.3°)

LE Angle 12.0°			LE Angle 16.0°			LE Angle 20.0°			LE Angle 24.0°			LE Angle 28.0°		
θ_γ	$\sigma(\mu b)$	Error	θ_γ	$\sigma(\mu b)$	Error	θ_γ	$\sigma(\mu b)$	Error	θ_γ	$\sigma(\mu b)$	Error	θ_γ	$\sigma(\mu b)$	Error
15.0			15.0			15.0			15.0			15.0		
30.0			30.0			30.0			30.0	1.409	0.356	30.0	1.230	0.254
40.0			40.0			40.0	1.440	0.405	40.0	1.579	0.436	40.0	1.652	0.445
50.0			50.0	1.254	0.186	50.0	1.277	0.193	50.0	1.258	0.201	50.0	1.461	0.232
60.0	1.235	0.366	60.0	1.149	0.330	60.0	1.496	0.432	60.0	1.351	0.442	60.0	1.221	0.408
70.0	0.915	0.153	70.0	1.044	0.172	70.0	0.901	0.160	70.0	0.874	0.163	70.0	0.925	0.182
80.0	1.173	0.383	80.0	1.135	0.370	80.0	1.052	0.415	80.0	1.091	0.448	80.0	0.815	0.305
90.0	1.441	0.267	90.0	1.358	0.263	90.0	1.365	0.290	90.0	1.166	0.275	90.0	1.057	0.254
100.0	1.534	0.446	100.0	1.256	0.405	100.0	1.546	0.624	100.0	0.928	0.343	100.0	1.061	0.461
110.0	1.450	0.166	110.0	1.471	0.226	110.0	1.197	0.203	110.0	1.035	0.190	110.0	0.919	0.169
120.0	1.968	0.392	120.0	1.961	0.443	120.0	1.777	0.442	120.0	1.585	0.434	120.0	1.051	0.309
130.0	1.715	0.211	130.0	1.823	0.252	130.0	1.780	0.284	130.0	1.295	0.206	130.0	1.561	0.315
140.0	1.988	0.500	140.0	2.695	0.691	140.0	2.653	0.833	140.0	2.147	0.708	140.0	2.343	0.915
150.0	2.170	0.357	150.0	2.127	0.301	150.0	2.611	0.414	150.0	2.267	0.393	150.0	1.520	0.265
160.0	1.551	0.526	160.0	2.549	0.736	160.0	3.830	1.211	160.0	2.186	0.638	160.0	1.863	0.677
170.0			170.0			170.0	1.916	0.318	170.0	1.818	0.313	170.0	1.416	0.263

LAC Small HE Angles (21.2°)

LE Angle 12.0°			LE Angle 16.0°			LE Angle 20.0°			LE Angle 24.0°			LE Angle 28.0°		
θ_γ	$\sigma(\mu b)$	Error	θ_γ	$\sigma(\mu b)$	Error	θ_γ	$\sigma(\mu b)$	Error	θ_γ	$\sigma(\mu b)$	Error	θ_γ	$\sigma(\mu b)$	Error
15.0			15.0			15.0			15.0	1.060	0.208	15.0	1.488	0.296
30.0			30.0	0.884	0.142	30.0	1.360	0.232	30.0	1.341	0.224	30.0	1.532	0.254
40.0	0.969	0.1	40.0	1.449	0.268	40.0	1.308	0.250	40.0	1.942	0.406	40.0	1.805	0.360
50.0	0.926	0.1	50.0	1.150	0.141	50.0	1.267	0.154	50.0	1.377	0.179	50.0	1.667	0.226
60.0	1.082	0.210	60.0	1.447	0.333	60.0	1.722	0.407	60.0	1.324	0.290	60.0	1.664	0.407
70.0	0.888	0.115	70.0	1.060	0.144	70.0	1.046	0.150	70.0	1.192	0.175	70.0	1.064	0.155
80.0	1.071	0.229	80.0	1.232	0.308	80.0	0.922	0.237	80.0	1.288	0.372	80.0	1.432	0.431
90.0	1.451	0.199	90.0	1.613	0.262	90.0	1.406	0.241	90.0	1.355	0.261	90.0	1.342	0.277
100.0	1.560	0.346	100.0	1.378	0.311	100.0	1.531	0.413	100.0	1.333	0.383	100.0	1.401	0.409
110.0	1.603	0.180	110.0	1.540	0.200	110.0	1.287	0.176	110.0	1.315	0.194	110.0	1.149	0.184
120.0	1.587	0.168	120.0	1.734	0.211	120.0	1.544	0.202	120.0	1.660	0.252	120.0	1.557	0.266
130.0	1.711	0.193	130.0	1.752	0.212	130.0	1.483	0.189	130.0	1.828	0.261	130.0	1.566	0.257
140.0	1.956	0.417	140.0	2.103	0.470	140.0	1.852	0.417	140.0	1.639	0.394	140.0	2.262	0.747
150.0	1.287	0.188	150.0	2.276	0.328	150.0	2.077	0.305	150.0	1.844	0.284	150.0	1.799	0.289
160.0	1.008	0.270	160.0	2.467	0.619	160.0	1.832	0.460	160.0	1.967	0.502	160.0	1.937	0.552
170.0			170.0			170.0	1.150	0.309	170.0	1.433	0.440	170.0	1.410	0.432

LAC Large HE Angles (27.8°)

LE Angle 12.0°			LE Angle 16.0°			LE Angle 20.0°			LE Angle 24.0°			LE Angle 28.0°		
θ_γ	$\sigma(\mu b)$	Error	θ_γ	$\sigma(\mu b)$	Error	θ_γ	$\sigma(\mu b)$	Error	θ_γ	$\sigma(\mu b)$	Error	θ_γ	$\sigma(\mu b)$	Error
15.0			15.0			15.0			15.0			15.0	1.831	0.360
30.0			30.0			30.0			30.0	1.966	0.297	30.0	2.352	0.331
40.0			40.0			40.0	2.394	0.426	40.0	2.651	0.472	40.0	2.549	0.407
50.0			50.0	1.596	0.172	50.0	2.247	0.265	50.0	2.388	0.266	50.0	2.335	0.258
60.0	1.490	0.280	60.0	2.137	0.402	60.0	2.112	0.388	60.0	2.349	0.443	60.0	2.804	0.560
70.0	1.274	0.141	70.0	1.948	0.235	70.0	2.043	0.256	70.0	2.061	0.268	70.0	1.781	0.212
80.0	1.321	0.251	80.0	1.996	0.417	80.0	2.073	0.436	80.0	2.013	0.451	80.0	1.801	0.421
90.0	1.830	0.239	90.0	2.698	0.358	90.0	2.640	0.371	90.0	2.687	0.429	90.0	2.362	0.367
100.0	1.635	0.395	100.0	2.658	0.553	100.0	2.446	0.523	100.0	2.027	0.419	100.0	2.343	0.572
110.0	1.366	0.165	110.0	2.258	0.263	110.0	2.285	0.284	110.0	2.007	0.245	110.0	2.322	0.330
120.0	1.197	0.151	120.0	2.262	0.266	120.0	2.335	0.286	120.0	2.203	0.266	120.0	2.455	0.330
130.0	0.977	0.159	130.0	1.958	0.242	130.0	2.418	0.311	130.0	2.474	0.337	130.0	2.031	0.275
140.0	0.790	0.340	140.0	2.161	0.538	140.0	2.532	0.590	140.0	2.841	0.729	140.0	2.857	0.806
150.0			150.0	1.487	0.255	150.0	2.234	0.340	150.0	2.339	0.359	150.0	2.157	0.341
160.0			160.0	1.418	0.527	160.0	2.067	0.567	160.0	2.590	0.774	160.0	1.616	0.436
170.0			170.0			170.0			170.0	1.185	0.415	170.0	1.505	0.550